UC Berkeley
UC Berkeley Electronic Theses and Dissertations

Title

Talkin' About a Revolution: The Dynamics of the Rotary Motor of Bacterial Flagella

Permalink

https://escholarship.org/uc/item/8wx803d1

Author

Nirody, Jasmine Ashok

Publication Date

2017

Peer reviewed|Thesis/dissertation

Talkin' About a Revolution:
The Dynamics of the Rotary Motor of Bacterial Flagella

by

Jasmine Ashok Nirody

A dissertation submitted in partial satisfaction of the
requirements for the degree of
Doctor of Philosophy

in

Biophysics
and the Designated Emphasis

in

Computational and Genomic Biology

in the

Graduate Division

of the

University of California, Berkeley

Committee in charge:

George Oster, Chair
Carlos Bustamante
Oskar Hallatschek
David Steigmann

Spring 2017

Talkin' About a Revolution:
The Dynamics of the Rotary Motor of Bacterial Flagella

Abstract

Talkin' About a Revolution: The Dynamics of the Rotary Motor of Bacterial Flagella

by

Jasmine Ashok Nirody

Doctor of Philosophy in Biophysics

and the Designated Emphasis in Computational and Genomic Biology

University of California, Berkeley

Professor George Oster

The bacterial flagellar motor (BFM) is an ion-powered nanomachine that drives swimming in many bacteria. Its central role in processes like chemotaxis and biofilm formation has made obtaining a mechanistic understanding of its function a central challenge in biophysics. This protein complex is comprised of several transmembrane rings connected to a long flagellar filament by a flexible hook. Rotation is known to occur via an interaction between one or more membrane-embedded "stator" units and protein spokes on the periphery of the "rotor" ring. Further modeling has been stymied by the lack of atomic-level structures, which are hard to obtain because the BFM is large and traverses the membrane.

The work in this thesis attempts to clear this hurdle by combining partial crystal structures, mutation and crosslinking experiments, and biophysical measurements to propose a mechanically-specific, experimentally-testable model of how the motor generates torque. Predictions are validated against biophysical measurements on single-stator motors, which isolate the properties of the motor's fundamental mechanochemical cycle by removing the effects of interactions between individual stator units.

This base model is also extended to consider the behavior of multi-stator motors. Recent experiments have shown that stator units dynamically bind and leave the motor, influenced by several factors, including the ion gradient, external load, and motor speed. This has brought into question past results, one of which is the long-held conviction that the maximum speed of the motor is independent of stator number; that is, that at near-zero load, one engaged stator unit can push the motor at its maximum speed. The model proposed in this thesis predicts that such a "limiting" zero-torque speed in fact does not exist: Recruitment of additional stator units, even at very low external load, results in an increase in motor speed. This assertion is supported by experimental results in chimeric sodium-driven motors.

Finally, validation experiments for this model are described. The mechanism presented is unique in that it suggests motor rotation is loosely coupled to ion flux; that is, an ion passage may not always constitute a fully efficient power stroke. Thus, motor steps are likely to be unequal in size, and the number of ions required for a full revolution of the motor may vary with external conditions. This notion is tested using single-cell fluorescent measurements to compare ion flux in motors at different speeds.

To my brother,
  whose curiosity is a constant reminder of the worth of studying physics.

And to *E. coli*,
  for giving me so much to be curious about.

Contents

Acknowledgments

It is standard to thank one's advisor first, and I do so with the important note that there has been nothing standard about the mentorship and guidance I have received from **George Oster** during my time here at Berkeley. From George, I've learned that complex physical processes are sometimes best explained using playground analogies and shadow puppets, that simple ideas are often the most poignant, that puzzles are always exciting, even when— *especially when*—they seem to make no sense. His mark on the work in this thesis is clearly visible but not heavy-handed; somehow, I always found myself with exactly the amount of help I needed, but no more. I have been lucky to have had an advisor who trusted my intuition even when it seemed crazy, who let me stumble because he always believed I could get back up on my own. I have been even more lucky to have had an advisor who has been not only a great mentor, but also a great friend. Undertaking a PhD can be a lonely task, but choosing to do mine with George has made it decidedly less so. To George: Thank you for everything. I will work hard to earn the confidence you have had in me.

Much of this thesis would also have not been possible without the guidance and insight of **Richard Berry**, who kindly let me infiltrate his lab towards the end of my PhD. Thinking up and attempting crazy experiments with Richard has been a dream I never knew I had, but am very happy to be fulfilling. It has been an immense pleasure to be a part of the molecular motors group at Oxford, both professionally and personally; special thanks go to **Robert Ishmukhametov**, **Sam Tusk**, and **Joel Spratt** for emulating the skills a great experimentalist must have (primarily patience); and to **Jordan Juritz** for being a shining example of everything a MPhys student should be.

From conception to conclusion, the work in this thesis has been shaped by the advice of many wonderful people, in particular my qualifying and dissertation committees: **Carlos Bustamante**, **Ahmet Yildiz**, **Nir Yosef**, **Mohammed Mofrad**, **David Steigmann**, and **Oskar Hallatschek**; and my collaborators, who are listed in the conclusion of the first chapter. Outside of my dissertation research, I have had the good fortune to work on a variety of projects on a variety of topics over the years, a freedom for which I am extremely grateful. I am even more grateful, however, that these projects have allowed me the privilege of working with and learning from people like **Robert Full**, **Judy Jinn**, **Miklós Rácz**, **Susana Serna**, **Galateia Kazakia**, **David Hu**, and **Michael Shelley**.

The importance given to interdisciplinary science at Berkeley (for which I am incredibly thankful) has resulted in the development of an almost over-abundance of awesome institutes on campus. I have had the pleasure of being affiliated with several of these, and I credit them for providing me with an environment that was somehow simultaneously both extremely challenging and welcoming. More practically, they have also provided me with research funding, desk space, and so much free coffee. Specific mentions go to **CiBER** (here, I must give an extra note of appreciation to **Tom Libby** and **Robert Full** for keeping such an innovative and unique space running so smoothly for so long), **BIDS**, **QB3**, and the **Simons Institute for Theoretical Computing**.

Chapter 1

Summa scientia: an introduction

> "Whatever is in motion must be put in motion by another. If that by which
> it is put in motion be itself put in motion, then this also must needs be put in
> motion by another, and that by another again. But this cannot go on to infinity,
> because then there would be no first mover, and, consequently, no other mover;
> seeing that subsequent movers move only inasmuch as they are put in motion by
> the first mover; as the staff moves only because it is put in motion by the hand.
> Therefore it is necessary to arrive at a first mover, put in motion by no other;
> and this everyone understands to be..."
>
> — St. Thomas Aquinas, *Summa Theologica*

Movement is one of the defining characteristics of life, so much so that St. Thomas
Aquinas once utilized its mysteries in his philosophical "proof" of the existence of God, the
"first mover". The wonder in and study of how things move has been pervasive throughout
the history of science and philosophy, filling the notebooks of Aristotle and DaVinci, as well
as the hard drives of biologists, physicists, mathematicians, and engineers today.

At some point during their time on Earth, all living things move, though some do so so
subtly that you may not notice it. As you are reading this sentence, you, too, are moving
— even if you are not conscious of it. Even if you are consciously trying *not* to. Air flows
into expanded lungs and out of deflated ones; heart muscles contract, forcing blood through
arteries and capillaries and veins; intestines churn and grind remnants of meals past. To be
alive, is to be in motion.

1.1 Rafting, rowing, and ratcheting: (fluid) motion across scales

Though some, or arguably most, biological motion may be imperceptible to us, movement is
often the first thing to catch our (and according to Spielberg, the *Tyrannosaurus rex*'s) eye.
The variety of these movements, and the variety of environments in which they take place,
is a marvel of evolution — and, luckily for us, one that has been characterized conveniently
(at least, for fluid-based motility, which will be the focus of our discussion here; for further
information on terrestrial locomotion, we refer the interested reader to [53, 4, 17]).
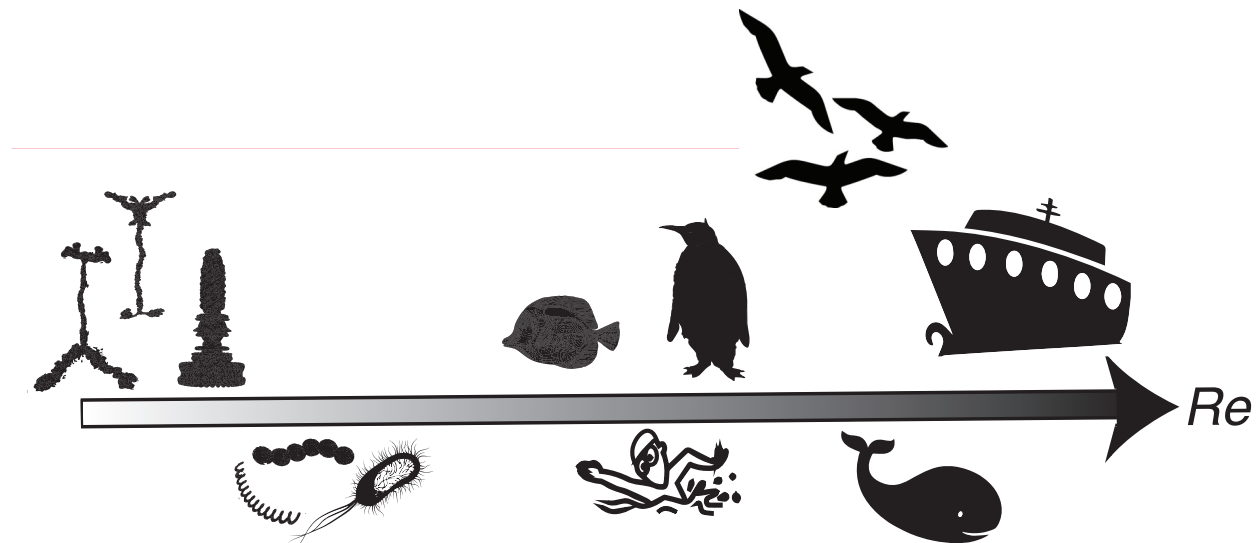
Figure 1.1: The Reynolds number (Re) is a useful metric to compare fluid locomotion across scales. Shown here are things that move through fluids spanning over 10 orders of magnitude in Re. Nanoscale molecular motors and microorganisms move in a viscous world (Re $\sim$ $10^{-6} - 10^{-3}$), while larger fish and humans swim at considerably larger Reynolds numbers of approximately 10^4. Giant cruise ships and birds flying through thin air exist at larger still Reynolds numbers (Re $> 10^7$).

The **Reynolds number** (Re) is used to predict flow patterns in a wide range of situations, from fluid flowing in a pipe to fish swimming in a lake. It is the ratio of inertial forces to viscous forces, defined as:

$$\text{Re} = \frac{\rho v L}{\mu} = \frac{v L}{\nu}, \tag{1.1}$$

where ρ is the density of the fluid, v is the characteristic velocity of the fluid with respect to the object, L is the characteristic length, and μ and ν are the dynamic and kinematic viscosities of the fluid [43]. A particularly useful application of this dimensionless quantity is the ability to compare similar but differently-sized fluid situations (Figure 1.1). For example, one might not imagine that the physical intuition needed to understand a man wading through peanut butter and a bacteria swimming in water are related. But they are: These situations both correspond to a low Reynolds number world ($\sim 10^{-1}$ and $\sim 10^{-5}$, respectively).

This world — in which viscous forces dominate and inertia means nothing — will be the one in which the work in this dissertation takes place. The scaling analogies allotted to us via the Reynolds number will turn up again and again in our quest to understand the physics of the foreign world of tiny things. While this paragraph marks the end of our general discussion on the low Reynolds number environment and the things that move
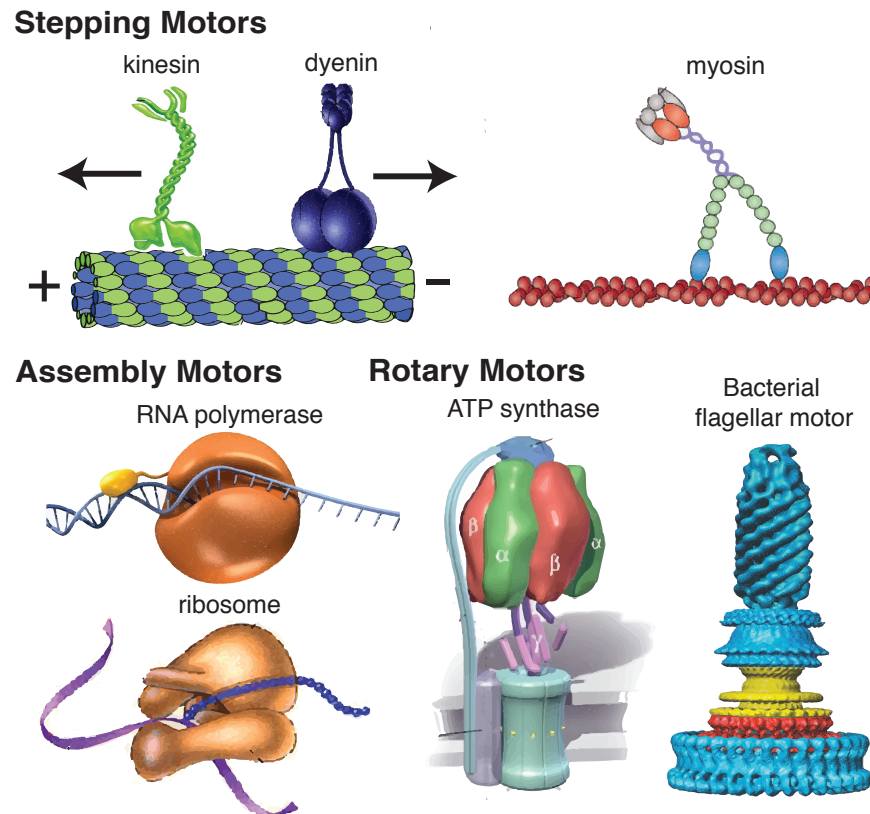
Figure 1.2: Molecular motors use chemical energy in order to perform a wide range of tasks in the cell. Cargo-carrying motors like dyenin, kinesin, and myosin step along tracks like microtubles and actin. Assembly motors like polymerases and ribosomes construct nucleic acids and polypeptides out of monomeric units. Rotary motors use the energy stored in the transmembrane ion gradient to generate torque for ATP synthesis (ATP synthase) and to drive bacterial swimming (bacterial flagellar motor).

within it, we endorse enthusiastically and repeatedly (multiple!) reading(s) of E.M Purcell's outstanding *Life at Low Reynolds Number* [101]. There are also excellent resources for the reader interested in locomotion at high [3] and intermediate [32] Re.

1.2 For molecular motors, life is a drag

Remember the analogy we made about how a bacterium swimming in water is akin to a human wading in peanut butter? Now that we've dipped our toes in this (very viscous) pool, let's dive in deeper. Instead of watching bacteria swim, we will now consider the tiny machines chugging along inside them. Motion in this (sub)microscropic world is dominated by these **molecular motors**, protein assemblies which take chemical energy from their

environment and transform it into mechanical work. There are a great variety of them, that perform a great variety of cellular tasks (Figure 1.2). These nanomotors can live in worlds with Re as low as 10^{-9}: Take that man wading in peanut butter, and pour some asphalt on him [41].

Another thing happens when we shrink down to a scale this small. Molecular motors generate forces only slightly above the surrounding thermal bath, and all of a sudden, those previously negligible noisy forces and fluctuations can no longer be ignored. That poor man we buried in the tar pits? We forgot to mention: He's also in the middle of a hurricane (with winds strong enough to shake asphalt). But unlike our tar pit explorer, molecular motors have spent a long time (evolutionarily speaking) living in and mastering this environment. It is quite possible that they not only *survive* the thermal fluctuations going on around them, but *bias them* to help perform useful work.

The energy for the work of molecular motors comes from one of two sources: (1) chemical energy, derived from the hydrolysis of adenosine tri-phosphate (ATP); and (2) **electrochemical energy**, from the passage of ions across a membrane down a gradient. As we mentioned, the energies at which molecular motors operate are only slightly above the Brownian fluctuations all around them.

Given all this, it now makes sense to abandon the language of classical fluid mechanics, which treats the environment as a continuous (i.e., infinitely divisible) substance, for one which allows us to consider a more detailed molecular description of the surroundings: **statistical mechanics**. To this end, we will now speak of energies scaled according to these fluctuations, $k_B T$, where k_B is the Boltzmann constant and T is the temperature (let's call room temperature, at which most molecular motors operate, T_0). One $k_B T_0$ is 4×10^{-21} J, for the reader keen on SI units. Now, to get an idea of what molecular motors are working with: The hydrolysis of a single ATP molecule yields $\sim 20 k_B T_0$, while an ion crossing the cell membrane provides $\sim 6 k_B T_0$.

1.3   Nature spins its wheels

As Figure 1.2 shows, we can divide molecular motors into two general categories: linear and rotary motors. We zone in on the latter; while linear motors perform many important cellular tasks, we leave you to read about them elsewhere [50, 27, 54]. Nature might have only invented the wheel twice, but she has put it to good use: The two known rotary protein motors are responsible for producing the cellular energy currency (ATP synthase), and driving motility in a wide range of bacterial species (the **bacterial flagellar motor**, or BFM, on which the work in this dissertation focuses).

Flagellated locomotion is the most common form of bacterial motility, observed in many species and driven by variations of the BFM. This motor is central to several biological processes, including biofilm formation and the "-taxes" — chemotaxis, phototaxis, magnetotaxis, and thermotaxis [102, 85]. Though it is rightfully well-studied and characterized in
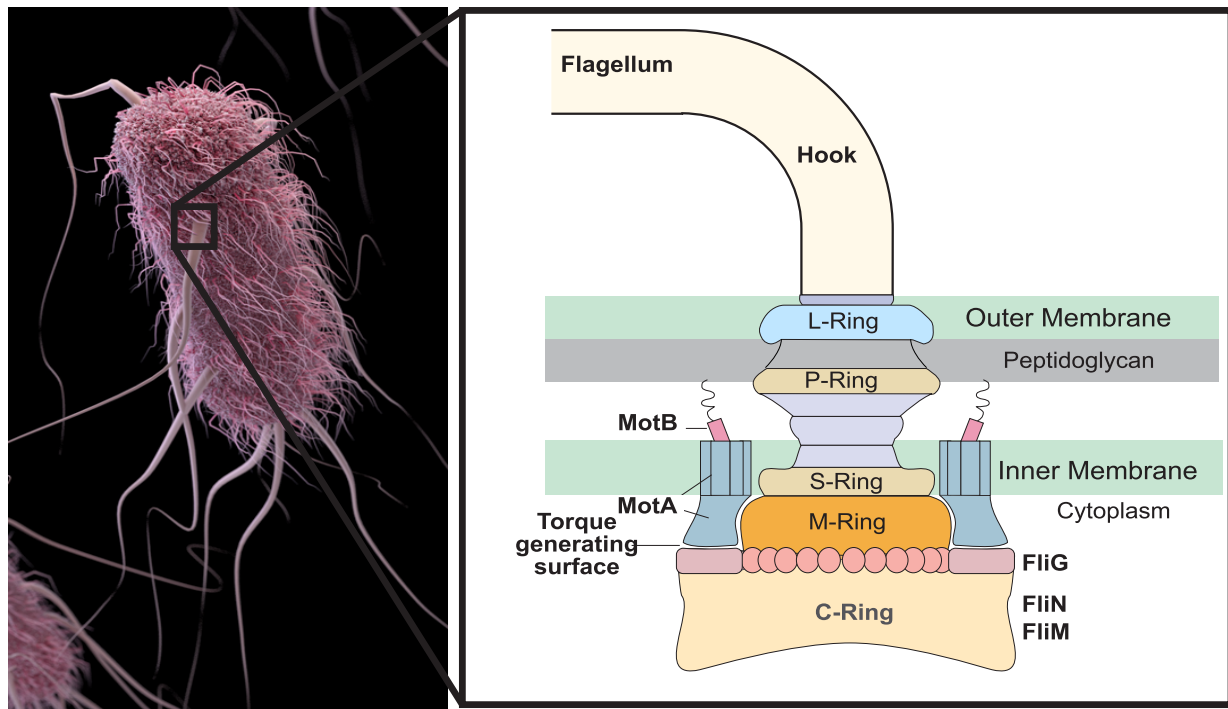
Figure 1.3: *E. coli* swim by beating several long flagellar filaments extending from the cell body, each driven by a motor at its base. Shown is a schematic of the basic parts of the bacterial flagellar motor. Depending on external load, motors adapt their structure to have between 1 and 11 torque-generating Mot complexes (stators). Figure adapted from the Center for Disease Control and [76].

terms of its structure and function, much remains to be uncovered regarding the fundamental mechanism of this motor's operation.

The BFM's mysteriousness, in large part, is thanks to its large size (relative to other molecular machines, not a bread box) and its localization to the membrane. These features make obtaining an atomic-level structure of the motor challenging, thus stymieing most modeling efforts. Here's what we *do* know: The **basal body** of the BFM spans the cellular envelope and is comprised of several transmembrane rings that connect to the bacterium's flagellar filament by a flexible hook. These rings are approximately 45 nm in diameter, containing approximately 25 different proteins. Motor rotation is known to occur via an interaction between one or more membrane-embedded torque-generating **stator** *mot* (for motility!) units and spoke-like proteins (FliG's) along the periphery of the **rotor** C-ring (Figure 1.3) [10].

This interaction is powered by the ion-motive force arising from the transit of ions (protons, in the case of the commonly-studied *Escherichia coli* motor) across the cellular membrane. The BFM is remarkable in its ability to efficiently convert the free energy stored in

this transmembrane electrochemical gradient into mechanical work: while man-made engines lose significant amounts of energy to heating, the BFM operates at close to 100% efficiency. Rotating at approximately 300 Hz (or 18000 rpm; compare to the upper limit of a typical car engine's rotational speed of 6000 rpm), the *E. coli* motor can output a power of approximately 1.5×10^5 pN nm s^{-1} [124] and propel the bacteria at a speed up to 100 μm s^{-1} — that is, up to 100 body lengths per second! The BFM of other species have been shown to rotate several times faster [10]. Regardless, we still choose to focus our work on the *E. coli* motor, because speed isn't everything.

1.4   What's in the rest of this thesis?

As previously mentioned, the remainder of this dissertation zones in on the bacterial flagellar motor. In Chapter 2, we provide a history of theoretical and experimental milestones in the study of this nanomachine, with a bend towards understanding how these approaches have informed each other towards a deeper, mechanistic understanding of motor function. The work in this chapter is joint work with Yi-Ren Sun and Chien-Jung Lo [91]. In Chapter 3, we summarize our work towards building a mechanically-specific, experimentally-testable model for torque-generation in motors with a single stator (joint work with Kranthi Mandadapu, Richard Berry, and George Oster [76]). Next, we generalize this model to understand the dynamics of motors with multiple torque-generating stator units in various external conditions (Chapter 4, joint work with Richard Berry and George Oster [90]). In keeping with the spirit of the collusion between theory and experiment, Chapter 5 focuses on the design and implementation of experiments to directly test predictions of the fundamental model proposed in earlier chapters. We end by looking to the future in Chapter 6.

Chapter 2

The biophysicist's guide to the BFM

> "Far out in the uncharted backwaters of the unfashionable end of the Western Spiral arm of the Galaxy lies a small unregarded yellow sun. Orbiting this at a distance of roughly ninety-eight million miles is an utterly insignificant little blue-green planet whose ape-descended life forms are so amazingly primitive that they still think [rotary motors] are a pretty neat idea."
>
> — Douglas Adams, *The Hitchhiker's Guide to the Galaxy*

The bacterial flagellar motor's fundamental role in facilitating several biological processes has made it one of the most well-studied molecular machines. Furthermore, the long history of research on the BFM is a wonderful example of how valuable the close interplay between theory and experiment can be (for an even more summarized overview, see Figure 2.1). Experimental results have inspired theoreticians to build and update models, while model predictions have served to guide experimental design. This cooperative and mutually beneficial communication is a prime example of the interdisciplinary and open nature of modern scientific research.

In this chapter, we provide an overview of past experimental and theoretical research on the BFM; our goal is to emphasize both the richness of this history, while highlighting that there remain many fascinating open questions about the function of this dynamic nanomachine.

2.1   Experimental milestones

The first swimming bacterial cells were observed in the 17$^{\text{th}}$ century by Antonie van Leeuwenhoek. But the powerhouse behind this locomotion, the bacterial flagellar motor, remained a mystery. Too tiny to be observed easily using optical microscopes, the flagellar filament and the motor that spins it went unnoticed for 300 years. Starting from the mid-1900s, we outline here several important experimental leaps that have led us to our current understanding of the BFM.

Experiment

| 1970s |
| 1980s |
| 1990s |
| 2000s |
| 2010s |
| Now |

Electron microscopy (1971): Basic motor structure (filament-hook-basal body) is revealed. Later, EM unveils elements of the switching complex (1994), basal body symmetry (2006), and structure of the sodium-driven stator (2011).

Tethered cells (1974): Experiments involving cells tethered to surfaces via sheared flagellar filaments allowed direct observation of the rotation of the motor.

Energy source (1977): The BFM is shown to be driven by proton-motive force rather than by ATP. The dependence of motor speed is shown to be linear in V_m over the physiological range (1995).

Resurrection (1984): Trials in which rotation was recovered from paralyzed *mot* mutants reveals the motor is driven by independent force-generating units.

Applying external torque (1993): Techniques that allow control over the applied torque on the motor are developed (e.g., optical trapping and electrorotation). These experiments allow for the direct measurement of the motor torque-speed relationship.

Bead assay (2000): Attaching beads to flagellar hooks and observing their rotation characterizes motor behavior over a larger range of motor speeds than tethered cell experiments.

Chimeric motor (2003): A chimeric bacterial strain using sodium-, rather than proton-driven stators allowed for experiments across a wide range of ion-motive forces (IMFs). This opened many doors; e.g., torque-speed curves at various IMFs could now be collected (2013).

Steps (2005): Improvements in experimental resolution, as well as the developments providing control over IMF and external torque allow direct observation of stepping behavior in the BFM.

Component Turnover (2006): Motor structure was shown to be dynamic, with many components (e.g., FliM, FliN, *mot* complexes) in constant turnover.

Load-dependent assembly (2013): The turnover of stator complexes is shown to be related to external load: Motors at high load maintain higher stator number than at low loads.

Theory

Oosawa and Hayashi (1986): The first theoretical model to use current structural information and make quantitative, testable predictions. Proposed a loosely coupled mechanism inspired by the mechanism of crossbridges in skeletal muscle.

Läuger (1988): Conformational change based model similar to Oosawa and Hayashi with the exception of proposing that ion flux is necessarily tightly coupled to motor rotation.

Meister (1989): Tightly coupled model proposing stators have two "half-channels" that allow for alternating access to the cyto- and periplasm. Fit well with torque-speed curves collected from the tethered-cell experiments.

Berry (1993): A purely electro-statically driven model in which proton flow is coupled to motor rotation due to alternating tilted lines of positive and negative charges on rotor.

Elston and Oster (1997): "Ion turbine" model similar to that of Berry, with the added possiblity that stator units could be either "fixed" or "movable".

Mora et al. (2009): Modeled stators as protein springs that attach and detach along the rotor's circumference. Made two major assumptions: all stator units work in unison and apply torque simultaneously and additively; torque is due to a contact force at the interface between the stator and rotor.

Xing et al. (2006): Model involving a conformational change with the following requirements: an elastic connection between stator and rotor; tight coupling; ion channel in stator is gated by rotor movement.

Meacci and Tu (2009): Kinetic model predicting a zero-torque speed independent of stator number. Reproduced stepping behavior using two timescales: waiting time t_w (chemical transition) and moving time t_m (power stroke/motor rotation).

Mandadapu et al. (2015) & Chapter 3: Conformational change model with a loosely-coupled mechanism. Torque generation is due to formation of proline-hinge driven "kink" in cytoplasmic stator loops upon proton binding. Predicts that zero-torque speed increases with addition of engaged stators.
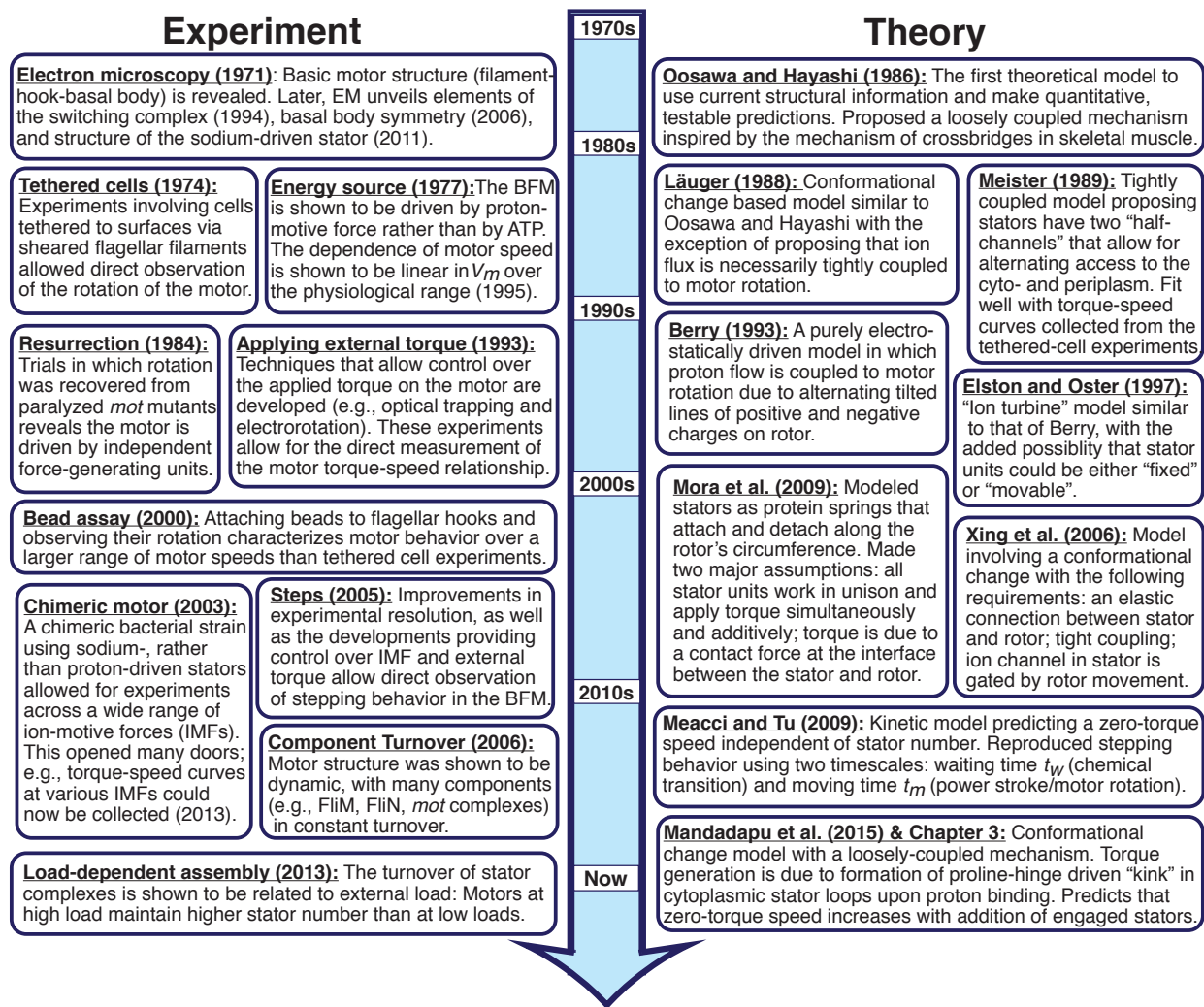
Figure 2.1: A timeline of selected experimental and theoretical milestones in our understanding of the structure and function of the bacterial flagellar motor, from the 1970s to the present (including this work!).

Electron microscopy images (1971)

Understanding, or even imagining, how something works is, not impossible, but really, really improbable, if it has never been seen. So, predictably, the first investigation into the flagellar machinery concerned its structure: From the 1950s onward, several attempts to image the BFM using electron microscopy were made (see Figure 2.2A).

First, the rough structure of the disk-like basal body was resolved [1, 30]; however, the details of these disks remained unclear because they are surrounded by the bacterium's cellular envelope. Later, in 1971, a series of papers described a way to purify the flagellar filament-hook-basal body complex (termed the **intact flagella**) [37, 38, 36, 39]. These sketches of the fundamental features of the motor were enough to inspire the first quantitative modeling efforts; further structural information over the years has served to allow for more specific, detailed models, as well as to validate model predictions.

In 1994, researchers were able to isolate and characterize the basal body, together with the **switching complex** (responsible for changing the direction of motor rotation, e.g., from couterclockwise to clockwise, during chemotaxis; for more information on this topic, see [119]) [47]. With the development of cyroEM techniques, access to detailed knowledge of the structure of the rotor increased drastically [115, 116].

Obtaining similar information about the stator-unit complex, however, has proven significantly more difficult. As this complex is fundamentally involved both in transmembrane ion passage and torque generation, atomic-level information of its structure is vital to our understanding of motor function. Investigations to this end have begun to be successful only recently, with the structure of the *Vibrio alginolyticus* stator-unit complex, PomAB [126]. The structure of the *E. coli* stator unit complex remains elusive.

Tethered cell experiments (1974)

The bacterial flagella is approximately 20 nm in width — too thin to be visualized using conventional optical microscopy. Furthermore, this several micron long filament moves rapidly, making characterizing motor rotation via the observation of flagellar motion prohibitively difficult. In 1973, Berg et al. showed strong evidence of rotational motion in bacterial flagella [11].

In 1974, Silverman and Simon overcame this obstacle by attaching cells to surfaces using antibodies [110]. In this way, motor rotation could be characterized via rotation of the tethered cell (see Figure 2.2B). The load of the cell body is such that the motor rotates at only a few hertz, ideal for direct observation by eye. This experimental design has stood the test of time, remaining a practical and easy method to study the motion of the bacterial flagellar motor.

Energy source (1977)

ATP is known as the standard cellular energy "currency". However, the flagellar motor is driven by a different energy source, the energy gained from the ion flux through the

eletrochemical potential across the bacterial cell membrane. This critical knowledge arose from two studies in 1977: It was shown that after starvation, swimming ability can be recovered through an artificial electrochemical potential in *Streptococcus* (strain V4051) [77] and, more specifically, by an artificial **proton-motive force** (PMF) in *Bacillus subtilis* [78]. Shortly after, a study conclusively showed that the PMF, not ATP, was the driving force behind motor rotation [52].

The proton-motive force is the sum of the electrical and chemical potential difference across a membrane (here, across the cellular envelope of the bacteria). It is given by:

$$\text{PMF} = V_m - Z\Delta\text{pH}, \tag{2.1}$$

where V_m is the membrane potential, and $Z = 2.303(\frac{RT}{F}) = 2.303(\frac{k_B}{e})$, in which R is the gas constant, T is the absolute temperature, F is Faraday's constant, k_B is Boltzmann's constant, and e is the electrical charge. The typical PMF for *E. coli* grown at pH 7.0 is approximately -170 mV. In 1995, the dependence of motor speed on the membrane potential V_m was shown to be linear (over the physiological range, i.e., up to -150 mV) by an experiment wiring motors to an externally controlled voltage source [49].

We note that there exist bacteria that utilize the gradients of ions other than protons — for example, alkalophilic bacteria are driven by sodium ions. The general term of Equation (2.1) for the **ion motive force** (IMF) is then:

$$\text{IMF} = V_m - Z\Delta\text{p(ion)} = V_m - Z\log\frac{[\text{ion}]_e}{[\text{ion}]_i}, \tag{2.2}$$

where p(ion) is the generalization of pH to any ion (i.e., the decimal cologarithm of the ion concentration, $-\log_{10}[\text{ion}]$), $[\text{ion}]_e$ and $[\text{ion}]_i$ are the extracellular and intracellular ion concentrations, respectively (see Figure 2.2C). Thus far, there has been only one ion flux measurement reporting that the BFM consumes roughly 1200 protons per revolution [83].

Stator resurrection (1984)

While the rotor of the BFM has been fairly deeply studied, the dynamics of the torque-generating stator units remain significantly more enigmatic. Each stator unit is a complex containing 4 MotA proteins, which contain the torque-generating domain that interacts with the rotor, and 2 MotB proteins, which contain the ion binding site and the domain that binds to the cell wall.

Resurrection experiments, which showed that the rotation speed of the motor can be recovered in a step-wise fashion in paralyzed (stator-less) mutants of *E. coli* via induction using Mot proteins, provided the first insight into the dynamics of these complexes [109, 18]. Resurrection experiments on tethered cells showed 8 step-wise jumps in speed [16]. Later, the development of the bead assay demonstrated that these experiments could be performed with various external loads [105]; in 2006, resurrection experiments using attached beads showed the existence of up to 11 independent stator units (see Figure 2.2D) [103].

When this experiment was performed at low loads, however, researchers observed only a single jump to the maximum observed motor speed [128]. This was interpreted to mean that, at near-zero external load, only one stator unit was needed to rotate the motor as fast as it could go [112]. This quickly led to a series of reworked theoretical models, all of which fit the constraint of a universal limiting speed. However, much like the report of a barrier to backwards rotation, this idea came under question several years after its conception, when it was found that motors at ultra-low load are able to maintain fewer stator units loads (1-2 vs. 8-11 near stall).

Application of external torque (1993) & the bead assay (2000)

The relationship between the motor torque and speed is one of the most fundamental dynamic features of the BFM. The first attempt to explore this relationship was a 1987 experiment that used metabolized cells of motile *Streptococcus* in different viscous environments [74]. However, as previously discussed, inferring the motor speed from observing flagellar motion is difficult and indirect. Furthermore, the estimated torque in these measurements also depended on several varying factors, such as the size of the cell body. Accordingly, it was measurements made using tethered cells that provided the first truly quantitative estimate of the torque-speed curve [12]. Further understanding the BFM's torque-speed relationship was made possible by two experimental leaps: the development of (1) methods to apply external torque to the motor, and (2) the bead assay.

These techniques proved particularly important to study this relationship in regimes that could not be reached using the limited range of loads allowed by tethered cell experiments. Experiments utilizing a rotating electric field (**electrorotation**) reported that there was a barrier to backwards rotation of the motor; that is, significantly more applied torque was required to rotate the motor slowly backwards than to rotate the motor slowly forwards or stall it [12]. The existence of such a barrier strongly hinted that the motor may operate using a **Brownian ratchet** mechanism, and several models were developed to this end. However, a few years later, optical trap experiments showed that this observed barrier was an artifact of the electrorotation method, and a flurry of revised, non-ratchet models soon followed [14].

But what about the other end of the universe? Tethered cell experiments left the low-load, high-speed regime of the motor totally unexplored. This was remedied by the discovery that beads of varying size could be attached to the flagellar stubs of adhered cell *bodies*, and used to observe motor rotation at a wide range of loads. The possibility of the **bead assay** was demonstrated decades earlier, but the yield was low [110].

However, during an investigation into the minimum size of functional bacterial flagellin, a hydrophobic flagellar mutant was discovered [62]; this "sticky" filament was then utilized in tethered cell experiments, and eventually to the bead assay with polystyrene beads [12, 29, 105]. Using this assay, the BFM torque-speed curve was shown to have two distinct regimes: (1) a constant torque at low speeds up until a critical "knee", after which (2) motor torque rapidly drops until the zero-load speed is reached (Figure 2.2F) [29].

Several further advancements in our understanding of this curve have been made in recent years: Resurrection experiments using the bead assay reported torque-speed curves for motors with different stator-unit numbers [105]. Currently, high-resolution data can be taken using a back-focal plane detection system for loads as low as 200 nm. To probe the ultra low-load region, smaller beads must be attached to the hook. To this end, gold nanobeads have been developed and, via several different detection methods [128, 113], nearly complete curves (i.e., curves extending almost up until the zero-torque speed) have been measured for the BFM [72].

Chimeric motors (2003)

The proton gradient drives the *E. coli* flagellar motor. As noted in Equation (2.1), varying the PMF requires changing either the bacterium's membrane voltage or the pH of the medium. Unfortunately, as robust as they may seem, even bacteria have their limits: Measurements on the BFM made over a wide range of PMF's have been stymied because bacteria cannot survive under such conditions.

Noting that several marine bacterial species have sodium-driven flagellar motors, researchers created the first chimeric sodium-driven BFM in *E. coli* in 2003 (see Figure 2.2C). To harness the electrochemical energy of the sodium ion gradient, the chimeric stator complex contains PomA, *Vibrio alginolyticus*'s analogue of MotA in *E. coli*; and PotB, a mash-up of PomB N-terminus and MotB periplasmic C-terminus [6]. Important electrostatic interactions between the stator and the rotor in *E. coli* were demonstrated to retain their role when PomA is part of the chimeric PomA/PotB stator in *E. coli* [134, 125]; interestingly, however, they are significantly less important for rotation in *V. alginolyticus* [127]. While able to reach higher motor speeds and torques than the wild-type proton-driven motor, the chimeric motor has been shown to be qualitatively similar to that of *E. coli* with regard to several properties, including the torque-speed relationship [55].

This swung the door into the study of the flagellar motor wide open — the coupling of sodium ions is far weaker than protons in *E. coli*, allowing quite a bit of flexibility in the ability of researchers to manipulate the ion-motive force [71, 73]. This ability was soon exploited, and single-cell measurements of the two separate components of the ion-motive force were reported [71, 73]. Using the bead assay, researchers also reported the torque-speed curves of motors at various, known IMFs; these measurements were also used to calculate the number of ions required for a revolution of the motor [72].

Observation of motor steps (2005)

Structural information on the motor provided the first hints as to its modus operandi: the M- and C-rings were shown to have 24- to 26-fold and 34- to 36-fold symmetry, respectively [116]. This, combined with the existence of independent torque-generating stator units surrounding the rotor, pointed towards the existence of a rate-limiting process in the rotor-stator interaction, and, accordingly, a discrete, "stepping" rotation.
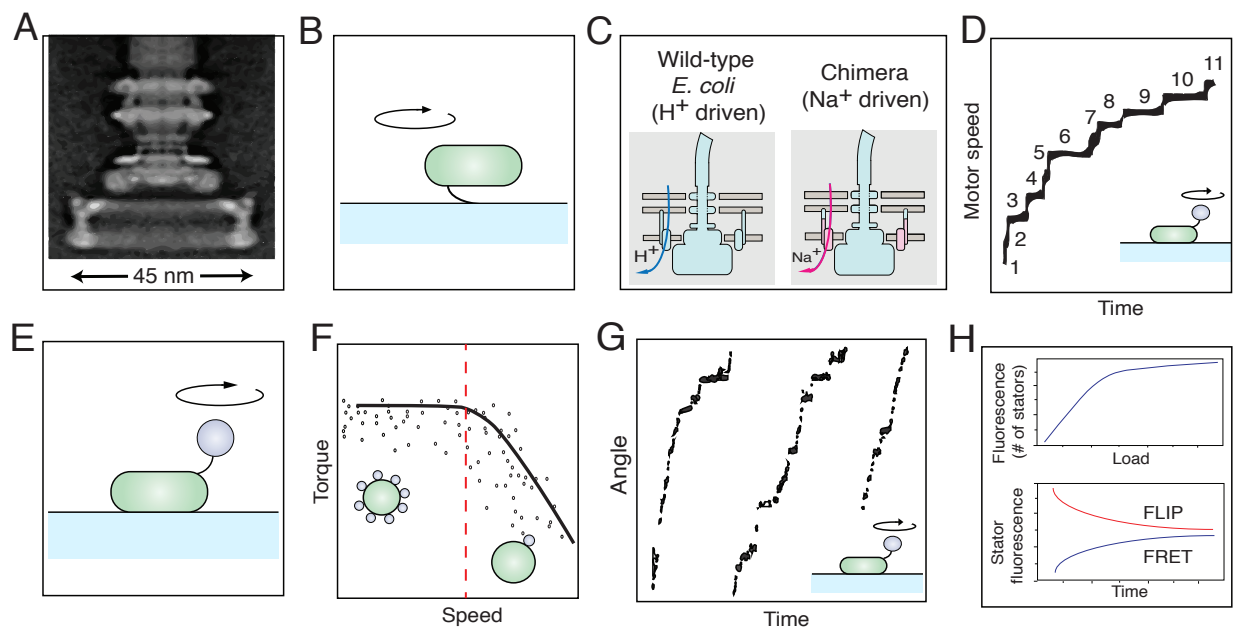
Figure 2.2: An overview of experimental landmarks. Note that this figure consists of cartoon schematics and does not contain any real data points or fits. (**A**) Electron microscopy image of the *Salmonella* flagellar motor basal body. Figure adapted from [10]. (**B**) The tethered cell assay allowed for direct characterization of motor rotation. (**C**) The BFM is unique in harnessing the energy stored in the transmembrane ion gradient instead of ATP. Wild-type *E. coli* motors are driven by the proton motive force. The development of sodium-driven chimeric motors eased the difficulty of studying motor energetics, as bacteria are far more sensitive to changes in pH than in sodium concentration. (**D**) Resurrection of paralyzed *mot* mutants demonstrated the existence of up to 11 independent torque-generating stator units. Figure adapted from [112]. (**E**) The bead assay, which involves observation of the rotation of small beads tethered to flagellar stubs, allowed for the characterization of motor dynamics across a wide range of external loads. (**F**) The torque-speed curve is the most fundamental dynamic measurement on the flagellar motor. The BFM's curve shows two distinct regions: a constant torque plateau up until a "knee", after which the torque rapidly falls until the zero-torque speed. Recently, it was discovered that the number of stator units a motor is able to maintain depends on external load: Motors at high load are able to maintain many more stator units than motors at low loads. Figure adapted from [90]. (**G**) The development of the bead assay and sodium-driven motors allowed for the direct observation of motor stepping behavior. Figure adapted from [114]. (**H**) Studies using fluorescently-labeled stator units showed that the structure of the motor was dynamic, with components constantly turning over and being exchanged with a pool of proteins in the membrane.

However, directly observing these steps has proven challenging for two reasons: (1) The BFM's symmetry hints at far smaller individual steps than other motors that exhibit large linear or rotational steps; these small discrete events are difficult to distinguish in the inherently noisy background of the nano universe. (2) Because motor behavior is observed via rotation of an external load (either a tethered cell body or bead), motor steps are further smoothed out by the flagellar hook, a soft spring.

This leads to a catch-22 of sorts: To counter the smoothing effect of the hook, motor rotation should be observed in the low-load regime. However, the motor speed is high under these conditions, making small steps exceedingly difficult to parse. This is where the development of the chimeric flagellar motor becomes particularly useful: Stepwise rotation is observable in the low-load regime when motors are slowed down by lowering the external SMF. The existence of 26 discrete steps per motor revolution were shown in de-energized chimeric *E. coli* motors (see Figure 2.2G) [114] and proton-driven de-energized *Salmonella* motors spinning both clockwise and counterclockwise [89]. Further experiments are needed to properly understand the energetic properties of the BFM at (ultra) low loads; recently, gold nanoparticles have made such exploration an exciting possibility [128, 113].

Dynamic turnover of motor components (2006) & load-dependent assembly (2013)

One of the most surprising results in the study of the BFM has been the discovery that motor components are constantly being turned over. Using the bead assay and high-resolution measurements of motor speed, small stepwise speed changes were observed in fully resurrected motors [103]. Later, experiments using fluorescently labeled MotB showed that stator units do not remain engaged to the motor, but are dynamically exchanged with a large pool of "waiting" complexes diffusing about in the cell membrane (see Figure 2.2H) [65].

The transition from liquid to surface living in bacteria (e.g., the formation of biofilms and swarming) is often triggered when bacteria "sense" they are near a surface. This has long been thought of as an indication that bacteria have some mechanosensing ability. The recent discovery that motors at high loads are able to maintain a much higher number of engaged stator units than motors at low load suggest that this ability may arise from the flagellar motor [68, 117], clearing a path towards an exciting new line of research to be explored.

While we have gained further insight into the mechanism behind stator dynamics, similar results have been obtained on the turn over of rotor components such as FliM [35, 131] and FliN [22, 34] in the C-ring. The dynamic turnover of rotor components, which serves to explain the symmetry variation observed in EM images, is believed to be related to switching in the BFM [34]. These emerging studies strongly suggest that adaptive remodeling is a common feature in the BFM, and, likely, in molecular motors in general.

2.2 Theoretical milestones

The ultimate question of how the flow of ions across the bacterial cell membrane is transduced into torque by the flagellar motor is a fundamental problem in molecular biophysics, requiring Deep Thought. Several models have been proposed over the years to tie together the various experimental measurements made on the motor into a coherent framework to describe the mechanochemical cycle of this machine. In the following section, we describe how hypothetical mechanisms for the flagellar motor have evolved, alongside experimental breakthroughs, since its initial discovery as the driving force behind bacterial swimming.

Oosawa and Hayashi (1986)

One of the first models to provide sufficient detail to quantitatively reproduce experimental observations on the relationship between motor speed and rotary torque was that of Oosawa and Hayashi [96]. An electron microscopy study found two rings, composed of several radially-arranged proteins, at the base of the flagellar filament [37]. Studies on the motility of bacterial cells after starvation provided evidence that this motor was driven by the flow from protons from the cell's exterior into the cytoplasm, quantifying for the first time the relationship between the motor's speed and membrane electrochemical gradient [77, 52].

The authors' ideas stemmed from these large experimental strides: they postulated a mechanism in which two concentric rings interact with each other to generate torque and rotate the motor. The authors supposed that the outer ring, the S-ring, was fixed to the cell membrane, while the inner ring, the M-ring, was attached to the base of the flagellum. Proteins along the periphery of S-ring were purported to alternate between two positions in order to shuttle protons across the membrane. The interactions of these molecules with analogous "outer" and "inner" tilted positions on the M-ring was implicated as the mechanism of torque generation in the motor; the broad minima of binding free energies due to the flexibility of the sites provided the source of the model's argument that ion flux was **loosely coupled** to motor rotation (i.e., each ion passing does not necessarily confer a full motor step).

Oosawa and Hayashi's paper was seminal in strongly arguing for the close interaction between theory and experiment, making it an appropriate starting point in our timeline of milestones in our theoretical understanding of the flagellar motor. Further, the authors emphasized that proper analysis and understanding of experimental data requires an underlying model, and that even a shortage of structural information should not discourage theorists from constructing quantitative, experimentally-testable models. At the time their model was constructed, it was not even known which parts of the motor might be rotating and which parts might interact with protons!

Model(s)	Class	Coupling	R-S interaction	Zero-torque speed
Oosawa & Hayashi	Ion turnstile	Loose	Not specified	Not specified
Läuger	Conformational change	Tight	Cross-bridge	Not specified
Meister et al.	Ion turnstile	Tight	Cross-bridge	Not specified
Berry	Ion turbine	Loose	Electrostatic	Not specified
Elston and Oster	Ion turbine	Loose	Elastic	Depends on paramaters
Xing et al.	Conformational change	Tight	Not specified	Decreases w/ stator number
Meacci and Tu	Conformational change	Tight	Not specified	Universal limiting speed
Mora et al.	Conformational change	Tight	Steric	Universal limiting speed
Mandadapu et al. & Ch. 3	Conformational change	Loose	Steric	Increases w/ stator number

Table 2.1: Comparison of fundamental model properties.

Läuger (1988)

As dynamic and structural experiments revealed more and more about motor function, so increased the number and specificity of modeling efforts. Torque-generating stator units were shown to not be a ring attached to the membrane, but instead possibly independent elements embedded in the cytoplasmic membrane peripheral to the rotor ring [109, 18]. Läuger proposed and analyzed possible kinetic mechanisms for motor rotation [64]. Two possible torque-generating interactions between the stator elements and the rotating M-ring were considered.

In Model I of [64], force is generated via the simultaneous interaction of a proton with elements on the stator and rotor as follows. Stator elements were thought to be affixed to the cell wall, each containing a ligand row perpendicular to the plane of the ring (Läuger correctly identified motB as a likely part of the stator complex). However, the interaction between an ion and one of these positions is not sufficient to remove it from solution: An energetic landscape favorable for ion passage occurs only at the intersection point between these and analogous ligand rows along the circumference of the M-ring, tilted with respect to those on the stators. This constrains the motion of the ion to this point alone, resulting in rotation of the M-ring with every ion passage.

The second model proposed by Läuger (Model II) differs from Model I in that the proton interacts with the stator and rotor sequentially rather than simultaneously. Ion translocation induces a conformational change in the stator elements, driving the movement of the rotor. The mechanism put forward by Model II of [64] is qualitatively similar to that of Oosawa and Hayashi's model, with the exception that it proposes that motor rotation is tightly coupled to ion flow. This property arises from the fact that the binding between the stator and rotor in both configurations ("outer-" and "inner-facing") is strong, in contrast to the broad minima seen in Oosawa and Hayashi's model. This requires that the transition between them (and thus, the passage of an ion) is tightly coupled to the movement of the inner ring — that is, each ion passing leads to a full motor step of a fixed size.

Meister et al. (1989)

Meister et al. proposed another tightly-coupled mechanism for torque generation in the motor. In this model, similar to those put forward by Läuger, stator elements are positioned along the periphery of the rotating M-ring [83]. Stators are equipped with channel complexes composed of two half-channels that span the membrane. Adjacent sites on the rotor align with these two half-channels, resulting in one site being in contact with the cytoplasm (the i-site) and the other with the extracellular medium (the o-site).

Motion of the stator relative to the M-ring is constrained as follows: the ends of the channel cannot move past an occupied site, while the center of the channel cannot move past an empty site. Consider a situation in which both extra- and intracellular sites are bound; then the channel can only move towards the i-site. If thermal motion carries it one step in this direction, the proton in the i-site is dropped off into the cytoplasm and the other bound proton moves into the intracellular position, allowing a proton from the extracellular medium to move into the empty o-site. This motion exerts a force due to the elastic linkage in the channel complex, inducing a rotation in the M-ring.

This model capitalized on the development of the tethered cell assay, and the subsequent improved ability to characterize the motor's torque-speed relationship in the intermediate range. Importantly, this model predicted that the torque required to drive the motor backwards would steeply increase, a claim which would be "proven" and then, interestingly, later "disproven" as various techniques to apply torque to tethered cells were developed and improved upon.

Berry (1993)

Improved structural and biophysical experiments on the flagellar motor provided much information into the structure and function of the motor's stator. The stator was found to consist of up to eight independent membrane-embedded *mot* units peripheral to the rotary rings, each capable of applying approximately equal torque to the rotor in either clockwise (CW) or counterclockwise (CCW) directions [18, 16]. Rotational directions are taken from the reference point of an observer looking at the plane from above throughout this thesis.

Given this information, Berry proposed a model in which alternating lines of high and low electrical potential are created along the perimeter of the rotor ring by the arrangement of positive and negative charges [13]. These lines are tilted with respect to the proton-conducting channels in the stators, such that protons flowing through the stator exert a long-range electrostatic torque on the rotor charges, forcing motor rotation.

This **ion turbine** model is structurally similar to Model II in [64], where protons are constrained at the intersection of two "half-channels" on the rotor and stator. However, it does not force tight coupling, instead relying on energetic constraints to keep protons close to the negatively-charged lines on the rotor. Furthermore, this model explicitly implicated an electrostatic force as driving both motor rotation and motor switching, contrary to previous

models which required a major conformational change for switching between CW and CCW modes.

Elston and Oster (1997)

Many windows into the function of the flagellar motor opened up with the development of biophysical techniques to apply torque to tethered cells. One such technique, electrorotation, applied torque to cells by high-frequency rotating electric fields and displayed an apparent barrier to backward rotation [15].

This result yielded support for models utilizing a thermal ratchet mechanism for motor rotation. One of these was another "ion turbine" model proposed by Elston and Oster [42]; the authors presented this model in the context of a motor with stator elements that were either fixed or movable. In the fixed-stator case, Elston and Oster's model is similar to Berry's, purporting that motor rotation was driven by electrostatically-driven torque.

However, the movable stator case removes the requirement of a continuous proton path between the extracellular surface and the cytoplasm; the authors point out that such a physical separation facilitates the operation of a proton turbine, as it lowers the probability of proton movement without motor rotation due to thermal oscillations alone. Additionally, while the movable stator case still implicated electrostatic forces generated by tilted lines of alternating high and low potential along the rotor's periphery in torque-generation, it additionally considered the contribution of elastic and steric forces caused by conformational changes in the stator.

Though the results of early electrorotation experiments brought about a series of models based on the fact that there was a steep barrier to backwards rotation, later experiments with optical tweezers showed that this was actually an artifact: In fact, the motor generated the same torque when rotated slowly forwards or backwards [14].

This result excitingly turned the field upside down and forced researchers to reconsider one of the fundamental features of most published models. Interestingly, the next "round" of models took a cue from Elston and Oster's movable-stator model: With evidence that there was no innate energy barrier to backwards rotation, a power-stroke driven by conformational changes in the stator elements became a likely contender for the flagellar motor's torque-generating mechanism.

Xing et al. (2006)

A deeper exploration of the relationship between motor speed and rotary torque became possible with two experimental developments: electrorotation (described previously) and the bead assay. In the bead assay, rather than observing rotating cell bodies tethered to glass slides by their flagella the rotation of polystyrene beads attached to flagellar stubs was analyzed [105]. Because beads far smaller than cell bodies were able to be used, this assay allowed the measurement of motor dynamics over a far larger range of torques than in previous experiments.

Both techniques showed the same result: the flagellar motor's torque did not simply vary linearly with speed as previously thought, but instead displayed two regimes. At a fixed PMF, the torque generated by the motor was nearly constant up to approximately 170 Hz at 23°C. Past this speed, the torque drops rapidly and linearly, reaching zero at approximately 300 Hz.

This new information into motor behavior was incorporated by Xing et al. into a model with four physical "ingredients": (1) load and motor are connected via a soft elastic linkage; (2) motor rotation is tightly coupled to ion flux; (3) motor rotation is driven by proton-driven conformational changes in the stator units; (4) the proton channel in the stator is gated by rotor movement. The third assumption was supported by experimental evidence of such a change in the stator complex [60]; it is worth noting that, after these experiments, most models implicated a conformational change in stator structure to drive motor rotation. However, because of a lack of atomic-level structural information of the motor, the authors chose to keep the details of the stator-rotor interaction vague beyond these four constraints [123].

Meacci and Tu (2009)

Two (more) surprising discoveries about the function of the flagellar motor came in quick succession. First, due to increases in experimental resolution the motor was shown to proceed by steps at low speeds [114]. Second, "resurrection" experiments (described previously) seemed to show that motor speed at low loads was independent of stator number; that is, when the external load is near zero, one stator seemed to be able to rotate the motor as fast as it can go [128]. In particular, the idea that the zero-torque speed must be independent of stator number led to the development of several new models.

Meacci and Tu proposed a kinetic model that explained this behavior based on the assumption that the stepping rate of the stator elements was dependent on the torque exerted on the rotor, analogous to the Huxley model for myosin — that is, "negative" torque between the rotor and a stator element (i.e., torque opposite the direction of motor rotation) increases the stator stepping rate [80, 79]. This results in a zero-torque speed dependent only on the maximum stepping rate, but independent of the number of stator elements, as Yuan and Berg's experiments predicted [128].

This kinetic model also intrinsically reproduced the motor's observed stepping behavior by the inclusion of two timescales in a single mechanochemical cycle: the waiting time t_w depending on the chemical transition of the stator and the moving time t_m determined by the mechanical rotation of the rotor ring. A future iteration of this model addressed the absence of a barrier to backwards rotation through the inclusion of a back-stepping probability [79].

Mora et al. (2009)

In step with Meacci and Tu, Mora et al. also capitalized on these new insights to propose a simple physical model for motor rotation [87, 86]. Their model relied on two main assumptions: (1) All stator elements work in unison, applying torque to the motor simultaneously

and additively and (2) this torque is imparted via a contact force between the stator and the rotor. Each stator complex was modeled as a set of protein springs that detach and reattach from successive sites along the rotor's circumference with each ion passage. This simple physical model, in which the stator drives a "bumpy" rotor through a viscous medium, fundamentally utilized the physical structure of the motor and was shown to be consistent with all the experimental data available at the time.

2.3   In conclusion

The bacterial flagellar motor's fundamental role in facilitating several biological processes has made it one of the most well-studied molecular machines. The BFM is far more complex than any other molecular machines we have known. The history of research on the BFM is a prime example of how valuable the close interplay between theory and experiment can be. We hope that our own model, previewed in Figure 2.1 and Table 2.1 and discussed in greater detail in the next chapter, continues in this tradition.

Atomic knowledge of the stator unit structure is crucial to our ability to understand motor function and build more detailed, predictive models. Many experiments remain necessary to validate the recent model predictions of the motor's fundamental mechanochemical cycle. Even the basic question of whether the BFM's rotation is loosely or tightly coupled to ion flux has not yet been definitively answered. Furthermore, the recent discoveries reporting the dynamic nature of motor structure have opened up a whole new avenue of research on how the BFM has evolved to interact with and adapt to its environment.

Finally, and importantly, a theme which we hope arises repeatedly and clearly in this thesis is that "reality" is often inaccurate: Even questions long believed to be closed must be periodically critically examined when new information arises. Models must constantly be updated as new experimental evidence arises, and theorists must always be aware and take account of all available knowledge in order to be able to provide the momentum for future experiments.

So, for the new generation of biophysicists: "Don't Panic." There is still a lot to learn!

Chapter 3

A few hundred Hz of solitude: single-stator motors

"Time was not passing...it was turning in a circle."

— Gabriel García-Márquez, *One Hundred Years of Solitude*

In the previous chapter, we provided an overview of past experimental and theoretical research on the BFM. Our purpose of this inclusion was twofold: Firstly, we of course wanted to show how strongly this nanomachine has piqued the scientific community's interest. However, it is our belief that great research not only answers questions, but, importantly, asks new ones as well. To this end, we hope we have also highlighted how many mysteries remain regarding the function of the flagellar motor.

Indeed, the difficulties in obtaining structural information about the motor, as well as the modest magnitude of the forces involved relative to thermal fluctuations [10], have made it challenging to pinpoint a specific physical origin behind the rotor-stator interaction. Previous models have avoided making this commitment, instead treating the interaction between the stators and the rotor phenomenologically as a free energy surface and the stator as an *ad hoc* stochastic stepper [123, 87, 80, 79].

We point out that, of course, a conclusive, full understanding of the torque-generating mechanism in the flagellar motor requires a crystal structure of the stator complex. But there is no need to sit around twiddling our thumbs until then! The available structural knowledge, combined with information about the motor's dynamical performance, is sufficient to propose a plausible model that is experimentally testable.

In the spirit of the work chronicled in Chapter 2, this chapter collates this information to present a theoretical mechanical model for torque generation, the predictions from which are in turn used to propose several validation experiments.

While we primarily discuss experiments utilizing the proton (H^+)-powered motor of *Escherichia coli*, our model is sufficiently general so as to apply to the sodium (Na^+)-powered motors found in alkalophiles and marine *Vibrio* species. Our model for torque generation involves a proline-induced conformational change in the MotA cytoplasmic loops [31, 58]. To the best of our knowledge, the model presented in this chapter is the first to incorporate known structural information about the BFM stator and rotor complexes into a quantitative physical mechanism for the generation of the power stroke.

In the following we first lay out a detailed description of the proposed mechanism, with frequent and interspersed references to experimental results on which model assumptions were based. Then, we address several model predictions, that either serve to explain existing experiments or propose new validating ones.

3.1 Two steps to torque

Due to the modest magnitude of the forces involved relative to thermal fluctuations, it has long been assumed that nearly any form of interaction between rotor and stator is sufficient to explain the rotation of the BFM. Here, using all experimental evidence available to us, we conclude that the power stroke of the flagellar motor is driven by both electrostatic and steric forces. Our proposed mechanochemical model consists of two phases: (i) Prior to the power stroke, electrostatic forces position the stator. (ii) Once positioned, the stator delivers a steric push (i.e., a **contact force**; for more information on the nature of these forces, see Appendix A) on a FliG protein located along the periphery of the rotor.

Electrostatic forces steer the stator into place

The first step in constructing our model is the steering and positioning of the stator by electrostatic forces. This hypothesis originates from the results of the mutagenesis experiments performed by Zhou et al. [133]. These studies were aimed at elucidating the structure of the MotA loops. They found that mutations of certain charged residues on the cytoplasmic portions of the loops degraded—but did not eliminate—motor function. Notably, the deleterious effect of mutations on the stator were often countered by corresponding mutations (in particular, compensating charge reversals on the FliGs). Certain mutations were also found to have very small effects, or even slight improvements, in bacterial motility.

These results correspond to the idea that mutations of charged residues may result in imperfect steering and consequently in a less efficient—but still functioning—power stroke. Similarly, certain mutations may position the cytoplasmic loops closer to the adjacent FliG, resulting in a larger power stroke and corresponding improved motility.

Because, as mentioned previously, detailed structural information on the stator is not yet available, we performed a simple example calculation to demonstrate how electrostatic interactions can position the stator ready for a power stroke. For computational convenience, we approximate the important charged residues on the FliG proteins [26] and stator loops [134] implicated in torque generation. The assumption that FliG proteins can be modeled as dipoles is based on previous studies [66, 26]. Modeling the electrostatic forces between the stator and rotor by point charge interactions produces results comparable to those obtained from a dipole approximation.

Dipole approximation. We denote the rotor dipole moment as $\vec{p}_R^{\,k}$, where $k \in \{1 \dots 26\}$ enumerates the number of FliGs on the rotor periphery. Likewise, the stator dipole moment

is denoted as $\vec{p}_S^{\,i,N}$, where N enumerates the number of stator units, and i the number of loops on a single stator. Here, for ease of exposition, we show electrostatic calculations for a single stator with a single loop ($i = 1$ and $N = 1$), but note that this calculation can be easily extended to the full stator model.

We calculate the electric field felt by the stator loop as:

$$E = \sum_{k=1}^{26} E_k, \tag{3.1}$$

where

$$E_k = \frac{1}{4\pi\epsilon|\vec{r}_k|^3} \left[3(\vec{p}_R^{\,k} \cdot \hat{r}_k)\hat{r}_k - \vec{p}_R^{\,k} \right]. \tag{3.2}$$

Here ϵ is relative permittivity of cytoplasm and $\vec{r}_k$ is a vector quantity of the distance between the stator loop and the kth FliG; $\hat{r}_k$ is the normalized unit vector denoting its direction and $|\vec{r}_k|$ is its scalar magnitude. Except where noted explicitly, this notation is used throughout.

From E_k, we calculate the interaction energy between the dipole on the stator loop $\vec{p}_S$ and the kth FliG $\vec{p}_R^{\,k}$ as:

$$U_k = -\vec{p}_S \cdot E_k \tag{3.3}$$
$$= \frac{1}{4\pi\epsilon|\vec{r}_k|^3} \left[(\vec{p}_R^{\,k} \cdot \vec{p}_S) - 3(\vec{p}_R^{\,k} \cdot \hat{r}_k)(\vec{p}_S \cdot \hat{r}_k) \right].$$

Similar to the calculation for total energy, we have

$$U_{\text{stator}} = \sum_{k=1}^{26} U_k. \tag{3.4}$$

Note that, as the distance from the stator loop increases, the terms in the total energy sum drop off as $\frac{1}{|\vec{r}|^3}$, and so the contribution by FliGs located far from the stator loop is negligible.

To calculate the total energy in the system, we also add in the interaction energies between pairs of FliG molecules. However, we note that their relative positions do not change as the stator rotates, and so this consideration results simply in a translation of the entire landscape and has no effect on the topology.

$$U_{\text{total}} = U_{\text{stator}} + \sum_{i=1}^{26} \sum_{j=1,j\neq i}^{26} \frac{1}{4\pi\epsilon|\vec{r}_{i,j}|^3} \left[(\vec{p}_R^{\,i} \cdot \vec{p}_R^{\,j}) - 3(\vec{p}_R^{\,i} \cdot \hat{r}_{i,j})(\vec{p}_R^{\,j} \cdot \hat{r}_{i,j}) \right], \tag{3.5}$$

where $\vec{r}_{i,j}$ is the displacement vector between the ith and jth FliG.

Comparison with calculation using point charges. We also performed the above calculations using point charges for the relevant residues on FliG and MotA loops. Because of the uncertainty in the position of the charges, we are interested primarily in a qualitative
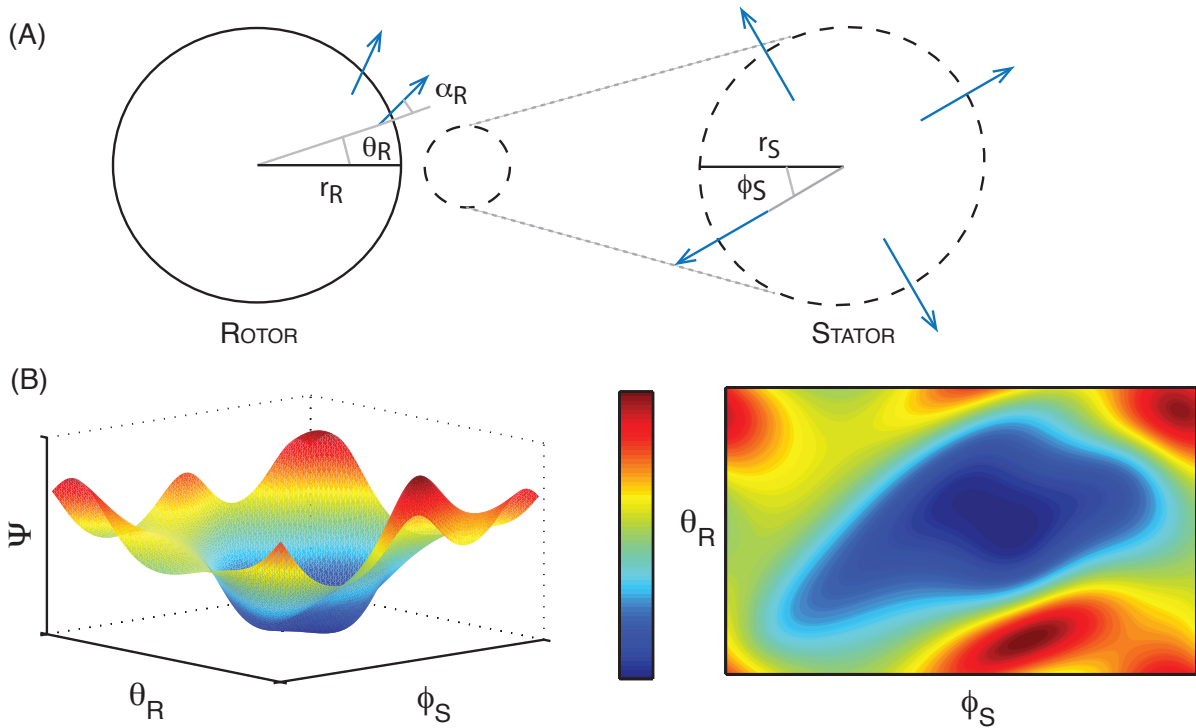
Figure 3.1: The predicted energy landscape during electrostatic steering. **(A)** Schematic of rotor and stator configurations. ϕ_S and θ_R are the angular coordinates of the stator and the rotor with respect to their contact point (denoted by the horizontal above); α_R is the positive angle of the individual FliGs with respect to the radius. Blue arrows denote the direction of the dipole [66, 26]. **(B)** Predicted surface and contour plots of the electrostatic energy vs. the stator and rotor angles. The predicted surface shows the existence of a wide and gently sloping energy well. Note that ϕ_S and θ_R are periodic variables with periods $\pi/2$ and $\pi/13$, respectively; the above plots show one period of each. Our calculations consider a single stator centered at (21,-2,1) with the rotor centered at the origin (all distances in nm). Computations using this dipole approximation suggest a well of depth ~ 1 $k_B T$ for this configuration.
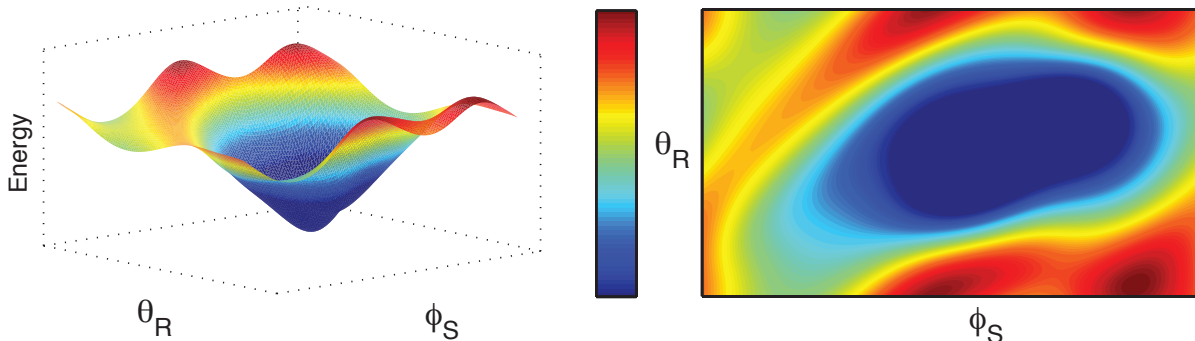
Figure 3.2: Energy landscape during "electrostatic steering" calculated using point charges rather than dipoles. All parameters are defined as in the text; the stator is centered at (21,-2,1) and the rotor is centered at the origin (all distances in nm).

affirmation of our approximation — that is, the existence of a gently sloping, relatively wide energy well.

As in our dipole calculations, we consider the charged residues on the FliG to be positioned at $\frac{\pi}{4}$ to the horizontal (i.e., the charges are positioned along the dipole as shown in Figure 3.1). Similarly, we position the charges on the stator loop along the dipole, positioned radially outward from the stator center. Given this configuration, we calculate the electrostatic energy as

$$U_{\text{pc}} = \underbrace{\sum_{i=1}^{8} \sum_{j=1,j\neq i}^{8} \frac{q_i q_j}{4\pi\epsilon |\vec{r}_{i,j}|} e^{-|\vec{r}_{i,j}|/\lambda_D}}_{\text{Interaction between stator charges}} + \underbrace{\sum_{i=1}^{52} \sum_{j=1,j\neq i}^{52} \frac{q_i q_j}{4\pi\epsilon |\vec{r}_{i,j}|} e^{-|\vec{r}_{i,j}|/\lambda_D}}_{\text{Interaction between FliG charges}} \tag{3.6}$$

$$+ \underbrace{\sum_{i=1}^{8} \sum_{j=1}^{52} \frac{q_i q_j}{4\pi\epsilon |\vec{r}_{i,j}|} e^{-|\vec{r}_{i,j}|/\lambda_D}}_{\text{Interaction between charges on stator and FliGs}}.$$

We screen charges using a Debye length of $\lambda_D = 0.5$ nm. As before, $\vec{r}_{i,j}$ denotes the displacement vector between charge i and charge j; the magnitude of these charges are denoted by q_i and q_j, respectively. Note that, similar to our dipole calculations, the first two terms of the energy are invariant to rotation of the stator. Therefore, they only serve to translate the entire energy landscape and do not affect the topology.

As shown in Figure 3.2, the topology generated is indeed similar to that using the aforementioned dipole approximation. The removal of certain charges may modify the energy landscape via a flattening or widening of the energy well. In conjugation with our electrostatic steering hypothesis, this may point to a possible explanation for experimental studies which show that mutation of charged residues reduce, but do not eliminate, motor function.

Our methods can easily be extended using positional information from solved structures to more quantitatively analyze the effects of these charges.

Centering the stator. The distribution of observed rotor step-sizes has been shown experimentally to be centered around $\frac{2\pi}{26}$ radians ($\sim 13.8°$), the average spacing between consecutive FliGs [114, 89]. The positioned charges result in a weak electrostatic force that is sufficient to position the MotA loop without significantly wasting energy to free the stator at the end of the power stroke. Furthermore, the width of the well leads to somewhat imprecise positioning. While this result is hardly unexpected, the wide spread of this distribution—in particular, the tendency towards smaller step sizes—has been somewhat puzzling.

Because a wide energy well may result in stators being positioned at "nonoptimal" locations, electrostatic positioning may contribute to this variance. Since we propose that the stator's power stroke is imparted via a contact force on the rotor, imperfect electrostatic positioning will result in the stator being in contact for only a portion of its trajectory. This results in the stator delivering a stroke that is smaller than average. Of course, imperfect steering is not likely to be the only factor determining the variance in the observed step-size distribution: the uneven spacing of FliG's along the periphery of the rotor [8, 98], as well as experimental errors, are also likely to contribute.

There is little structural information for the stator of the BFM. Therefore, in our calculations, we choose a possible position of the stator which is consistent with our model and experimental results. Firstly, we center the stator so that all four stator loops are able to access the FliG molecules. The occasionally observed backsteps imply that both pairs of loops must be able to execute a power stroke during motor function.

Preliminary calculations strongly suggest that the loop charges cannot be in plane with the charges on the FliG. The close proximity of the charges results in an electrostatic interaction far too strong to be feasible given the known efficiency of the BFM (i.e., far too much energy would be wasted in "letting go"). In-plane configurations which do not present both extremely steep and deep wells must place the stator out of reach of the FliGs.

Given these considerations, and noting that the stator and rotor have radii of respective lengths ~ 2 nm and ~ 20 nm, we center the stator at $(x_S, y_S, z_S) = (21, -2, 1)$ using a coordinate system with the rotor centered at the origin.

Note that, in the case of a "reciprocal" motion of the stator, attractive electrostatic forces strong enough to comprise the entire power stroke would require a non-negligible energy to separate the stator and the rotor at the end of the power stroke. This penalty for "letting go" would likely obviate the rotor torque, resulting in a motor with a far lower Stokes efficiency [121] than has been calculated for the BFM ($\sim 95\%$) [10]. In contrast, the mechanism we propose here efficiently generates mechanical work from the ion-motive force.

We note that the above calculation is speculative: changes in parameter choices will vary the resulting energy landscape. However, our mechanism presupposes that the energy well produced by the electrostatic interactions will be shallow and wide (Figure 3.1). We have performed an example calculation to show that such a mechanism is feasible given our
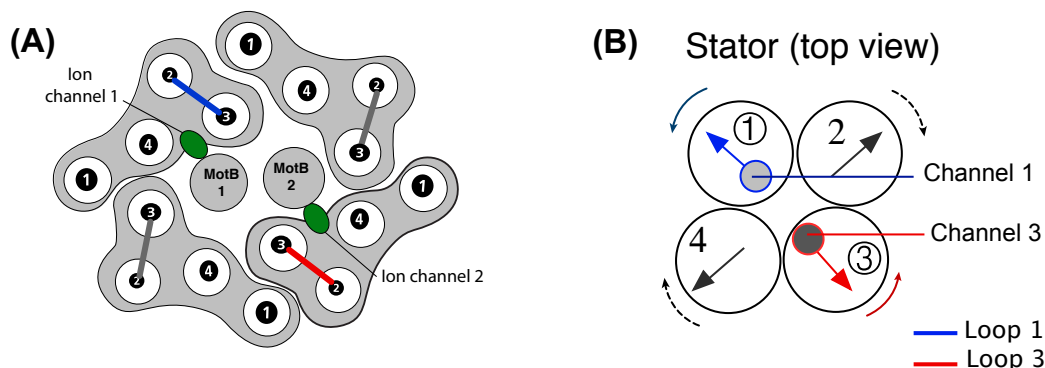
.

Figure 3.3: Stator structure and coordinated motion between stator subunits. **(A)** Proposed arrangement of stator components as viewed from the periplasm. A stator has four MotA helix bundles, each consisting of four α-helices. The four MotA subunits surround a pair of MotB helices. The ion channels associated with the MotB's (shown in green) contain the Asp32 residue essential for proton binding. The stator is attached to the peptidoglycan via a linker region on MotB. The power stroke is delivered to the rotor FliGs by the cytoplasmic loops between helices A2 and A3 in each MotA bundle (shown as solid bars). Loops 1 and 3 (highlighted in blue and red, respectively) are associated with the ion channels. Adapted from Braun et al. and Kim et al. [23, 58]. **(B)** Due to the helical structure of the MotA loops, we can make an analogy between their motion to that of a bundle of four gears. Our model proposes that Loops 1 and 3 (shown in blue and red, respectively) drive CCW rotation via contact with FliG, while Loops 2 and 4 drive CW rotation.

limited structural information. A more precise calculation can be performed only when more detailed structures are available.

Motion about a proline hinge provides a steric push

There are four MotA subunits in each stator complex; see Figure 3.3 for a schematic of the stator structure. Our model supposes that two of these subunits are inactive during torque-generation while the motor is moving predominantly in a single direction. We base this presumption on the idea that switches between counterclockwise (CCW) and clockwise (CW) rotation result from changes in FliG orientation [66]. Given this, we propose that two MotA loops are responsible for the power stroke in one direction, while the other two interact with the alternately oriented FliG to drive rotation in the other direction. We suppose that loops 1 and 3 are responsible for CCW motion and loops 2 and 4 for CW motion, but note that this designation is arbitrary. This mechanism predicts that the intrinsic mechanics for power strokes in both directions are equivalent; this has been observed experimentally [89].

We propose that an elementary step is composed of a pair of power strokes, analogous

to the mechanism of a two-cylinder engine. Experiments on motors driven at extremely low speeds may allow the direct observation of these substeps, in support of our model. This can be done using chimeric sodium-driven flagellar motors. As extremes in sodium concentration are tolerated far more easily than extremes in pH, these chimeric motors can be driven at very low sodium motive forces (SMFs). Thus far, speeds as low as 10 Hz have been obtained [114].

A two-ion mechanism can either be "in-phase", in which the energetic profiles of the two stator loops are identical, or "anti-phase", in which their dynamics are offset by a half-cycle. In an experiment using a slowly-driven chimeric motor, measuring the rate-limiting step between mechanical substeps can differentiate between these two scenarios. For example, if slower ion-binding (e.g., by lowering IMF) extends the dwell time between half-steps, the out-of-phase engine model is supported.

The mechanics of these two scenarios are equivalent within the framework of our model. For this reason, we discuss only one of these mechanisms in detail: the one in which the two stator loops act in-phase with each other (as shown in Figure 3.6B). We choose this alternative because the passage of two protons across a membrane provides more energy, which contributes (along with the work done by the MotA loops) to a more reliably directional process in the presence of thermal noise. Interestingly, a single proton passage under standard conditions generates $\sim$6 k_BT, slightly less than the calculated length of "time's arrow" (the energy barrier required for a such a reliably directional process) [44].

As proposed previously [58], we assume that the steric portion of the power stroke is the result of a conformational change in the cytoplasmic MotA loop. Evidence of such conformational changes have also been shown experimentally [60]. In our model, this motion consists of hinged movements of the MotA helices that result in a **"kink and swivel"** motion, as shown in Figure 3.4 [31]. The steric mechanism proposed below remains valid regardless of which residue, or group of residues, on the MotA/MotB helices acts as the inducer. However, we have chosen to focus on MotA's Pro173 residue because: (i) along with Asp32 on MotB, this amino acid is strongly conserved across bacterial species [24], and (ii) previous molecular dynamics simulations have found that proline residues induce hinges in transmembrane helices [31], resulting in a movement analogous to the one proposed in the model. The specific mechanism we propose is as follows.

When a cation binds to the negatively charged Asp32 residue on MotB, the hydrogen bonds (including those of water) in the vicinity of Asp32 and Pro173 on the A3 helix of MotA collectively rearrange. This rearrangement induces an elastic strain in the MotA-MotB complex centered around the proline residue in the A3 loop of MotA. Figure 3.4A shows a candidate scenario, where the carbonyl group of residue 169 on MotA forms a hydrogen bond with Asp32 on MotB after proton binding, as proposed in [58]. This elastic strain induces the kink and swivel movement around the proline residue and drives the proposed motion of the lower part of the A3 helix, constituting the power stroke (see Figure 3.4B). The binding of the ion and the rearrangement of the hydrogen bonds (10^{-12} to 10^{-9} s) are near-instantaneous processes as compared to the much slower motion of the kink and swivel conformational change (10^{-5} to 10^{-3} s). Thus the chemical steps can be treated as
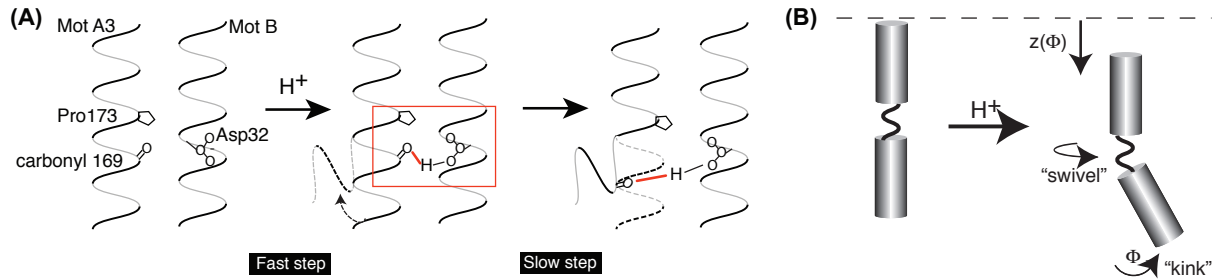
Figure 3.4: Ion binding onto Asp32 induces a "kink and swivel" conformational change [31]. **(A)** Binding of a proton to Asp32 of MotB drives a rapid local reorganization of hydrogen bonds (including those of water). In particular, we focus on the creation of a hydrogen bond between the side chain of MotB's Asp32 and the carbonyl group of MotA's residue 169. Ion binding thus creates a local elastic strain in the MotA helix. The release of this strain leads to the proposed conformational change in MotA about the Pro173 residue. Adapted from Kim et al. [58]. **(B)** Upon ion binding, MotA undergoes a rapid conformational change consisting of three motions: (i) a bending about Pro173 ϕ, (ii) a downward motion, $z(\phi)$, and (iii) a rotation about its central axis. Inspired by the work of Cordes et al. [31], we propose that this "kink and swivel" motion generates the power stroke. Importantly, we note that this figure is a two-dimensional depiction of a three-dimensional process, with the motion of the loop extending out of the plane of the page.

transitions between states in a Markov chain.

The above proposal is supported by a few simple calculations. The maximum torque of the BFM in *E. coli* is $\sim$2000 pN-nm [14]. Given that up to 11 torque-generating units may be acting, this corresponds to a maximum motor torque of $\sim$200 pN-nm per stator [103]. As the radius of the motor is $\sim$20 nm, the force generated by a single stator during a power stroke is $\sim$10 pN. Direct observation of stepping behavior have shown that the motor takes 26 elementary steps per revolution, corresponding to a displacement of $\sim$5 nm per step. As explained below, our model supposes that each elementary step is actually composed of two half-steps, each imparted by the power stroke of a MotA helix. This results in a displacement of $\sim$2.5 nm per power stroke. Molecular dynamics studies show the angles subtended by proline hinge motifs from various transmembrane helices to be between 18-25° [31]. From this, we can estimate the length of the cytoplasmic loop measured from the proline hinge to its tip to be $\sim$7 nm, a reasonable estimate as the majority of the stator residues have been shown to extend into the cytoplasm [133]. Such a lever arm would result in $\sim$25 pN-nm ($\sim$6-8 k_BT) of work per half-step, corresponding to the rearrangement of 1-2 hydrogen bonds (and the free energy released by the passage of one proton). This energy barrier is sufficient to ensure an efficient directional process, as suggested in [44].

Model equations

The mechanochemistry of the torque-generation cycle of a flagellar motor with a single stator unit can be modeled by the following **Langevin equations**. The dynamics of the angular positions of the stator loops $\phi_S^i(t)$, $i \in \{1, 3\}$ are given as:

$$\zeta_S \frac{d\phi_S^i}{dt} = \underbrace{-\frac{\partial G}{\partial \phi_S^i} \ell_p}_{\substack{\text{Torque from} \\ \text{Proline hinge}}} - \underbrace{\frac{\partial V_{RS}}{\partial \phi_S^i}}_{\substack{\text{Reaction} \\ \text{from rotor}}} - \underbrace{\frac{\partial \psi}{\partial \phi_S^i} \ell_p}_{\substack{\text{Electrostatic} \\ \text{attraction}}} + \underbrace{\sqrt{2 k_B T \zeta_S} f(t)}_{\text{Thermal fluctuations}} . \tag{3.7}$$

The left-hand side of the equation is the viscous rotational drag (remember that, because we are in a low Reynolds number environment, inertial forces are inconsequential). The right-hand side then is the corresponding torque balance, consisting of the torque exerted on the rotor by the proline hinge of the stator, the reaction torque from the rotor, and the electrostatic attraction between the two. These are given as the gradients of potentials described in detail in the following paragraphs. As in the following equations, the last term is the stochastic Brownian force, where $f(t)$ is uncorrelated white noise.

ζ_S is the effective drag coefficient of the stator. $G = G(\phi_S^i, j)$ denotes the free energy of stator loop i, modeled in Figure 3.6B as a **Landau potential**. However, because of thermal fluctuations the exact shape of the potentials is immaterial. Accordingly, we approximate this potential by piecewise quadratic functions for ease of computation. The parameter $j \in \{0, 2\}$ corresponds to the chemical state of the system: $j = 2$ if two protons are bound to the MotB helices and $j = 0$ if not. The switching between the two chemical states corresponds to a "jump" between potential curves, as shown in Figure 3.6B.

As the stator moves between the two configurations, it induces a contact force, and subsequent torque, on the rotor. Unlike previous models, we do not assume that this torque is constant across loads, but rather depends on the ζ_L. To this end, we do not allow a linear interaction potential between the stator and the FliG; this would result in a constant applied force, which is not true for contact forces. We model the steric interaction potential V_{RS} as

$$V_{RS}(\phi_S^i, \theta_R) = \begin{cases} -F_{RS} \frac{(R\theta_R - \ell_P \phi_S^i)^2}{X_{RS}} & \text{if } 0 \leq X_{RS} + R\theta_R - \ell_p \phi_S^i \leq X_{RS} \\ 0 & \text{otherwise,} \end{cases}$$

where $X_{RS} + R\theta_R - \ell_p \phi_S^i$ denotes the distance between the position of the stator loop and the nearest FliG. From this, the torque on the rotor is calculated as $\tau_{\text{contact}} = -\partial V_{RS}/\partial \theta_R$, while the corresponding reaction torque on a stator loop is given by $\tau_{\text{reaction}} = -\partial V_{RS}/\partial \phi_S^i$.

The charges on the FliG and the stator loop exert weak attractive forces on each other. These forces prevent the drifting of the rotor with respect to the stator during the chemical transition events. With the contact torque and the weak electrostatic forces, the total instantaneous torque on the rotor is given by $\tau = \tau_{\text{contact}} - R(\partial \psi / \partial \theta_R)$. The average torque on the rotor is a time (or ensemble) average of the instantaneous torque. Finally, the rotor and load are connected by a linear spring with elastic constant κ; the elastic coupling terms in the equations for the rotor and the load thus appear with opposite signs.

Given this, the rotor dynamics are described by a corresponding Langevin equation:

$$\zeta_R \frac{d\theta_R}{dt} = \underbrace{-\frac{\partial V_{RS}}{\partial \theta_R}}_{\text{Torque}\atop\text{from stator}} - \underbrace{\frac{\partial \psi}{\partial \theta_R}R}_{\text{Electrostatic}\atop\text{attraction}} \underbrace{- \kappa(\theta_R - \theta_L)}_{\text{Connection}\atop\text{to load}} + \underbrace{\sqrt{2k_B T \zeta_R} f(t)}_{\text{Thermal fluctuations}} , \tag{3.8}$$

where ζ_R is the effective rotor drag coefficient. Finally, the dynamics of the load are then driven by the motion of the rotor:

$$\zeta_L \frac{d\theta_L}{dt} = \underbrace{\kappa(\theta_R - \theta_L)}_{\text{Spring connection}\atop\text{to rotor}} + \underbrace{\sqrt{2k_B T \zeta_L} f(t)}_{\text{Thermal fluctuations}} . \tag{3.9}$$

As above, ζ_L is the effective drag coefficient of the load.

The above model can be collapsed to explicitly include only the dynamics of a stator with a single loop that generates torque both during its bending (ϕ_S^i increasing) and unbending (ϕ_S^i decreasing). This description is isomorphic to the mechanism described previously (see Figure 3.6) because the mechanics of the two half power strokes are equivalent as described above. The equations corresponding to this reduced model are:

Stator : $$\zeta_S \frac{d\phi_S}{dt} = \underbrace{-\frac{\partial G(\phi_S, j)}{\partial \phi_S}\ell_p}_{\text{Torque from}\atop\text{Proline hinge}} - \underbrace{\frac{\partial V_{RS}}{\partial \phi_S}}_{\text{Reaction torque}\atop\text{from rotor}} - \underbrace{\frac{\partial \psi}{\partial \phi_S}\ell_p}_{\text{Electrostatic}\atop\text{attraction}} + \underbrace{\sqrt{2k_B T \zeta_S} f(t)}_{\text{Thermal fluctuations}}$$

$$\tag{3.10}$$

Rotor : $$\zeta_R \frac{d\theta_R}{dt} = \underbrace{\frac{\partial V_{RS}}{\partial \theta_R}}_{\text{Torque}\atop\text{from stator}} - \underbrace{\frac{\partial \psi}{\partial \theta_R}R}_{\text{Electrostatic}\atop\text{attraction}} - \underbrace{\kappa(\theta_R - \theta_L)}_{\text{Spring connection}\atop\text{to load}} + \underbrace{\sqrt{2k_B T \zeta_R} f(t)}_{\text{Thermal fluctuations}} \tag{3.11}$$

Load : $$\zeta_L \frac{d\theta_L}{dt} = \underbrace{\kappa(\theta_R - \theta_L)}_{\text{Spring connection}\atop\text{to rotor}} + \underbrace{\sqrt{2k_B T \zeta_L} f(t)}_{\text{Thermal fluctuations}} . \tag{3.12}$$

In Equation (3.10), the internal force driving the stator due to the rearrangement of hydrogen bonds caused by a proton binding event is denoted by $-\frac{\partial G}{\partial \phi}$. Here, $G(\phi, j)$ denotes the free energy of the stator. Due to the fact that thermal fluctuations are of a comparable magnitude to the free energies considered, the exact shape of the potentials is relatively unimportant. For ease of computation, we approximate the potential using a piecewise linear function. During each mechanical power stroke, the force is constant and positive. At other times, there is little elastic strain on the MotA loops, and accordingly, the force is negligible.

The torque generated by the stator is dependent on the applied load ζ_L, as a natural consequence of steric forces. A general discussion of the nature of contact forces, as well as

the explicit formulation of the steric interaction potential V_{RS}, is provided in Appendix A. The contact torque applied to the rotor (Equation (3.11)), and consequent reaction torque applied to the stator (Equation (3.10)), are given by $\tau_{\text{contact}} = \frac{\partial V_{RS}}{\partial \theta_R}$ and $\tau_{\text{reaction}} = \frac{\partial V_{RS}}{\partial \phi_S}$, respectively.

Additionally, as described previously, the charges on the FliG and the stator loop also exert weak attractive forces on each other. These forces prevent the drifting of the rotor with respect to the stator during the chemical transition events. In the above equations, we denote this term via the term $-\frac{\partial \psi}{\partial \theta_R} R$, as it detracts from the repulsive torque imposed by the steric force of the stator.

The rotor and load are connected by a linear spring with constant κ; the elastic coupling terms in the equations for the rotor and the load thus appear with opposite signs (Equations (3.11) and (3.12), respectively). The elastic constant in the experiments can vary depending on the length of the hook when attaching the bead. In some cases, the hook is very short or is stiffened by an antibody linker. This corresponds to a large spring coefficient [20, 19].

As previously [123], we ensure that chemical transitions are localized near potential minima. We choose rate constants for these transitions such that detailed balance is maintained.

We conclude our technical discussion of our model with some specifics on the interaction potentials used and some comments on the ion kinetics important for implementation. A full copy of the simulation code used can be provided upon request.

Interaction potentials

Here, we provide explicit forms of the free-energy potentials in terms of the order parameters we choose to describe the motion of the stator and the rotor.

Stator potentials. The order parameter describing the motion of the stator is the angle subtended by the stator loops $\phi_S^{1,3}$ with respect to the vertical MotB ion channels. When two ions bind to the Asp32 residues, the two loops undergo a conformational change from their straight ($\phi_S^{1,3} = 0°$) to bent state ($\phi_S^{1,3} = 20°$). In this work, we have assumed that the stator loops move in-phase. Therefore, as previously, we model the two stator loop configurations using a single collective parameter ϕ_S.

Before the ions bind to the Asp32 residues, the motion of the stators is governed by the potential $G_1(\phi_S)$ where the minimum is around $\phi_S = 0°$ as shown in Figure 3.5. When two ions bind to two Asp32s, the stator potential switches from G_1 to G_2. This compels the stator angle to move from $\phi_S = 0°$ to $\phi_S = 20°$.

During this transformation, the loop pushes the rotor via a steric force. At the end of the conformational change, when the loops are at the minimum of the potential G_2, the two ions bound to two Asp32s exit into the cytoplasm. The potential then switches back to G_1 and the loops traverse back to $\phi_S = 0°$. During this time, the loops apply a contact force on the same FliG as in the previous substep (see Figure 3.5).

As noted previously, thermal fluctuations are of the same order of magnitude as the free energies considered and the precise form of the potentials is not important. In our
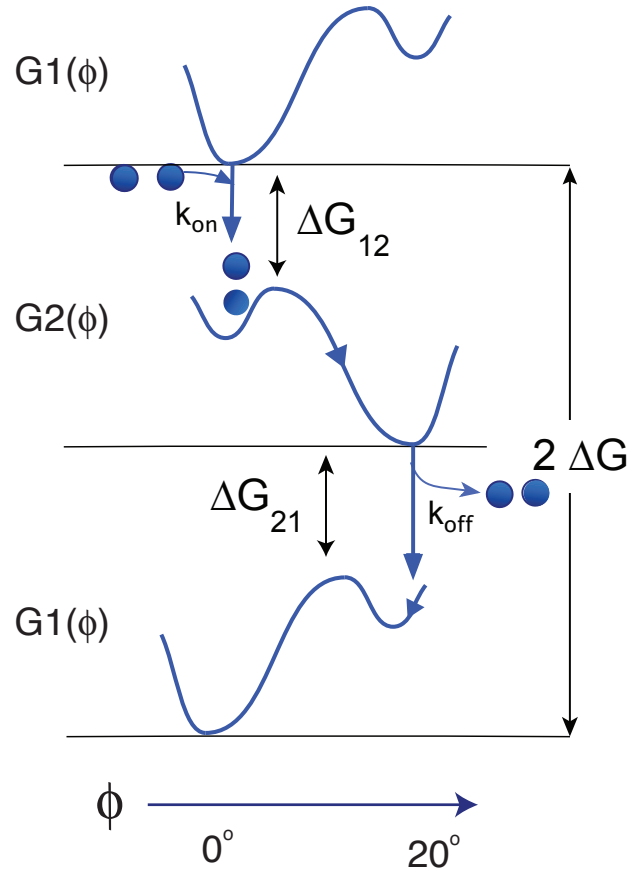
Figure 3.5: Schematic of the internal stator potentials used in our mechanistic model.

simulations, we choose:

$$G_1(\phi) = \begin{cases} \beta\phi^2 & \text{if } \phi \leq 0 \\ F_p\phi & \text{if } 0 \leq \phi \leq \phi_{\text{max}} \\ F_p\phi_{\text{max}} + \beta(\phi - \phi_{\text{max}})^2 & \text{if } \phi \geq \phi_{\text{max}} \end{cases}$$

and

$$G_2(\phi) = \begin{cases} \beta\phi^2 & \text{if } \phi \leq 0 \\ -F_p\phi & \text{if } 0 \leq \phi \leq \phi_{\text{max}} \\ -F_p\phi_{max} + \beta(\phi - \phi_{max})^2 & \text{if } \phi \geq \phi_{\text{max}}. \end{cases}$$

Here, β is the parameter for the tension in the system when ϕ is either less than 0 or greater than ϕ_{max} and F_p is a scaling parameter for the force exerted by the proline hinge.

Rotor-stator interaction potential. The steric force between the stator and the rotor can be simulated using a soft linear repulsive force with a cutoff distance X_{RS}.

$$V_{RS}(\phi_S^i, \theta_R) = \begin{cases} -F_{RS}\frac{(R\theta_R - \ell_P\phi_S)^2}{X_{RS}} & \text{if } 0 \leq X_{RS} + R\theta_R - \ell_P\phi_S \leq X_{RS} \\ 0 & \text{otherwise,} \end{cases}$$

For convenience, we denote $x_{RS} = X_{RS} + R\theta_R - \ell_p\phi_S$, the distance between the position of the stator loop and the nearest FliG. The torque on the rotor can be obtained as $\tau_{\text{contact}} = -\frac{\partial V_{RS}}{\partial \theta_R}$:

$$\tau_{\text{contact}}(x) = \begin{cases} -F_{RS}R\frac{R\theta_R - \ell_P\phi_S}{X_{RS}} = F_{RS}R\left(1 - \frac{x_{RS}}{X_{RS}}\right) & \text{if } 0 \leq x_{RS} \leq X_{RS} \\ 0 & \text{otherwise.} \end{cases}$$

Likewise, the reaction torque on the stator is $-\frac{\partial V_{RS}}{\partial \phi_S}$. F_{RS} is the maximum force that can be applied by the proline hinge. All other parameters are defined as described previously.

Note that we assume that weak electrostatic forces place the stator at most 0.5 nm from the nearest FliG on the rotor ($X_{RS} \sim 0.5$ nm) prior to the start of the power stroke. During the half step, the stator moves from $\phi_S = 0°$ to $\phi_S = 20°$. In this process, a contact force is applied on the rotor when $0 \leq x_{RS} \leq X_{RS}$. The contact force is zero when $x_{RS} \geq X_{RS}$.

All previous theoretical studies of the BFM have chosen to model the interactions between the stator and the rotor as a load-independent force. In the above sections, we have shown that the dependence of steric forces on the load reproduces many of the mechanical characteristic features of the motor found in experiments (e.g., the nonlinearities in the relationship between speed and stator number at high loads).

While the exact form of the potential used to model the rotor-stator interaction is not very important, we note that linear potentials cannot be used. Such potentials result in a constant torque, independent of ζ_L, and thus do not reproduce several properties of steric forces.

Kinetics of ion-binding

Here, we will describe how to model ion-binding events as part of the Langevin equation framework. In many problems related to motors, the ion-binding events may occur only in a certain window of a continuous coordinate describing the mechanical motion of the system. In the BFM, there are two main ion-binding events involved in the torque-generation cycle.

1. Two cations (here, protons) from the periplasm bind to the Asp32 residue on two MotBs or unbind into the cytoplasm when the cytoplasmic loops are straight.

$$\text{Asp32}^- + \text{H}^+_{\text{periplasm}} \underset{k_{21}}{\overset{k_{12}}{\rightleftharpoons}} \text{Asp32-H} \tag{3.13}$$
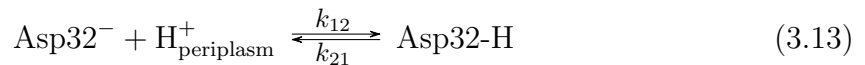
2. Once the protons are bound, the cytoplasmic loops undergo conformational change from the straight state into the bent state. At the end of the conformational process,

the two channels close with respect to the periplasm and instead open towards the cytoplasm. Once this occurs, the two protons unbind from Asp32 residues into the cytoplasm (or, in the reverse reaction, bind from cytoplasm to Asp32).

$$\text{Asp32-H} \underset{\tilde{k}_{21}}{\overset{\tilde{k}_{12}}{\rightleftharpoons}} \text{Asp32}^- + \text{H}^+_{\text{cytoplasm}} \tag{3.14}$$
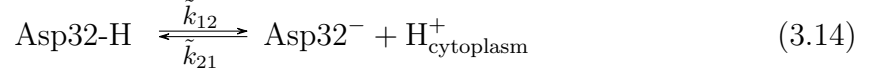
First, we will describe the case for the kinetics at equilibrium (i.e., at zero IMF), followed by the procedure to model the kinetics under a non-zero IMF.

Equilibrium kinetics under zero IMF. In the following we consider the proton-driven motor of *E. coli*, and so the IMF concerned is the proton motive force (PMF). When there is no PMF, the forward and backward reaction rates for the reaction in (3.13) must satisfy

$$\frac{k_{12}}{k_{21}} = \frac{[\text{Asp32-H}]}{[\text{Asp32}]} \ . \tag{3.15}$$

Let the equilibrium dissociation constant of reaction (3.13) be defined as

$$\text{K}_a^p = \frac{[\text{Asp32}][\text{H}^+_{\text{periplasm}}]}{[\text{Asp32-H}]} \ . \tag{3.16}$$

If $\text{pK}_a^p = -\log_{10}\text{K}_a^p$, then the forward and backward rates should satisfy

$$\frac{k_{12}}{k_{21}} = 10^{(\text{pK}_a^p - \text{pH}_{\text{periplasm}})} \ . \tag{3.17}$$

Note that the acid dissociation constant value of pK_a^p should be determined from experiments. A similar relation to the above can be derived for the reaction in (3.14).

Kinetics under non-zero IMF. To satisfy detailed balance when the PMF is non-zero, the kinetic coefficients for the reaction should satisfy

$$\frac{k_{12}}{k_{21}} = 10^{(\text{pK}_a^p - \text{pH}_{\text{periplasm}})} \exp\left(\frac{e\psi_p + G_1 - G_2}{k_B T}\right) \ . \tag{3.18}$$

There exist multiple choices for the expressions k_{12} and k_{21}. For convenience and symmetry, we choose the following for the rate constants :

$$k_{12} = 10^{-\text{pH}_{\text{periplasm}}} \exp\left(\alpha\left(\frac{e\psi_p + G_1 - G_2}{k_B T}\right)\right) \ , \tag{3.19}$$

$$k_{21} = 10^{-\text{pK}_a^p} \exp\left(-(1-\alpha)\left(\frac{e\psi_p + G_1 - G_2}{k_B T}\right)\right) \ . \tag{3.20}$$
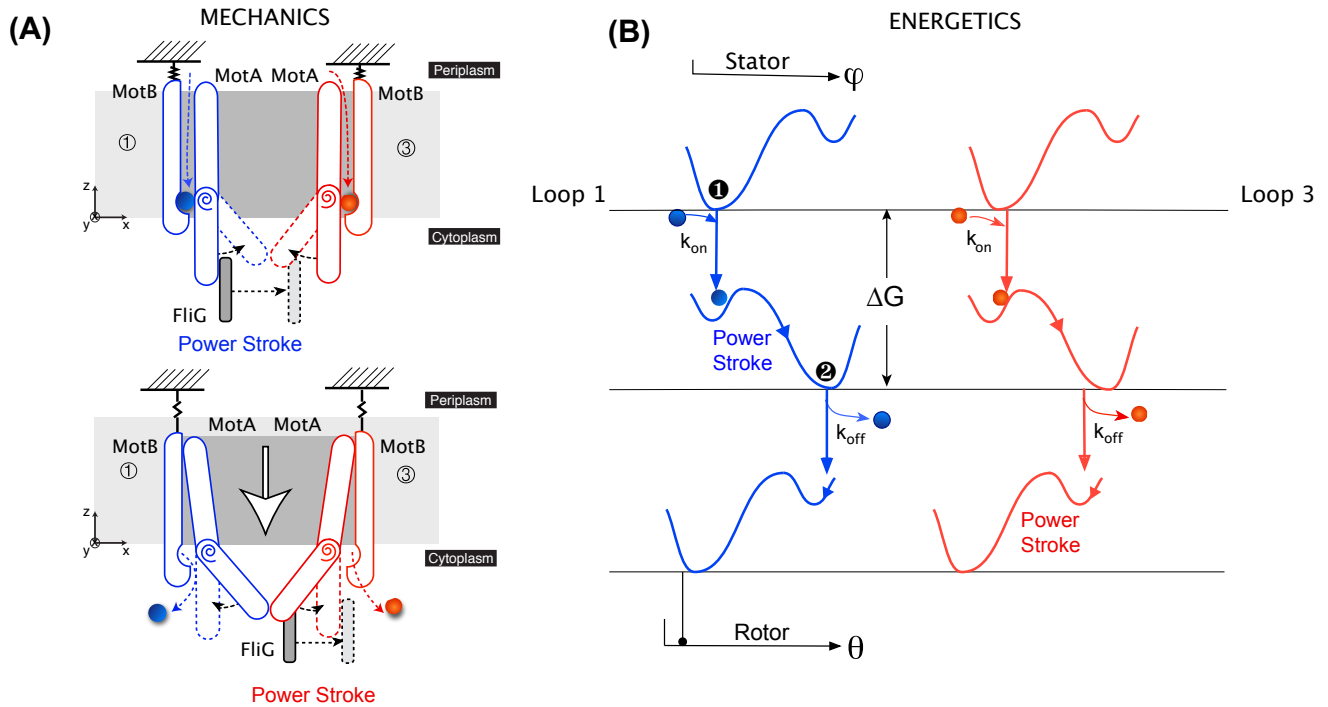
For symmetry, we have chosen $\alpha = 0.5$.

Figure 3.6: Dynamics of the rotor-stator interaction. **(A)** MECHANICS OF THE POWER STROKE. *Top panel:* After the initial electrostatic steering, two protons bind to the charged Asp32 residues on the MotB's. The consequent rearrangement of hydrogen bonds induces an elastic strain in the straight MotA loops. Release of this strain results in synchronous "kink and swivel" motions about the proline 'hinge' in both MotA's. As a result, a steric push is imposed on FliG, and the first half of the power stroke performed by Loop 1. Importantly, this motion also has a vertical component—the loops lower themselves out of the membrane. *Bottom panel:* The lowering of the MotA loops exposes the protons in MotB to the cytoplasm, where they are released. This results in a "reset" of the MotA loops, during which Loop 3 carries out the second half of the power stroke. We note that this image depicts a two-dimensional projection of a three-dimensional motion: the motion of the stators is not constrained to the plane of the page. **(B)** ENERGETICS OF THE POWER STROKE. Because the two loops move in-phase with each other in our model, their energetic pictures are identical. We describe the free energy landscapes using double-well Landau potentials. These landscapes are shown in blue for Loop 1 and red for Loop 3 with respect to the angles of the stator ϕ and rotor θ. We model the stator and rotor interaction using a steric force. This ensures that their motion, and the values of the corresponding angles, are very tightly tied to one another. The initial entrance of the proton into the ion channel (k_{on}) places the system within $k_B T$ of the energy barrier. Thermal motions then result in the first half of the power stroke (*Top and middle panels*). The exit of the protons into the cytoplasm (k_{off}) results in the "reset", and the second half of the power stroke (*Middle and bottom panels*).

Summary

Figure 3.6A depicts the mechanics associated with the power-stroke. We choose the angle subtended by a stator loop ϕ_S^i with respect to the bilayer normal (where i corresponds to the loop number) as the order parameter. That is, we consider the energy landscape along the arc length of the mechanical trajectory of the stator loop. A stator loop has two stable configurations: straight ($\phi_S^i = 0°$) and bent ($\phi_S^i \sim 20°$). Both of these configurations correspond to energy minima in different chemical environments: when the negative Asp32 is not neutralized by a proton, the loops prefer to maintain a straight posture ($\phi_S^i = 0°$). The presence of bound protons induces a free energy change sufficient such that thermal fluctuations can induce the conformational change to the bent state ($\phi_S^i \sim 20°$).

During a power stroke, the entire stator complex undergoes a collective gear-like motion as shown in Figure 3.3B. The conformational change due to the "hopping on" of the ion produces the first half of the power stroke: here, loop 1 pushes the FliG, while loop 3 is put in place to carry out the second half of the power stroke during the reset (Figure 3.6A). This "reset" corresponds to the "hopping off" of the proton, resulting once again in the the stator loops surmounting the energy barrier between configurations and reverting to the straight position ($\phi_S^i = 0°$). Note that the numbering of the loops is arbitrary; the mechanism proposed here is equivalent to one in which loop 1 performs the first half of the power stroke and loop 3 the second.

In summary, a torque-generation cycle by a single stator of the bacterial flagellar motor proceeds as follows:

1. Electrostatic interactions between charged residues on MotA and FliG steer a stator tip close to a rotor FliG.

2. In the presence of a membrane potential, the two MotB aqueous ion channels open and two protons bind to the negatively charged Asp32 residues on the MotBs. This triggers a reorganization of the hydrogen bonds in the vicinity of the Pro173 on MotA (see Figure 3.4A).

3. The hydrogen bond rearrangements induce elastic strain in the straight MotA loops. This strain drives a "kink and swivel" motion of the MotA loop, increasing the bend angle (from $\phi_S^i = 0°$ to $20°$, as shown in Figure 3.4B).

4. One MotA loop (Loop 1, shown in blue in Figure 3.6A) applies a steric push to the nearest FliG, resulting in one-half power stroke.

5. At the same time, the movement of the stator ion binding pocket moves downward so that the pocket is exposed to the cytoplasm. The ion-channel is now closed to the periplasm. The protons "hop off" MotB into the cytoplasm, now inverting the strain in the bent MotA loops .

6. The inverse strain drives the movement of the loops in the reverse direction, straightening the bent MotA's (i.e., from $\phi_S^i \sim 20°$ to $0°$).

7. The other MotA loop (Loop 3, shown in red in Figure 3.6A) now applies a steric push to the same FliG, completing the second half of the power stroke.

Consequently, to the rotor, the stator appears to be an "inch-worm" stepper with FliGs as the "stepping-stones".

3.2   Fits and predictions

Single-stator motors exhibit concave torque-speed curves. Until recently, BFM experiments have been performed on motors with multiple stators, with no direct accounting for the number of engaged stators at a given load. Therefore, the existence of the torque-speed "plateau" and "knee" have been assumed to be innate characteristics of the rotor-stator interaction, largely because there was no evidence to the contrary. However, Lo et al. [72] performed experiments using a chimeric single-stator motor showing smoother torque-speed curves without a dramatic plateau as observed for wild type motors. While these curves are still concave in shape, the extent of the plateau regions are quite variable, and depend on the IMF.

The physics behind the two regimes of the torque-speed curve have been interpreted by previous models as a competition between waiting and moving timescales [123, 80]. Thus the general concave shape is largely independent of the exact structural and mechanistic details of the model. It requires only that the model is tightly coupled and the moving time exceeds the waiting time at high loads. Our model for single-stator motors fulfills both of these properties.

Our simulations show torque-speed relationships consistent with single-stator experiments (Figure 3.8B). The behavior of the torque-speed curves results from a competition between the time taken for a mechanical half-step (T_M) and the waiting time between ion-binding events (T_W). For example, our simulations show that the average time in moving a half-step $\langle T_M \rangle$ can be ∼20 ms at high loads and ∼0.01 ms at low loads. The average waiting time under standard conditions $\langle T_W \rangle$ is ∼0.2 ms [80]. Therefore, at low loads, the motor is in a kinetically limited regime, where the waiting time between steps is generally higher than the time required to complete a step. Conversely, the motor is mechanically limited at high loads when $\langle T_M \rangle > \langle T_W \rangle$, resulting in the observed plateau. Consequently, as shown in Figure 3.8B, this plateau region grows smaller as the IMF decreases (i.e., as $\langle T_W \rangle$ increases).

This competition is also manifested in the relationship between speed and IMF: speed depends linearly on IMF at high loads, but in a slightly nonlinear fashion at low loads (Figure 3.8C). Given that the rotor moves $2\pi/26$ radians per step, the speed of the rotor (ω_R) can be approximated as:

$$\omega_R \approx \frac{2\pi}{26} \times \frac{1}{\langle T_M \rangle + \langle T_W \rangle}.$$

At high loads, $\langle T_M \rangle \gg \langle T_W \rangle$. Because the time to complete a power stroke is inversely proportional to the ion-motive force, $\langle \omega_R \rangle \propto$ IMF at high loads. In contrast, the waiting time
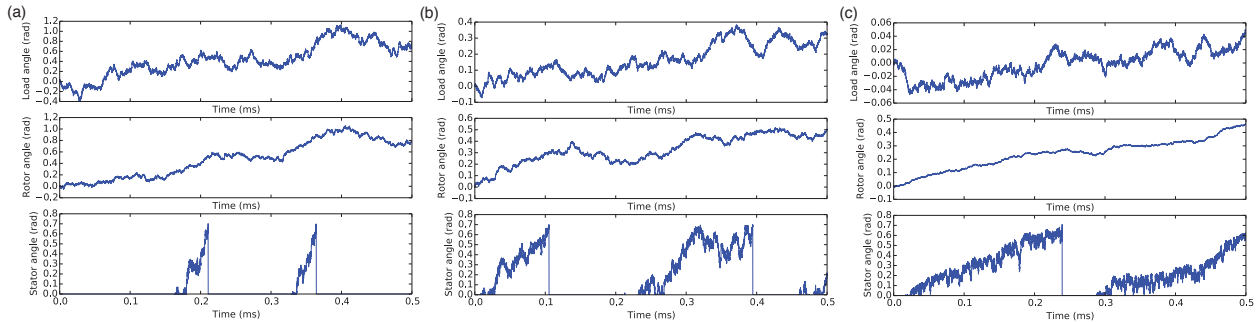
Figure 3.7: Simulation output (0.5 ms) for a single-stator motor at **(a)** $\zeta_L = 0.005$ pN-nm-s-rad^{-1}, **(b)** $\zeta_L = 0.05$ pN-nm-s-rad^{-1}, and **(c)** $\zeta_L = 0.5$ pN-nm-s-rad^{-1}. The duration of stator steps (bottom panel) increases with load, decreasing the relative amount of a mechanochemical cycle taken up by the waiting time between subsequent steps.

eclipses the time for a mechanical step at low loads, and therefore $\omega_R \propto 1/\langle T_W \rangle \propto \exp(q \times \text{IMF}/k_B T)$ (see Figure 3.7). This relationship is explicitly explored in our previous discussion on ion-binding kinetics; the consequences of this are further explored in our discussion on multi-stator motors (see Chapter 4).

A full revolution requires the passing of at least 52 protons. Our model for torque generation assumes that each elementary power stroke is tied directly to the passage of protons across the membrane. Given our prior assumption of 26 elementary steps per revolution, our model thus requires 52 protons for a full revolution. Previously, a lower bound for the number of ions per full revolution was determined by calculating the work done as $\langle \tau \rangle \times 2\pi$ and equating it to the free energy $n \times \text{IMF}$, where n is the number of ions per revolution and IMF is the ion motive force, as before [72]. The above calculation resulted in an estimate of $n = 37$, lower than the 52 ions per revolution supposed by our model.

This discrepancy can be explained as follows. While the above is indeed a lower bound, a tighter bound can be computed. The calculation of work as stated above suggests that the power output per revolution is $\widetilde{P} = \langle \tau \rangle \langle \omega \rangle$. However, power is formally calculated as $P = \langle \tau \cdot \omega \rangle$, which differs from $\widetilde{P}$ by a covariance term, $\text{cov}(\tau, \omega)$. This follows from the fact that, for any two stochastic processes X and Y, $\langle XY \rangle = \langle X \rangle \langle Y \rangle + \text{cov}(X, Y)$. So, the calculation of $\widetilde{P}$ as in [72], which gives a value of $n = 37$ ions per revolution, is missing this covariance term. Given the physical relationship between τ and ω, this omitted term is always positive, and so it is quite feasible that the actual value of n is 52 ions per revolution as predicted by our model.

Note that the number of protons per revolution assumed by our model is also a lower bound; that is, we have assumed that 52 *working* ions are required per revolution. Many factors can result in the passing of more ions than predicted, including leakiness of the ion channels, loose coupling between the rotational and vertical movements of the stator,

irregular arrangement of FliG's around the rotor, or imperfect placement of stators by electrostatic steering forces. Our mathematical framework can easily be extended to include this by replacing the step function associated with ion binding with a sigmoidal function.

Using the mathematical model described, we performed both analytic calculations and numeric stochastic simulations. Statistics from simulated trajectories—an example of which is shown in Figure 3.8A—were used to calculate various experimental quantities including average motor torque and angular speed.

In the sample trajectory for the rotor motion, the duration of a power stroke (T_m) and the waiting time between consecutive power strokes (T_w) are highlighted in orange and purple, respectively. The highlighted power stroke shows two half-steps, corresponding to the two sequential steric pushes by the two MotA loops involved. As in experimental trajectories, occasional reverse steps are also observed in our simulations, one of which is shown in the sample path in Figure 3.8A. An explanation for back-steps that is compatible with our model is provided below.

The results shown in Figure 3.8 were obtained via simulation. Analytic calculations on an approximate deterministic model were also performed for illustrating different aspects of the model (see Chapter 4). These calculations were also used to obtain suitable ranges for the parameters (e.g., stator and rotor drags) used in Langevin simulations.

Backstepping in the absence of CheY-P. The BFM plays a central role in bacterial chemotaxis: the direction of rotation of the motor determines whether a bacterium will move in a straight line (CCW) or "tumble" (CW) to move in a random new direction. This switching is typically initiated via a signal transduction pathway, in which a response regulator protein, CheY, is phosphorylated into an activated form, CheY-P, to induce tumbling. For more information on this pathway and bacterial chemotaxis, we refer the reader to several excellent reviews [119, 100].

However, occasional backsteps (e.g., CW motion during primarily CCW rotation) are observed even in the absence of CheY-P. This has been attributed to microscopic reversibility. For example, Mora et al. ascribed switching in the BFM to the diffusive motion of the rotor through a "bumpy" 26-fold periodic potential [87]. However, recent structural studies have found that there exist two main configurations for the FliGs [66, 89], lending support to the idea that flipping between these states is the molecular basis for backstepping. We note that despite a general agreement on the *existence* of two distinct FliG configurations, the exact nature of the conformational change to the CCW direction remains controversial.

In our model, the probability of observing a backward step is equivalent to the probability of finding a FliG oriented in the CW state (assuming a primarily CCW-rotating motor). Within the framework of our model, whenever a FliG changes its state and is close to a stator, then the stator uses loops 2 and 4 to apply a contact force and pushes the FliG in the CW direction. To model the flipping between CW and CCW states for the FliGs, we use a nearest-neighbor periodic **Ising model** with the 26 FliGs arranged on a one-dimensional ring. Such models have been used to explain rotational switching (see, e.g., [40, 7]).
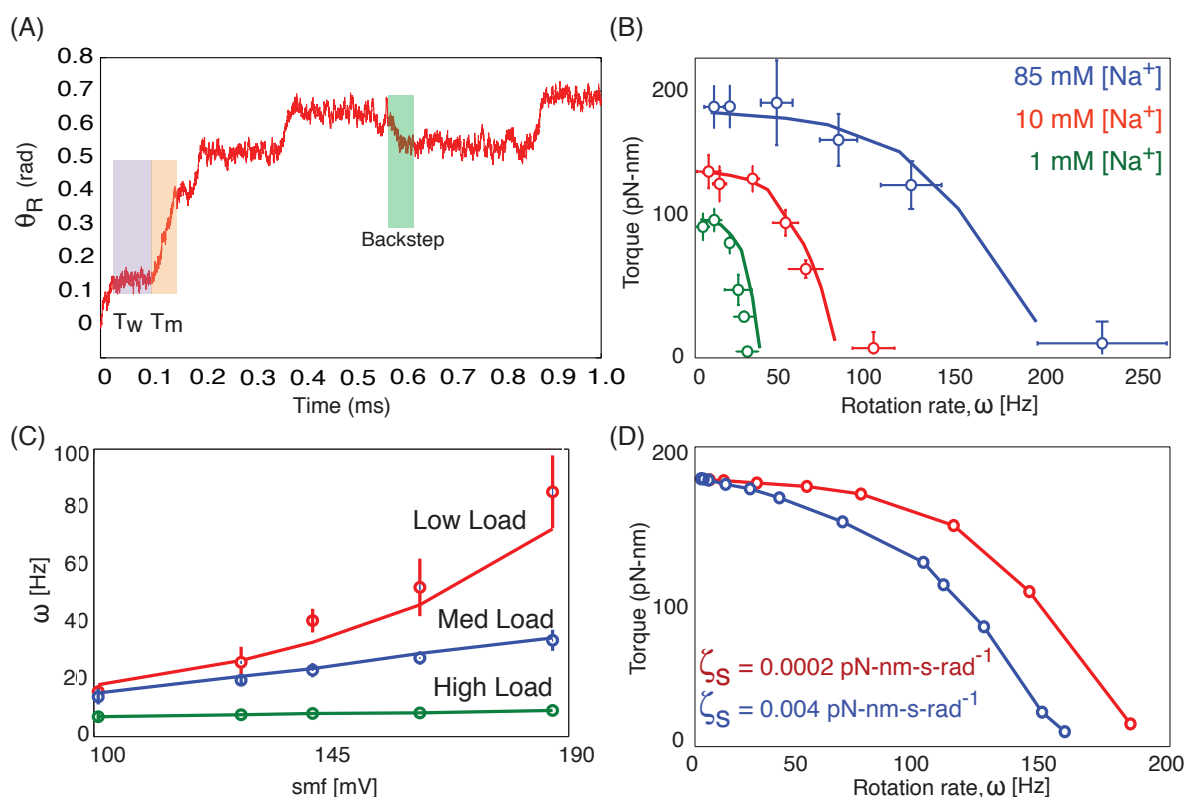
Figure 3.8: Summary of recent experiments and comparisons with model simulations. Results are derived from numerical simulations. In all plots, model calculations are shown by solid lines, and experimental data is shown as open colored circles. **(A)** Sample trajectory generated by the model. Moving (T_M) and waiting (T_W) times are shown with orange and purple backgrounds, respectively. Two "half-steps" separated by a very short pause can be seen in the highlighted forward step (orange). Occasionally, reversals (shown with green background) appear when MotA Loops 2 and 4 are engaged due to conformational changes in FliG. **(B)** Single-stator torque-speed curves measured in a chimeric sodium motor for various sodium concentrations at pH 7.0. Curves show a concave shape, with the length of their "plateau" being SMF-dependent (data from Lo et al. [72]). **(C)** Motor speed vs. SMF in a chimeric sodium motor shows a nearly linear relationship across various loads (data from Lo et al. [72]). **(D)** Effect of stator viscosity on the shape of BFM torque-speed curves. The reduction in the plateau region is mainly due to the nature of the steric forces during the power stroke.

In our model, when the FliGs are oriented at an angle of roughly 10-20° with respect to the radial direction, as shown in Figure 3.1A, the motor moves in the CW direction by virtue of contact forces from loops 2 and 4. Conversely, when the FliGs are pointed either orthogonal or at an angle of 180° with respect to the CW orientation, the motor steps in the CCW direction using loops 1 and 3. The numerical values for the above parameters will likely change with the resolution of a structure. However, the above calculation is meant to demonstrate the general framework of our predicted mechanism, which is independent of these choices. Using an Ising model for the flipping of FliGs, we calculate the probability of a backstep to be $\sim 8\%$. This probability was calculated to be $\sim 7.3\%$ from stepping statistics collected by Sowa et al. [114], demonstrating that a backstep might indeed be simply due to fluctuations in FliG orientation.

The existence of motor backsteps in the absence of CheY-P has been largely attributed to "microscopic reversibility". Given this constraint, there are three possibilities in explaining the backstep: (i) A backward transit of an ion from the cytoplasm to the periplasm. (ii) A sufficiently strained hook relaxes by moving the rotor backwards. (iii) A fluctuation which changes the orientation of FliG from its CCW to CW orientation.

The first two possibilities contradict our proposed model. For example, if the first case were to be correct, then a backstep would correspond to a reversal of the entire conformational change process. In this case, an ion bound to the Asp32 from the cytoplasm should restore the MotA helix from its bent state to the straight state in the presence of the ion. This is in direct contradiction with one of our model assumptions that MotA relaxes to the bent state due to the rearrangement in the hydrogen bonds caused by the binding of the ion to the Asp32 residue.

The second possibility (that the relaxation of an elastically strained hook due to several sequential forward steps leads to an occasional backstep) is also not feasible within the context of our model: a contact force guarantees that the hook always follows the rotor.

In this work, we attribute the molecular basis for the backstep to the third possible scenario: a conformational change in one (or more) individual FliGs on the periphery of the rotor. A FliG can exist in two states; in our model, these states correspond to two orientations of the FliG dipole vector. Our electro-steric model, in conjunction with an Ising model corresponding to the states of FliG, explains the existence of occasional backsteps in a self-consistent manner.

Briefly, a backstep results from a fluctuation of FliG from the CCW to the CW position. In this case, when the motor is predominantly moving in the CCW direction and whenever a FliG changes its state from CCW state to CW state and is close to a stator, then the stator—using MotA loops 2 and 4—applies the contact force and pushes the FliG in the backward direction.

While the configuration of the FliGs in the CW orientation is fairly well agreed upon, the exact CCW configuration is still under debate. At least three possible orientations have been suggested, including directions orthogonal or 180° with respect to the CW orientation. Despite this uncertainty, it is generally believed that there are two significantly different orientations for each FliG.

As in other models, we describe the transitions between the two FliG orientations by a one-dimensional periodic Ising model consisting of 26 spins (corresponding to 26 FliGs). Each individual spin s_i can exist in two possible states corresponding to the two orientations of FliGs: $s_i = +1$ (CCW) and $s_i = -1$ (CW). The Hamiltonian is

$$H = -J \sum_{i,j=1}^{N=26} s_i s_j - h \sum_{i=1}^{N=26} s_i \tag{3.21}$$

where J denotes the nearest neighbor pairwise interaction energy and h denotes the field biasing the FliGs to preferentially orient in a certain direction. Let $\{s_i\} = (s_1, s_2, s_3, \ldots, s_{26})$ denote a possible state of the rotor. The probability of such a state is given by the Boltzmann distribution $\dfrac{e^{-\beta H(\{s_i\})}}{Z(J,h,\beta)}$, where $Z(J,h,\beta)$ is the partition function. The partition function for a one-dimensional Ising model (3.21) is obtained exactly using the transfer-matrix approach, and is given by

$$Z(J,h,\beta) = \lambda_+^N + \lambda_-^N \tag{3.22}$$

where

$$\lambda_\pm = e^{\beta J} \cosh(\beta h) \pm \sqrt{e^{2\beta J} \sinh^2(\beta h) + e^{-2\beta J}} \ . \tag{3.23}$$

In order to understand the back steps while the motor is running predominantly in CCW direction, we calculate the probability that any FliG (or any spin) points in the CW direction. This is given by

$$p(s_i = -1) = \sum_{(s_1, \ldots, s_{i-1}, -1, s_{i+1}, \ldots, s_{26})} \frac{e^{-\beta H((s_1, \ldots, s_{i-1}, -1, s_{i+1}, \ldots, s_{26}))}}{Z} \tag{3.24}$$

where the summation is over all possible states fixing $s_i = -1$. In the following, we derive an analytical expression for the probability $p(s_i = -1)$.

Let us denote the probability for the spin $s_i = +1$ as $p(s_i = +1)$. Given the probabilities $p(s_i = +1)$ and $p(s_i = -1)$, the average value $\langle s_i \rangle$ of the spin s_i can be calculated as

$$\langle s_i \rangle = (1)p(s_i = +1) + (-1)p(s_i = -1) = 1 - 2p(s_i = -1). \tag{3.25}$$

Moreover, the derivative of the partition function Z with respect to the field h yields

$$\frac{1}{N\beta Z} \frac{\partial Z}{\partial h} = \frac{1}{N} \sum_{\{s_i\}} \sum_i s_i \frac{e^{-\beta H(\{s_i\})}}{Z} = \langle s_i \rangle \ . \tag{3.26}$$

Therefore, using (3.25) and (3.26), the probability that spin $s_i = -1$ can be obtained as

$$p(s_i = -1) = \frac{1 - \frac{1}{N\beta Z}\frac{\partial Z}{\partial h}}{2} \ . \tag{3.27}$$

The derivative of the partition function with respect to the field h can be evaluated using the derivatives of the $\lambda_\pm$ functions, which are given by

$$\frac{\partial \lambda_\pm}{\partial h} = \beta \sinh(\beta h) \left(e^{\beta J} \pm \frac{e^{2\beta J} \cosh(\beta h)}{\sqrt{e^{2\beta J} \sinh^2(\beta h) + e^{-2\beta J}}} \right). \tag{3.28}$$

Within the context of our model, the likelihood of a flip in FliG conformation corresponds directly to the likelihood of a backstep. That is, the probability that a FliG is in the CW state is given by (3.27). This is because the fundamental mechanics of a backstep is the same as that of a forward step; the difference between these two scenarios is wholly described by the difference in FliG configuration.

Suppose that the motor is moving primarily in the CCW direction. This means that the FliGs in close proximity to the stator loops are oriented to favor CCW rotation (that is, to favor interaction with MotA loops 1 and 3). However, if a FliG close to the stator is oriented to favor CW rotation, then the FliG interacts with MotA loops 2 and 4, resulting in a step in the CW direction (a "backstep" when the motor is moving primarily CCW). This probability is given by (3.27).

For the choice of the energy scale $\beta J = 2$ at room temperature and a biasing field of $\beta h = 0.05$, the probability that any FliG is in the CW state is $p(s_i = -1) = 0.08$. That is, on average, 8 out of every 100 torque-generating cycles will result in a backstep. Areas under the curve corresponding to forward and backward steps from data collected by Sowa $et~al.$ [114] indicate that $p(s_i = -1) \approx 0.073$ (Figure 3.9).

The above analysis provides an explanation for how backsteps in the absence of CheY-P can arise from fluctuations in FliG configurations. However, it does not take into account how the above probabilities are effected by load or PMF. For example, the timescale of a single step depends on the load. If one assumes that this step is a backstep, then this particular FliG is pinned in the "backwards" orientation for the duration of that step. This CW defect in the FliG ring can affect the switching probabilities of the neighboring FliGs, resulting in further defects along the ring. Therefore, at higher loads, the probability of two (or more) subsequent backsteps may not be negligible. However, a complete understanding of the above requires a far more detailed analysis of an Ising model in conjunction with the proposed electrosteric model than is within the scope of this work.

High stator drag reduces the torque-speed plateau region. Since our mechanism crucially depends on steric forces, we expect the drag coefficient of the stator to have a significant effect on motor behavior. Because we explicitly model the motion of the stator, we are able to study directly the effect of this parameter on the BFM's torque-speed curve. Our model predicts that increasing the stator drag truncates the torque-speed plateau, thus reducing the concave shape of the BFM torque-speed curve (Figure 3.8D).

This is a direct consequence of the steric forces: some portion of the stator-generated force must go towards moving the stator itself. As the drag of the stator increases, so does
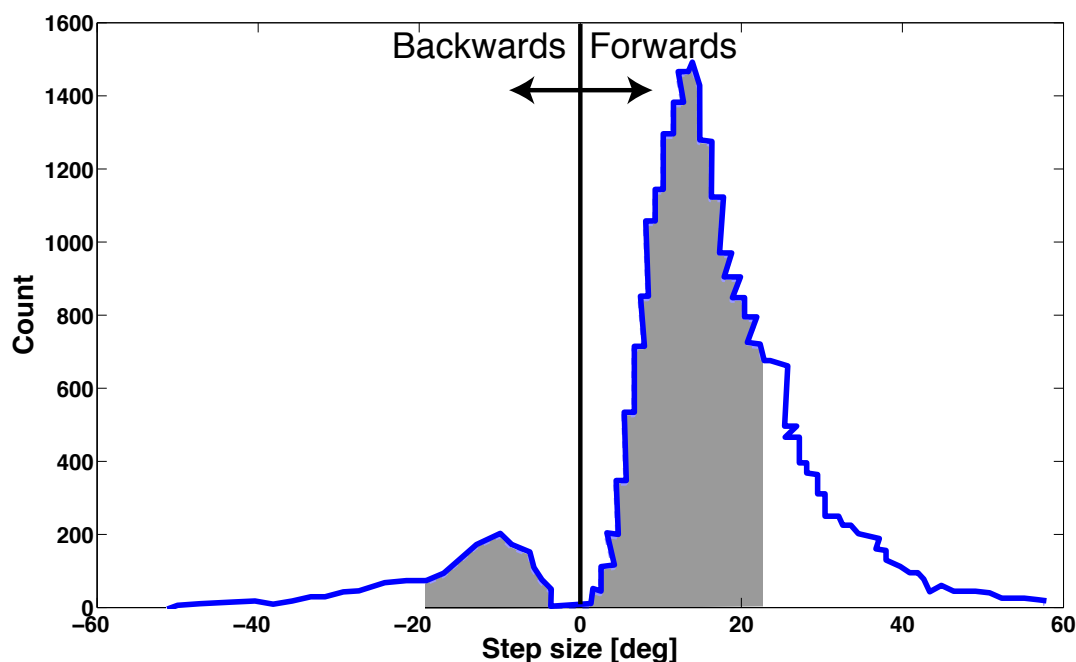
Figure 3.9: Probabilities of backward steps relative to forward steps can be estimated using statistics from stepping experiments (data shown from [114]). The area under the curve for steps below and above 0° corresponds to forward and backward step probabilities, respectively. The areas on either side are calculated as highlighted in gray. Curves are truncated where each shows a second "peak", corresponding to two steps being blurred together due to limitations in experimental resolution. The relative areas calculated for the data above suggest that the probability of a backwards step is 7.3%.

the amount of its generated force allocated to this task. Then for a given load, the torque transferred to the rotor is relatively low for large stator drag coefficients. This reduces the constant-torque plateau, as well as the overall concave shape of the torque-speed curve. This simple prediction may be experimentally tested by increasing the viscosity of the stator's membrane environment.

3.3   In conclusion

The ability to convert a transmembrane ion gradient into rotary torque is rare, observed so far in only two protein motors: the F_O motor of ATP synthase and the BFM. The mechanism behind the torque generation in the latter has been a longstanding mystery, driven by the fundamental role of this machine in bacterial locomotion and chemotaxis.

Here we have combined known structural information on the BFM [58, 66], as well as the experimental measurements on single-stator motors by Lo et al. [72], to construct and test

the first mechanically specific model of torque generation. Using this information, we are able to present an explicit model of the dynamics of the stator during a torque-generation cycle. Our model implicates a steric interaction between the cytoplasmic MotA stator loops and the FliG proteins of the rotor. We have tested the feasibility that this interaction is driven by conformational changes in the MotA loops due to the binding of cations to essential aspartate residues on the two MotBs, as was proposed by Blair and co-workers [58]. Results from our model simulations reproduce recently measured torque-speed and speed-IMF curves from single stator motors. A directly-testable prediction of our mechanism is that increasing the stator drag coefficient (e.g., via increasing the membrane viscosity) will reduce the constant-torque plateau and make the torque speed curve less concave.

The mechanism we have proposed is akin to a two-cylinder engine, where two of the four MotA loops act when the motor is moving in the counterclockwise direction and the other two loops act in the clockwise direction. We have proposed that the two loops act "in-phase" with each other, moving in synchrony as two protons bind to the MotBs and are subsequently released into the cytoplasm. In this manner, the first loop executes its half of the power stroke when the protons bind to the MotBs, and the second loop drives the second half power stroke once the protons have "hopped off" into the cytoplasm.

Experiments performed at low IMF can be used to differentiate between a stator acting as an engine which is "in-phase" or "out-of-phase". Because ion-binding is rate limiting under these conditions, trajectories would show clear half-steps only if the BFM acts as an "out-of-phase" engine. However, given that the mechanics of the power stroke for both scenarios are equivalent, the corresponding out-of-phase mechanism would lead to a calculation analogous to the one presented in this work.

Recently measured torque-speed curves revealed that the number of torque-generating units in the flagellar motor increases with load [68]. This opens several fundamental questions regarding the physics of this molecular machine. A fuller treatment of motors with multiple stators requires a model of stator recruitment—a compelling topic for future work.

Finally, viewing our model in a larger context: if it turns out that the proline hinge motif is not the stator structure driving rotation, but another structural motif, then essentially the same equations would have to be solved, albeit using a different set of collective coordinates.

Chapter 4

The Big Friendly Motor: multi-stator dynamics

"This [dissertation] is continuing very nice. It has a very dory-hunky ending."
            —Roald Dahl, *The BFG*

In the previous chapter, we presented a model in flagellar motors with a single stator, in which a **steric interaction** driven by a **conformational change** in the stator is implicated as the motor's torque-generating mechanism [76]. Our theoretical study was particularly timely as it was able to capitalize on experimental results on single-stator motors [72] to thoroughly explore the fundamental rotor-stator interaction without confounding effects that may arise in multi-stator motors. However, in the "wild", motors have more than one stator, and so in this chapter, we extend this model to consider the behavior of motors with multiple docked stators.

As in the preceding chapter, our exploration begins with arguably the most important physical probe into the dynamics of a molecular motor, its torque-speed relationship. For the BFM, this curve was shown to have two distinct regimes, separated by a "knee" (Figure 4.1). This characteristic feature of the BFM was long held as the first "checkpoint" for any theoretical model of the motor.

However, recent experiments showed that the number of torque-generating complexes (**stators**) in the motor is load-dependent—that is, published torque-speed curves most likely contain measurements from motors with different numbers of docked stators [68, 117]. Specifically, at high loads (low speeds) a motor can have up to 11 docked stators, while at low loads (high speeds) motors typically operate with only one stator (though we note that the experiments in [68] reported that $\sim 25\%$ of motors likely had two stators).

The recent experimental findings [68, 117] shed doubt on several fundamental results about the dynamics of the BFM. In this chapter, while we primarily focus on the behavior of the motor in the "low load" regime, we will also comment on implications of our model in the "high load" regime as well.

Before continuing, we first clarify some of our terminology. We consider the **"low load" regime** (also referred to as **"high speed"**, **"maximum speed"**, **"kinetically limited"**, or **"zero torque"** throughout) to be when the drag coefficient of the load is on the same order of magnitude or lower than the internal friction (i.e., the drag of the rotor). Importantly,
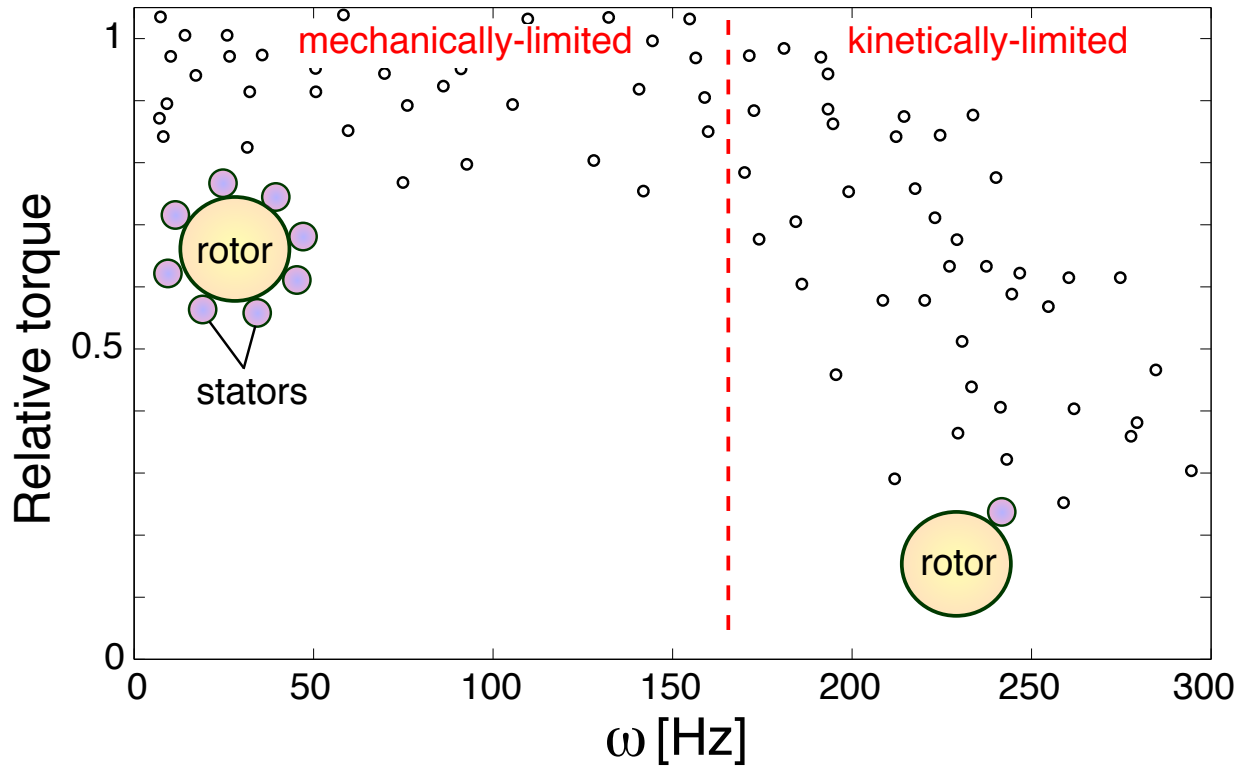
Figure 4.1: Recent experiments have shown that the number of torque-generating complexes (stators) is not constant across applied loads. Therefore, it is likely that most measured torque-speed curves were generated using motors with varying numbers of stators: points in the high-load regime correspond to motors with up to 11 stators and points at low loads (within the kinetically-limited regime) to motors with only one. A red dashed line separates the mechanically-limited and kinetically-limited regimes; we focus on the latter. Data shown is from [29]; however, we note that another experiment in this same article presents data that seems to be collected from a motor with a constant number of stators.

we point out that due to experimental constraints, several results originally considered to be "low load" measurements were conducted using loads outside of this regime; these will be noted as they appear.

In the following, we first provide, for expository purposes, an analytic treatment of a simplified deterministic model that assumes stators step all together in synchrony. This assumption matches the resurrection experiments as they are currently interpreted: primarily, that the addition of stators at low loads has no impact on the motor speed. This section is included to show how the fundamental torque-generation model in the previous section can be adapted to fit this result.

In the section following that one, however, we work under a more realistic assumption: that stators are independently activated. This leads to a non-universal "limiting speed" to

the motor, in opposition to current published assumptions: having more stators, at both high and low loads, increases the motor speed. We constantly refer to experiments to show that this interpretation of our model is consistent with results at both low and high loads.

4.1   Synchronously-stepping stators: a deterministic model

By taking an average over many trajectories, it is possible to generate a deterministic analogue of the model presented above. Although numerical simulations on the full stochastic model were used for the main results in this thesis, the below formulation is convenient primarily for expository purposes. In particular, it admits explicit analytic solutions for many experimental situations. Before we provide the numerical implementation of the full Langevin equations (3.10)-(3.12), we use the following model to introduce several important concepts.

The deterministic equations of motion can be obtained by time averaging the equations (3.10)-(3.12) as

$$\zeta_S \frac{d\phi_S}{dt} = F_p\ell_p - \frac{\langle\tau\rangle}{R}\ell_p \tag{4.1}$$

$$\zeta_R \frac{d\theta_R}{dt} = \langle\tau\rangle - \kappa(\theta_R - \theta_L) \tag{4.2}$$

$$\zeta_L \frac{d\theta_L}{dt} = \kappa(\theta_R - \theta_L). \tag{4.3}$$

Note that in addition to time averaging, we have neglected the electrostatic term for computational convenience, as it tends to be quite small in value. Here, the average torque on the rotor $\langle\tau\rangle$ results from averaging the torque on the rotor as $\tau_{\text{contact}} = -\frac{\partial V_{RS}}{\partial\theta_R}$ over many trajectories. The return force then can be calculated by $\langle\tau\rangle/R$, where R is the radius of the rotor. This is then multiplied by ℓ_p to calculate the return torque. The internal torque of the proline hinge for a given ion motive force (IMF) is $F_p\ell_p = -\dfrac{\partial G}{\partial\phi_S} \propto$ IMF. The averaged equations do not contain a noise term because the terms $f(t)$ are Gaussian with mean zero. In the following, we compute expressions for the average torque and speed during a single power stroke of the motor from the above deterministic model.

Under the assumption that all active stators act in synchrony, Equation (4.1) can be generalized to a motor with N stators as follows. An analogue of Equation (4.1) now corresponds to the motion of the i-th stator ($i \in 1, 2, \ldots N$):

$$\zeta_S \frac{d\phi_S^i}{dt} = F_p\ell_p - \frac{\langle\tau_i\rangle}{R}\ell_p, \quad i \in 1, 2, \ldots, N. \tag{4.4}$$

We can then sum the equations of all stators, which results in

$$\sum_i \zeta_S \frac{d\phi_S^i}{dt} = N\zeta_S \frac{d\phi_S}{dt} = NF_p\ell_p - \frac{\langle\tau\rangle}{R}\ell_p. \tag{4.5}$$

Note that we have used the fact that $\sum_i \langle \tau_i \rangle = \langle \tau \rangle$. Similarly, an equation for the rotor in a motor with multiple stators can be written as:

$$\zeta_R \frac{d\theta_R}{dt} = \sum_{i=1}^{N} \langle \tau_i \rangle - \kappa(\theta_R - \theta_L) \tag{4.6}$$

$$= \langle \tau \rangle - \kappa(\theta_R - \theta_L),$$

which is the same form as Equation (4.2). Note that only the terms corresponding to the stators are summed (i.e., the connection term between the rotor and the load is not multiplied by N). Equation (4.3) also remains as for the single stator case because the spring connection term is unaffected by the addition of torque-generating units.

The three equations of motion (4.1)-(4.3) contain 4 unknowns $\{\theta_R, \theta_L, \phi_S, \langle \tau \rangle\}$. This results in an indeterminate system, and requires the addition of an equation to generate a unique solution. This additional equation can be obtained from a fundamental property of contact forces. Since the stator loop is in contact with the rotor during the power stroke, the velocities of the stator loop and the rotor must be equal. This leads to a **contact condition** for the tangential velocities of the stator loop and the rotor:

$$\boxed{\ell_p \frac{d\phi_S}{dt} = R \frac{d\theta_R}{dt}.} \tag{4.7}$$

Analysis. Multiplying Equation (4.5) by $\frac{R}{\ell_p}$ and summing with (4.2) gives:

$$\frac{NR\zeta_S}{\ell_p} \frac{d\phi_S}{dt} + \zeta_R \frac{d\theta_R}{dt} = NF_pR - \kappa(\theta_R - \theta_L). \tag{4.8}$$

Rearranging (4.7), we get

$$\frac{d\phi_S}{dt} = \frac{R}{\ell_p} \frac{d\theta_R}{dt}. \tag{4.9}$$

Substituting into equation (4.8):

$$\frac{NR^2\zeta_S}{\ell_p^2} \frac{d\theta_R}{dt} + \zeta_R \frac{d\theta_R}{dt} = NF_pR - \kappa(\theta_R - \theta_L)$$

Rearranging, we arrive at:

$$\zeta_R \frac{d\theta_R}{dt}(NM + 1) = NF_pR - \kappa(\theta_R - \theta_L), \tag{4.10}$$

where $M = \frac{R^2\zeta_S}{\ell_p^2\zeta_R}$. Solving (4.10) for $\frac{d\theta_R}{dt}$ gives us:

$$\frac{d\theta_R}{dt} = \frac{NF_pR}{\zeta_R(NM + 1)} - \frac{\kappa}{\zeta_R(NM + 1)}(\theta_R - \theta_L). \tag{4.11}$$

Dividing equation (4.3) by ζ_L and subtracting (4.11) leads to

$$\frac{d(\theta_R - \theta_L)}{dt} = \frac{F_p R}{\zeta_R(NM+1)} - \kappa\left(\frac{1}{\zeta_R(NM+1)} + \frac{1}{\zeta_L}\right)(\theta_R - \theta_L). \tag{4.12}$$

This differential equation has the solution:

$$\boxed{(\theta_R - \theta_L)(t) = \frac{A^*(1 - e^{-\alpha^* t})}{\alpha^*},} \tag{4.13}$$

where $A^* := \frac{F_p R}{\zeta_R(NM+1)}$ and $\alpha^* := \kappa\left(\frac{1}{\zeta_R(NM+1)} + \frac{1}{\zeta_L}\right)$.

Substituting expressions for $\dfrac{d\phi_S}{dt}$ and $\dfrac{d\theta_R}{dt}$ from Equations (4.5) and (4.2), respectively, into the equation for contact condition (4.7) leads to:

$$\frac{\ell_p^2}{N\zeta_S}(NF_pR - \tau) = \frac{R^2}{\zeta_R}[\tau - \kappa(\theta_R - \theta_L)]. \tag{4.14}$$

Note that, because we are interested in the full time course, we consider $\tau = \tau(t)$, rather than the average torque $\langle\tau\rangle$. Rearranging and solving for τ:

$$\tau = \frac{N\zeta_R R\left[F_p\ell_p^2 - \zeta_S R\kappa(\theta_R - \theta_L)\right]}{\zeta_R\ell_p^2 + N\zeta_S R^2}. \tag{4.15}$$

Plugging in the derived expression for $(\theta_R - \theta_L)$ from Equation (4.13):

$$\tau = \frac{F_p\ell_p^2 NR\zeta_R\zeta_S\left[\frac{1}{\zeta_S} + \frac{\left(1 - \exp\left[\kappa t\left(\frac{1}{\zeta_L} + \frac{1}{\zeta_R + NR^2\zeta_S/\ell_p^2}\right)\right]\right)NR^2\zeta_S}{\zeta_R\left(\ell_p^2(\zeta_L + \zeta_R) + NR^2\zeta_S\right)}\right]}{\ell_p^2\zeta_R + NR^2\zeta_S}. \tag{4.16}$$

From this value, we can calculate the average torque in a single step $\langle\tau\rangle$ by

$$\langle\tau\rangle = \frac{1}{T_m}\int_0^{T_m}\tau(t)dt$$

$$= \frac{F_p\ell_p^2 NR\left(\left(-1 + \exp\left[\kappa T_m\left(-\frac{1}{\zeta_L} - \frac{1}{\zeta_R + NR^2\zeta_S/\ell_p^2}\right)\right]\right)NR^2\zeta_L^2\zeta_S + \kappa T_m(\zeta_L + \zeta_R)\left(\ell_p^2(\zeta_L + \zeta_R) + NR^2\zeta_S\right)\right)}{\kappa T_m\left(\ell_p^2(\zeta_L + \zeta_R) + NR^2\zeta_S\right)^2} \tag{4.17}$$

where T_m is the time spent moving during a step. Likewise, we can also calculate the speed of the load $\dfrac{d\theta_L}{dt}$ from Equations (4.3) and (4.13):

$$\frac{d\theta_L}{dt} = \frac{1}{\zeta_L}\kappa(\theta_R - \theta_L)$$

$$= \frac{\left(1 - \exp\left[-\kappa t\left(\frac{1}{\zeta_L} + \frac{1}{\zeta_R + NR^2\zeta_S/\ell_p^2}\right)\right]\right)F_p\ell_p^2 NR}{\ell_p^2(\zeta_L + \zeta_R) + NR^2\zeta_S}. \tag{4.18}$$

As with torque, we integrate over a time step to find the average speed $\left\langle \dfrac{d\theta_L}{dt} \right\rangle$:

$$\left\langle \frac{d\theta_L}{dt} \right\rangle = \frac{F_p \ell_p^2 N R \left[\left(-1 + \exp\left[\kappa T_m \left(-\frac{1}{\zeta_L} - \frac{1}{\zeta_R + N R^2 \zeta_S / \ell_p^2} \right) \right] \right) \zeta_L \left(\ell_p^2 \zeta_R + N R^2 \zeta_S \right) + \kappa T_m \left(L^2 (\zeta_L + \zeta_R) + N R^2 \zeta_S \right) \right]}{\kappa T_m \left(\ell_p^2 (\zeta_L + \zeta_R) + N R^2 \zeta_S \right)^2}.$$

(4.19)

Using Equations (4.17) and (4.19), we can calculate a family of parametric torque-speed curves (parametrized by the load ζ_L), where each curve corresponds to a motor with a constant number of synchronously stepping stators.

Approximation: model without spring. In most experimental setups, the filament is removed and a bead is attached to a shortened hook connection. Additionally, the hook is sometimes stiffened with an antibody linker. These setups have a rigid connection between the rotor and the load, corresponding to a large spring constant. In this section, we perform a similar analysis to that in the previous section for the limit $\kappa \to \infty$. The calculations performed in this section provide analytic formulas for a clear physical understanding of several important properties of the model.

The rotation rates of the rotor and load become equal after an initial "wind-up" period. That is, the rotor and load move at the same angular speed $\left(\text{i.e., } \dfrac{d\theta_R}{dt} = \dfrac{d\theta_L}{dt} \right)$ after the system reaches a steady state. Note however that the angular positions θ_R and θ_L still maintain a (constant) offset. This can be seen explicitly by subtracting Equations (4.2) and (4.3):

$$\frac{d(\theta_R - \theta_L)}{dt} = \frac{\langle \tau \rangle}{\zeta_R} - \kappa \left(\frac{1}{\zeta_R} + \frac{1}{\zeta_L} \right) (\theta_R - \theta_L).$$

(4.20)

To simplify some notation, we define $x := (\theta_R - \theta_L)$, $\alpha := \kappa \left(\frac{1}{\zeta_R} + \frac{1}{\zeta_L} \right)$ and $A := \frac{\langle \tau \rangle}{\zeta_R}$, and rewrite Equation (4.20)

$$\frac{dx}{dt} = A - \alpha x.$$

(4.21)

As in the previous section, we can solve for the timecourse $x(t) = (\theta_R - \theta_L)(t)$:

$$x(t) = (\theta_R - \theta_L)(t) = \frac{A(1 - e^{-\alpha t})}{\alpha}.$$

(4.22)

By definition, $\alpha > 0$, and so $x(t)$ converges exponentially fast. As $\kappa \to \infty$, the characteristic "wind-up" time $1/\alpha$ goes to zero. In this limit, we can consider the load to be rigidly connected to the rotor, and so there is no "delay" in its following; i.e., $\frac{d\theta_R}{dt} = \frac{d\theta_L}{dt}$.

Summing Equations (4.2) and (4.3) gives us:

$$\zeta_R \frac{d\theta_R}{dt} + \zeta_L \frac{d\theta_L}{dt} = \langle \tau \rangle.$$

(4.23)

When κ is large, $\frac{d\theta_R}{dt} = \frac{d\theta_L}{dt}$ and Equation (4.23) reduces to:

$$(\zeta_R + \zeta_L)\frac{d\theta_R}{dt} = \langle \tau \rangle. \tag{4.24}$$

We multiply Equations (4.5) and (4.24) by ℓ_p and R, respectively. After some algebra:

$$\ell_p \frac{d\phi_S}{dt} = \frac{\ell_p^2}{N\zeta_S}\left(NF_p - \frac{\langle \tau \rangle}{R}\right) \tag{4.25}$$

$$R\frac{d\theta_R}{dt} = \frac{R\langle \tau \rangle}{(\zeta_L + \zeta_R)}. \tag{4.26}$$

Given the relationship (4.7), the two right hand sides of (4.25) and (4.26) are equal:

$$\frac{\ell_p^2}{N\zeta_S}\left(NF_p - \frac{\langle \tau \rangle}{R}\right) = \frac{R\langle \tau \rangle}{(\zeta_L + \zeta_R)} \tag{4.27}$$

Multiplying by NR:

$$\frac{\ell_p^2 R}{\zeta_S}\left(NF_pR - \langle \tau \rangle\right) = \frac{NR^2\langle \tau \rangle}{(\zeta_L + \zeta_R)}. \tag{4.28}$$

Solving for $\langle \tau \rangle$:

$$\boxed{\langle \tau \rangle = \frac{NF_pR}{\left(1 + \frac{NR^2\zeta_S}{(\zeta_L+\zeta_R)\ell_p^2}\right)}.} \tag{4.29}$$

We can use this expression for some intuition about the result of Sowa et al. [114] regarding torque and stator number at high and low loads. Consider the following two limits of Equation (4.29): (i) high load, when $\zeta_L \gg \zeta_R$, and (ii) low load, where $\zeta_L \ll \zeta_R$.

In the first case, we have:

$$\begin{aligned}
\langle \tau \rangle_{\text{high}} &= \frac{NF_pR}{\left(1 + \frac{NR^2\zeta_S}{(\zeta_L+\zeta_R)\ell_p^2}\right)} \\
&\approx \frac{NF_pR}{\left(1 + \frac{NR^2\zeta_S}{\zeta_L\ell_p^2}\right)} \\
&\approx NF_pR. \tag{4.30}
\end{aligned}$$

The third line follows from the fact that $\zeta_S < \zeta_R \ll \zeta_L$. For very high loads, the observed torque is 180 pN-nm, and therefore the force $F_p \approx 9.5$ pN. Equation (4.30) suggests that the torque increases linearly with stator number under extremely large loads as observed in the experiments. However, for a given ζ_L, it can be seen that nonlinearities can arise in the torque versus number of stators even in the high load limit. This property is primarily due to the nature of contact forces, and is not applicable to previous models which assume constant torque between stator and rotor.

Conversely, at low loads ($\zeta_L/\zeta_R \ll 1$):

$$
\begin{aligned}
\langle\tau\rangle_{\text{low}} &= \frac{NF_pR}{\left(1 + \frac{NR^2\zeta_S}{(\zeta_L+\zeta_R)\ell_p^2}\right)} \\
&\approx \frac{NF_pR}{\left(1 + \frac{NR^2\zeta_S}{\zeta_R\ell_p^2}\right)}.
\end{aligned}
\tag{4.31}
$$

The torque measured at high speeds is approximately 20 pN-nm [72]. Then, from Equation (4.31), the non-dimensional number $NR^2\zeta_S/\zeta_R\ell_p^2 \approx 10$. Also, Equation (4.31) shows that the torque and speed are not linearly dependent on the number of stators at low loads. This is consistent with previous experimental observations [128].

The above approximations to the full model are primarily laid out for expository purposes, to introduce general properties of the model. The observations from Sowa et al. are under question given that motors with more than one (or a few) stators may not have been considered in low-load measurements. In order to determine whether the stators do indeed act independently or in synchrony, experiments that directly account for the number of active stators must be performed. The extension of our model to N stators is dependent on the assumption that all stators step in synchrony, and the above results will not hold if stators are independent stochastic steppers. The other "extreme" case, in which stators step independently of each other, is discussed at length later in this chapter. Intermediate cases, which must involve both further theoretical and experimental consideration of the interactions between stators in multi-stator motors, are extremely worthwhile, but out of reach given our current body of knowledge.

Addition of chemical kinetics. The linear torque-speed curves of a mechanically rate-limiting model elucidate the importance of the inclusion of ion-binding kinetics. In this case, these are events related to the binding of a cation from the periplasm to Asp32 and the unbinding of the cation from Asp32 into the cytoplasm. In this section, we recompute model torque-speed curves, explicitly including the dwell times corresponding to the ion-binding and unbinding events between the power strokes.

As done by Meacci and Tu [80], a torque-generation cycle is divided into two parts: (i) moving time T_m and (ii) waiting time T_w. Assuming that the ions bind only when the stators are around the minimum of the respective free energy potentials, we may use the above model during T_m and sample T_w from an exponential distribution at the end of each moving step.

In a motor with a single stator ($N = 1$), the instantaneous torque is obtained from Equation (4.29) as

$$
\tau = \frac{F_pR}{\left(1 + \frac{R^2\zeta_S}{(\zeta_L+\zeta_R)\ell_p^2}\right)}.
\tag{4.32}
$$

The force applied by the proline hinge is given as $F_p = -\frac{\Delta G}{\Delta \phi} = -\frac{2q \, \text{IMF}}{\Delta \phi}$, where q is the charge of the ion. Under the (fairly egregious) assumption that the motor speed ω is constant, we can compute the moving time $T_m^i = d_i/\omega$, where d_i is the angular distance moved in step i. Because we assume constant step size, $d_i = \frac{2\pi}{26}$ rad for all i. This can then be calculated from Equation (4.32) through the relationship $\omega = \tau/(\zeta_R + \zeta_L)$ as:

$$T_m^i = T_m = \frac{2\pi}{26}(\zeta_R + \zeta_L)\left(1 + \frac{R^2 \zeta_S}{(\zeta_L + \zeta_R)\ell_p^2}\right)\frac{1}{F_p R}. \tag{4.33}$$

Let T_w^i be the waiting time that follows a step i. During the waiting time, the instantaneous torque is zero. When the system reaches the steady state, the average torque $\langle \tau \rangle$ can be obtained via a time average

$$\langle \tau \rangle = \lim_{T \to \infty} \frac{1}{T} \int_0^T \tau(t')dt', \tag{4.34}$$

where T is large. If there are N steps in time T, then there are N waiting times. Therefore, Equation (4.34) can be approximated as

$$\begin{aligned}
\langle \tau \rangle = \lim_{T \to \infty} \frac{1}{T} \int_0^T \tau(t')dt' &\approx \frac{\sum_{i=1}^N \tau_i T_m^i}{T} \\
&= \frac{\sum_{i=1}^N \tau_i T_m^i}{\sum_{i=1}^N T_m^i + \sum_{i=1}^N T_w^i} \\
&= \frac{\tau T_m}{T_m + \frac{1}{N}\sum_{i=1}^N T_w^i}.
\end{aligned} \tag{4.35}$$

The average dwell time $\frac{1}{N}\sum_{i=1}^N T_w^i$ can be approximated as $\langle T_w \rangle = \left(k_0 \exp\left(\frac{\text{IMF}}{k_B T}\right)\right)^{-1}$, where k_0 is a proportionality constant related to the rate of hopping of the ions. Using this, Equation (4.35) reduces to

$$\langle \tau \rangle = \frac{\tau T_m}{T_m + \langle T_w \rangle}. \tag{4.36}$$

Likewise, the speed of the rotor (or the bead in the large spring constant limit) can be written as a time average

$$\langle \frac{d\theta_R}{dt} \rangle \approx \lim_{T \to \infty} \frac{1}{T} \int_0^T \frac{\theta_R(t')}{dt'}dt' = \frac{\frac{2\pi}{26 T_m}T_m}{T_m + \frac{1}{N}\sum_{i=1}^N T_w^i} = \frac{\frac{2\pi}{26 T_m}T_m}{T_m + \langle T_w \rangle} \tag{4.37}$$

where the instantaneous speed is $\frac{2\pi}{26} \times \frac{1}{T_m}$ during the power stroke and zero during the dwell time.

The torque during a power stroke τ, the time taken by a single step T_m, and the dwell time T_w all depend on the IMF. Thus, (4.35) and (4.37) point to the existence of nonlinearity in the torque-speed and speed-pmf curves, presented throughout this thesis and expanded upon in Appendix A.

4.2 Independently-stepping stators

In the following, we first give an overview of our model for single-stator motors and then discuss its extension to motors with multiple docked stators. We then discuss the implication of such a model for motors operating at low load: in particular, challenging the widely-held belief that the motor speed near the zero-torque limit is independent of the number of docked stators.

Our model implicates a steric interaction between the stator and rotor in torque generation [76]. Briefly, stators drive motor rotation by stepping along protein "spokes" around the periphery of the **rotor**, a large ring that connects to the flagellar filament via a flexible hook. This interaction is analogous to parents pushing on the handles of a merry-go-round on the playground for their children's amusement. An overview of our proposed mechanism was given in Figure 3.6.

Recall that individual steps are initiated by proton arrivals at ion-binding sites within the stator complex. The gate-controlled diffusion of protons through the BFM's stator, and its link to motor rotation, was recently explored [92]. During the power stroke, conformational changes in the stator apply a steric force onto the spokes of the rotor wheel, rotating it a discrete step length d. Details on the stator potential curves are provided in the previous chapter.

An important feature of our model is that stators apply no force ($F_p = 0$) to the rotor between power strokes. This results in negligible applied (τ_{contact}) and reaction torque (τ_{reaction}) when the stator and rotor are not in contact with each other. The values of these torques are calculated as the gradients of the interaction potential between the stator and the rotor, as shown in the previous chapter. All other model parameters are described

Table 4.1: Model parameters with units, values, and reference.

| Parameter	Definition	Units	Values	Ref
F_p	Proline hinge force	pN	20	[10]
ℓ_P	Length of proline hinge	nm	7	[133]
ζ_S	Stator drag coefficient	pN-nm-s-rad^{-1}	0.002	fit
ζ_R	Rotor drag coefficient	pN-nm-s-rad^{-1}	0.02	[10]
ζ_L	Load drag coefficient	pN-nm-s-rad^{-1}	0.005–10	[132]
κ	Hook spring constant	pN-nm-rad^{-1}	150	[19]
N	Number of stators	-	1–11	[132]
τ_{contact}	Contact torque on rotor	pN-nm	-	-
τ_{reaction}	Reaction torque on stator	pN-nm	-	-
ϕ_S	Stator angular position	rad	-	-
θ_R	Rotor angular position	rad	-	-
θ_L	Load angular position	rad	-	-
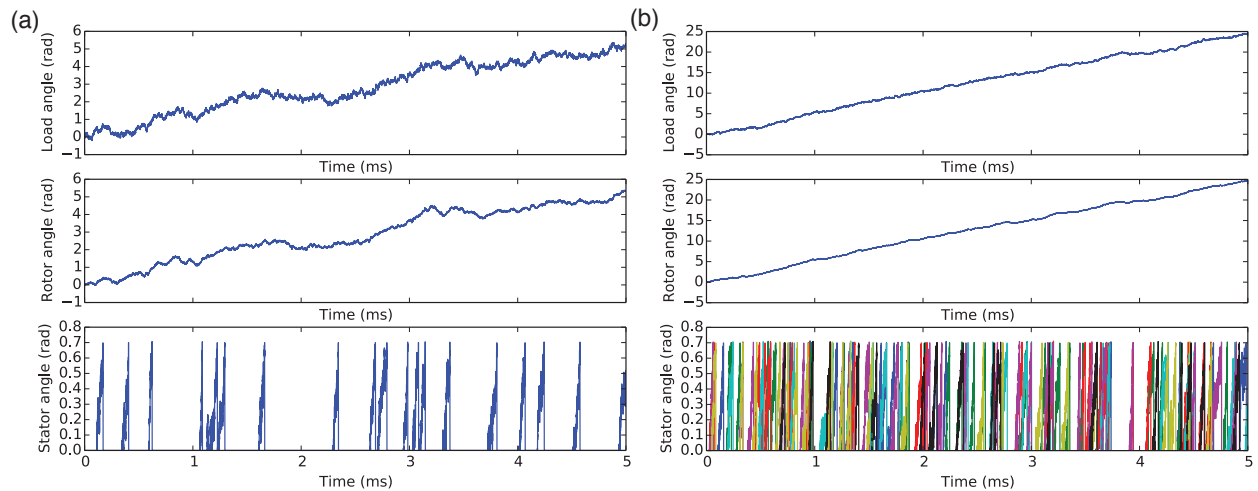
Figure 4.2: Simulation output (5 ms) at $\zeta_L = 0.005$ pN-nm-s-rad^{-1} for motors with **(a)** one and **(b)** seven stators. Top and middle panels show load and rotor trajectories, respectively. Bottom panels show stator stepping events. In **(b)**, events for each stator are colored uniquely.

in Table 4.1. Because the BFM lives at low Reynolds number, the rotor also exhibits no productive movement when the stator is disengaged between steps.

We assumed that there are 26 spokes along the edge of the rotor ([114], although see, e.g., [66, 99]). A "perfect" power stroke is defined as a step of length $d = \frac{2\pi}{26}$ rad, leaving the stator in contact with the neighboring spoke. These steps are observed through the rotation of a small bead (the "load") attached to the flagellar hook.

When the connection between the rotor and the bead is soft (κ is small), discrete motor steps "blur" into a seemingly continuous trajectory. Experimentally, steps have been directly observed by slowing the motor down to a speed of approximately 10 Hz [114].

In a motor with multiple stators, the mechanics of each stator follows the equations corresponding to that of a single stator. At any given time, docked stators can be "engaged" (i.e., actively performing a power stroke) or "disengaged" (in between power strokes). The mechanics of each unit follows the equations presented for a single stator. In multi-stator motors, each stator may act in synchrony with others, or be independently "activated" at rates given by Equations 3.19 and 3.20. Because cation arrivals are Poisson processes (i.e., waiting times between arrivals are distributed exponentially) [9, 75], the "next arrival" in a motor with N stators occurs at a rate $N \times k_{\text{on}}$, where k_{on} is the rate of arrival for a single stator.

This is seen in Figure 4.2, where the space between individual stator stepping events is much smaller in a motor with seven stators (right) than in a single-stator motor (left). The decrease in waiting time between steps in multi-stator motors is also seen in the rotor and

bead trajectories, which are far smoother when steps follow each other more closely.

The total contact torque τ_{contact} that the rotor feels is given by a sum of the contributing contact torques of each stator at a given time:

$$\tau_{\text{contact}} = \sum_{i=1}^{N} \tau_{\text{contact}}^i, \tag{4.38}$$

where τ_{contact}^i corresponds to the contribution of the ith stator and N is the total number of docked stators in the motor. The reaction torque, τ_{reaction} is computed similarly. As is evident from the form of the stator-rotor interaction potential V_{RS}, a stator not in a power stroke (i.e., during T_w) applies no torque to the rotor (i.e., $\tau_{\text{contact}}^i = \tau_{\text{reaction}}^i = 0$).

Let us consider duty ratio as the proportion of time that the torque on the rotor from the stator is nonnegligible. Then, from the above, it is clear that, by the construction of our model, more docked stators increase a motor's duty ratio: a multi-stator motor, with many possibly contributing terms to the sum would naturally have a higher duty ratio than a single stator motor.

An important consideration in simulations with multiple, independently-stepping stators is the following. While each stator pushes on its own "spoke" on the rotor's edge, these spokes are rigidly connected. This means that if one stator begins its power stroke shortly after another stator has done so, it likely will apply no torque to the rotor for some portion of its cycle. This is because the positions of the rotor spokes are dependent on each other, and the power stroke of the first stator will have pushed the second stator's spoke slightly out of reach (at least for the initial part of its cycle).

Technical details. We discuss briefly some technical details regarding practical implementation and simulation of the model equations. Example low-load simulation output can be seen for motors with one and seven stators in Figure 4.2.

Discrete transitions are modeled using Gillespie's method, as follows. For motors with N stators, N "first arrival times" are initially chosen from an exponential distribution at $t = 0$. Each subsequent waiting time is drawn from an exponential distribution when the stator loop reached a small range around the potential minima. For example, the time required to "hop off" is chosen when the angle of the stator loop is within a small range $((20 - \epsilon^\circ), (20 + \epsilon^\circ))$ for some prescribed ϵ. Likewise, the time for the next cation arrival is chosen when the angle retracts to within ϵ of 0°. This is done to imitate the alternating access of the cation-binding site to the periplasm and cytoplasm.

The rate for protons hopping off into the cytoplasm (k_{off}) are chosen as 1000 times the value for proton arrivals k_{on} [5]. This is in line with the fact that half-steps have yet to be directly observed experimentally.

Continuous-time portions of each cycle (corresponding to the mechanical movements) for the stator, rotor, and load are simulated using a forward finite difference scheme with a time step of 10^{-8} s. Checks are put in place to assure that the stator position does not surpass the position of the rotor due to the time step being too large.

Rotor spokes (FliG proteins) are rigidly connected to each other. Therefore, if a stator s_1 initiates its power stroke at time t_1 and a second stator s_2 initiates its power stroke at time $t_2 > t_1$, then the FliG adjacent to s_2 will have moved the same distance as the FliG that s_1 pushed in the interval $[t_1, t_2)$. This means that the portion of the power stroke up until s_2 can "catch up" to the FliG in front of it will be 'wasted' (i.e., no torque will be applied on the rotor by s_2). For simplicity, we do not consider backsteps in our simulations: each stator sees only the FliG in front of it. In time intervals where no stators are pushing on the rotor, stators are repositioned such that each is directly adjacent to a FliG.

All data points were computed as averages from 10 simulation runs, each of length 1 s. Because simulations were performed at low load, this run length was sufficient to include many steps. Standard errors of the mean were smaller than the size of markers.

Low loads

A seminal set of experiments, termed "resurrection" experiments, studied the dependence of motor speed on the number of stators at various external loads [18, 103, 128]. In these experiments, paralyzed cells were allowed to begin rotating slowly, and discrete increases in speed were interpreted as the addition of torque-generating complexes. Surprisingly, while up to 11 increases of near-equal size were observed at high loads, only a single such "jump" was observed at low loads.

These results quickly led to a series of reworked theoretical models, all of which required that the limiting speed of the motor be independent of the number of stators [80, 8, 79]. However, it is likely that low-load measurements were never performed on motors with more than one stator, leaving open the question of how the BFM behaves in the zero-torque (high-speed) limit.

From simulations, we predict that the maximum speed of the motor is dependent on the number of engaged torque generating complexes (Figure 4.3c, open red markers). This result arises from the fact that the stator is not in contact with the rotor in between steps, or **"power strokes"** (i.e., the **duty ratio** of the motor is less than 1). We note that while models with high duty ratios also can reproduce current experiments, evidence of a conformational change in stator structure has been reported (see, e.g., [60]). Generic models involving such a conformation will share this property, because such mechanisms likely require stators to "reset" between steps. In their recent paper, Lo et al. computed torque-speed curves for a chimeric sodium-driven motor [72]. Low-load measurements on these motors were performed using a 100 nm-diameter gold bead (inset, Figure 4.3c).

This data was collected from motors with 1–5 active stators (Figure 4.3c, blue markers). The authors focused on single-stator motor dynamics, leaving open the implications of their data for how the zero-torque speed depends on stator number. The existence of multiple discrete peaks at low load strongly supports the idea that the maximum speed is dependent on the number of stators, at least in chimeric motors. We note that current interpretation of experimental results on the wild-type motor support a zero-torque speed independent of the number of stators. We predict that our model will hold for both Na^+ and H^+ motors;
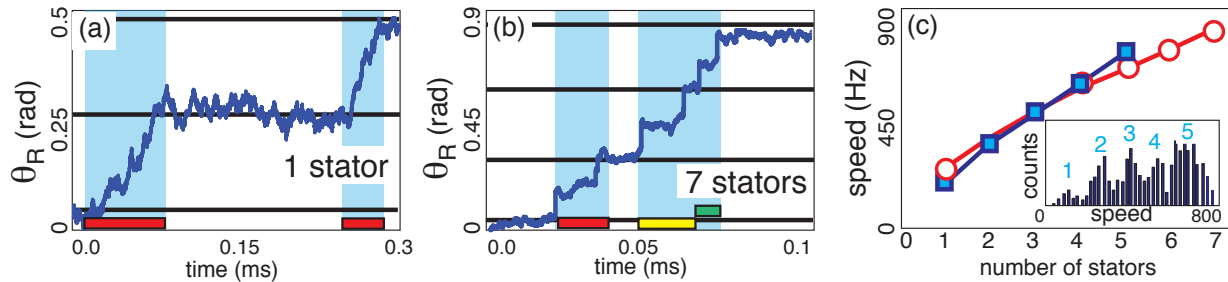
Figure 4.3: Simulated trajectories are shown for motors with **(a)** one and **(b)** seven engaged stators, with $\zeta_L = 0.005$ pN-nm-s-rad^{-1}. Horizontal black lines denote the distance between "perfect" steps ($\ell = \frac{2\pi}{26}$ rad). Colored bars at the bottom of the plots mark the duration of individual stator steps (in the shown trace, steps for three out of the seven engaged stators are shown). In the multi-stator motor trajectory **(b)**, steps for each stator are differently colored. In accordance with published temporal resolutions [93, 61], we consider two steps distinguishable if the end of the first step and the start of the second step are separated by 10 μs. These are shaded in blue; for multi-stator motors, steps may overlap or be too close together to be observed. **(c)** Motor speed at low loads increases with the number of stators. An experimentally-measured speed distribution at low loads is shown in the inset (data from [72]). Gaussian fits to the major peaks give mean speeds (blue squares) in good agreement with simulation predictions (open red circles).

however, further experiments on the wild-type are required for a definitive conclusion to this end.

Ryu and coauthors reported a set of general conditions that must be met in order for the limiting speed to be independent of stator number [105]. First, the rate at which steps are initiated must be independent of the relative position of the rotor and the stator. This position is dependent on both the external load and the actions of any other engaged stators. Therefore, the "decision" of a stator to step should be ignorant of both these factors. Second, stators must engage the rotor for the majority of their cycle (i.e., the BFM's duty ratio DR ≈ 1). Resurrection experiments reporting that the speed at low loads was independent of stator number soon followed [128], which seemed to lend strong support to both of the proposed requirements. We note that, while the experiments in [128] were performed in what we have considered to be near-zero load, the measurements performed in [105] that were referred to as "low load" were actually made at significantly higher loads.

Because we assume that stators are disengaged with (i.e., not applying any directional torque to) the rotor between successive power strokes, our model contains a violation of the second condition. In particular, unlike most proposed mechanisms (but see [21]), we assume motor rotation and ion flow can be *loosely coupled*: an ion passage may not always result in appreciable rotation of the rotor. The *stator's* motion, however, is tightly coupled to ion flow—that is, an ion passage is both necessary and sufficient for the initiation of a stator's
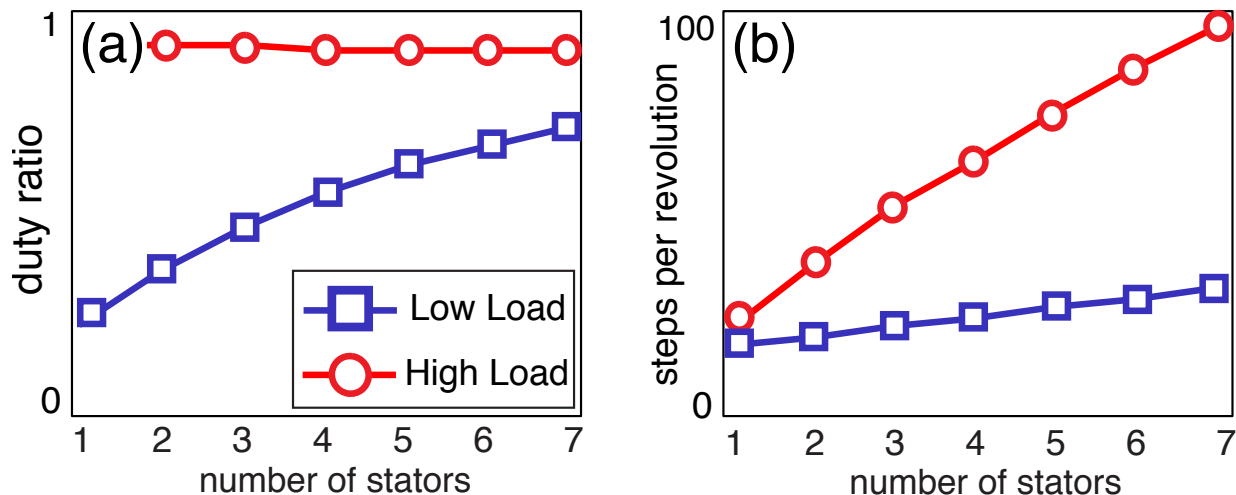
Figure 4.4: Comparison of motor dynamics at low ($\zeta_L = 0.005$ pN-nm-s-rad^{-1}, shown as blue squares) and high ($\zeta_L = 0.5$ pN-nm-s-rad^{-1}, shown as red circles) loads. **(a)** Decrease in the average time between steps with increasing stator number results in an increase in duty ratio in the low-load regime. In contrast, at high loads, each stator step takes a considerable amount of time (T_m is high), and the duty ratio is high even for single-stator motors. **(b)** As stators are recruited to fast-rotating motors (i.e., at low load), the number of independent stator steps per motor revolution (n_{steps}) increases sublinearly from 26 steps/rev for single-stator motors. At high loads, as predicted in [106], the steps per revolution is proportional to the number of stators. Note that n_{steps} is the number of *independent* stepping events, and does not depend on experimental resolution.

power stroke. Therefore, loose coupling in our model does not arise from some form of ion leakage [21, 97, 95, 96, 13], but because stator steps are rarely "perfect" in multiple-stator motors. If steps overlap, a portion of the second stroke is "wasted" because the rotor is pushed out of the later-firing stator's reach.

These properties seem contrary to present assumptions that stators in the BFM must have a high duty ratio. However, we show that our prediction that DR < 1 at low loads arises from fundamental differences in motor dynamics between the high- and low-load regimes. In this way, we argue that our proposed mechanism is compatible with experimental evidence for a high duty ratio at high loads (Figure 4.4a).

A stator initiates a step when protons arrive at a specified binding site within the complex. The mechanochemical cycle of the stator has two phases: moving and waiting, characterized by timescales T_m and T_w, respectively [80]. If T_S is the time that a stator engages the rotor during a complete cycle ($T_m + T_w$), a single-stator motor has duty ratio DR $= T_S/(T_m + T_w)$.

The waiting time between strokes T_w depends on the rate of proton arrivals at a binding site. These arrivals are Poissonian with rate $k_{\text{on}} = k_0 \exp\left[\lambda \Delta G_{\text{ij}}/k_B T\right]$. Here, ΔG_{ij} is the thermodynamic contribution of the ion motive force and $k_B T$ is Boltzmann's constant

multiplied by temperature [123, 8]. For simplicity, we choose $\lambda = 0.5$ as done in previous studies [123]. The parameter k_0 is a function of the pH of the external periplasm; lower pH corresponds to higher proton concentration and thus a speedier arrival at the site. At room temperature and pH 7.0, $\langle T_w \rangle = 1/k_{on} = 0.2$ ms for single-stator motors [80, 79].

The average moving time is estimated through the relation $\omega \approx \ell / (\langle T_m \rangle + \langle T_w \rangle)$ [80]. The average motor speed ω is also related to the load drag coefficient ζ_L by $\zeta_L \omega \approx \tau$, where τ is the motor torque [10, 55]. In our simulations, the motor is limited by proton arrivals at very low loads ($\langle T_m \rangle \approx 0.01$ ms), while at high loads, $\langle T_m \rangle \approx 10$ ms surpasses $\langle T_w \rangle$. These values are consistent with previous studies [80, 79].

Because we predict that motor rotation is driven by steric forces, a stator must be in contact with the rotor for a large part of a productive power stroke ($T_S/T_m \approx 1$). Previous models of torque-generation have similarly considered the mechanochemical cycle of the BFM to consist of moving and waiting phases [80, 79]. However, our model is unique in assuming that stators disengage from the rotor between subsequent power strokes. This results in DR < 1 for single-stator motors at low loads, as the waiting time is no longer negligible compared to the moving time in this regime (Figure 4.4a, blue squares). The waiting time may even surpass $\langle T_m \rangle$, as shown in Figure 4.3a-b.

The waiting time until a proton binds to any one of N independently-stepping stators is exponentially distributed with rate $N \times k_{on}$. Therefore, $\langle T_w \rangle$ is shortened as additional stators are recruited. The subsequent increase in duty ratio (Figure 4.4a, blue squares) results in an increase in limiting speed with the number of stators.

High-loads

Here, we address the assertion that the duty ratio of the BFM must be very high. Two common arguments in the literature are based on (i) the observation that the number of steps per revolution n_{steps} increases as additional torque-generating complexes were recruited [106, 107] and (ii) a calculation determining that a motor with a low duty ratio cannot be processive due to "unwinding" of the tether connection between the rotor and load [10]. The application of these arguments, based on high-load measurements, to the low-load regime has been possible because of the lack of a proposed physical mechanism for BFM rotation. Such a mechanism is now provided in our model [76]. To this end, we show these arguments can be consolidated with our proposed mechanism, as well as with the prediction that DR < 1 at low loads.

Samuel and Berg used fluctuation analysis to determine that the number of steps per revolution was proportional to stator number [106, 107]. In the absence of a specific physical mechanism, this result was interpreted to mean that a motor decreases its elementary step size as it recruits stators. This in turn implied a motor with a high duty ratio, in which each stator acts with the $N - 1$ others to rotate a fixed distance d [105].

In our model, this holds in the high-load regime, where these measurements were made. Though stators disengage between strokes, the duty ratio of the motor is very high because the time spent within a power stroke is far greater than the pauses between subsequent

strokes (DR $= T_s/(T_m + T_w) \approx T_s/T_m \approx 1$) (Figure 4.4b, red circles). Furthermore, the rotor is likely always in contact with at least one stator as the steps of individual stators almost certainly overlap. This accounts for the observed proportional increase in n_{steps} with the number of active stators (Figure 4.4b, red circles).

Note that stator steps still may overlap at low loads (high speeds), though they are less likely to do so because T_m is shorter than at high loads. Our simulations predict that similar analyses in this regime will detect a sublinear increase in n_{steps} with stator number (Figure 4.4b, blue squares).

The second argument was posed by Howard Berg, who posited that if the BFM did not have a duty ratio of close to unity, it could not be processive [10]. The reasoning behind this is as follows. Consider an experiment where a cell is tethered to a surface by the hook of its flagella and is spun about by the rotation of the motor at its base. The cell body is large in comparison to the flagellar motor, and, accordingly, the viscous drag on it is much larger than that on the BFM's rotor. Therefore, if there are no stators to prevent it, the wound tether between the surface and the cell will unwind exponentially: $\theta = \theta_0 \exp(-\alpha t)$, where θ_0 is the initial twist and α is the torsional spring constant divided by the rotational drag coefficient of the rotor. A simple calculation showed that unless a motor had a duty ratio of very close to unity, this tether would unwind too quickly for the stator units to keep up.

We note that concrete evidence is still lacking that slowly-rotating tethered motors do not "lose" steps to the tether connection unwinding. Support for tightly-coupled mechanisms came from reports that the number of ions per revolution was directly proportional to motor speed [82]. However, it was later shown that a loosely-coupled mechanism also produced a linear relationship with the same slope, but non-zero intercept [13]. Regardless, our model construction and parameter choice is such that the unwinding of the tether does not overwhelm the stator in our simulations [76]. A final resolution may be reached using experiments that measure how the ion flux at stall (zero speed) differs between single- and multi-stator motors.

At low loads however, the relative drags of the bead and the rotor are comparable. As we approach the zero-torque limit, the rotor drag may surpass that of the load [80, 79]. For example, we estimated the drag coefficient for the low-load measurement in [72] to be $\zeta_L \approx 0.005$ pN-nm-s-rad^{-1}, which is lower than $\zeta_R \approx 0.02$ pN-nm-s-rad^{-1} [10]. In this case, the bead will move forward as the tether connection unwinds.

More generally, the characteristic timescale of the load's motion is given by its frictional drag coefficient divided by the spring constant: $t_L = \zeta_L/\kappa$. A single-stator motor should have a comparably long power stroke. Note that this is not necessary for a multi-stator motor: steps from different stators may overlap, extending the period during which at least one complex is present.

To illustrate, we consider the second-smallest bead used by Lo et al. [72]. Estimating $\zeta_L = 0.04$ pN-nm-s-rad^{-1} and choosing a spring constant $\kappa = 150$ pN-nm-rad^{-1} at the lower edge of the measured range [19], the characteristic timescale of the load is $t_L = \zeta_L/\kappa \approx 0.27$ ms. A single-stator motor with this load rotated at approximately 110 Hz [72]. Recall that motor speed $\omega \approx \ell/(\langle T_m \rangle + \langle T_w \rangle)$, where the step size $\ell = \frac{1}{26}$ rev and $\langle T_w \rangle \approx 0.2$ ms.

Then $\langle T_m \rangle \approx \left(\frac{1}{26} \right) / 110 - 0.0002 \approx 0.15$ ms, and the load is able to (at least partially) "catch up" to the rotor.

Tether-wind calculation. In his 2003 review article, Howard Berg posed an argument for why torque-generating units in the flagellar motor must have a very high duty ratio [10]. Here, we redo this calculation with the values Berg originally used, and then revise it using our model construction and chosen parameters (see Table 4.1). Though high-load simulations were not used in these conclusions, the following calculation provides an explanation as to how high-load simulations were run in the previous chapter and in [76].

Consider a cell tethered to a surface by its flagellar filament. The cell is spun around by the rotation of the motor at the base of the filament. In the first step of a resurrection experiment, a motor has a single torque-generating unit.

Berg estimated the torque generated by a wild-type motor (with 8 torque-generating units) to be 4000 pN-nm, so that each unit generates about 500 pN-nm of torque. Likewise, he estimated the torsional spring constant of the tether to be 500 pN-nm-rad^{-1}, leading to a twist in the tether of about 1 rad (57°). Since the cell body has a significantly higher drag than the rotor, the tether will unwind exponentially once the stator disengages: $\theta = \theta_0 \exp(-\alpha t)$, where θ_0 is the initial twist and α is the torsional spring constant divided by the drag coefficient of the rotor. Estimating the drag of the rotor as 0.02 pN-nm-s-rad^{-1}, we have that $\alpha = 2.5 \times 10^{-4}$ s^{-1}. Then, if the stator is disengaged for 1.6×10^{-5} s (corresponding to a duty ratio of 0.999 in his calculation), the twist in the tether decreases to $57 \exp(-2.5 \times 10^4 \times 1.6 \times 10^{-5}) = 38°$, or by 19°. It is currently assumed that a single unit steps 50 times per revolution, so that a single step was approximately 7.2°, or less than half of the unwinding. This led to the conclusion that a single torque generator would not be able to keep up if it detached for a time even on the order of 10^{-5} s.

Most estimates have calculated the maximum torque in the BFM to be approximately 2000 pN-nm. Assuming a motor at stall has 11 stators, each stator generates approximately 180 pN-nm of torque. This is also consistent with single-stator measurements in chimeric motors [72]. We estimate the torsional spring constant very conservatively, at the lower end of the experimentally measured range, as 150 pN-nm-rad^{-1} [19]. Then, the tether is twisted by 1.2 rad, or 69°.

The "waiting time" between subsequent steps corresponds to the time required for an ion from the periplasm to bind to an exposed binding site on the stator. In our model simulations, this site is exposed when the angle of the stator is smaller than some ϵ. Here, we take $\epsilon = \frac{\pi}{1500}$ rad $= 0.12°$. Recall that $\langle T_w \rangle = 0.2$ ms. A stator disengages from the rotor from the time it completes its power stroke ($\phi_S \leq 0$) until an ion binds to it. In our simulations, when ϕ_S is in the interval $(0, \epsilon)$, it is able to bind a periplasmic cation while still being bound to the rotor. For the vast majority of the loads considered, the time spent in this interval is negligible compared to $\langle T_w \rangle$, and the stator detaches from the rotor for 0.2 ms at a time, on average. However, in very slowly-rotating motors, the time when $\phi_S \in (0, \epsilon)$ may be large enough to significantly lower the average time that the stator detaches from

the rotor.

Tethered cells rotate at 1.2 Hz, which corresponds to each step taking 32 ms (assuming there are 26 steps per revolution). Since the experiment is performed at very high load, $\langle T_m \rangle$ is approximately 32 ms, since $\langle T_m \rangle \gg \langle T_w \rangle$. Because the BFM lives at low Reynolds number, we assume that the stator moves at a constant speed throughout its power stroke. Then $\phi_S \in (0, \epsilon)$ for $0.12°/20° = \frac{6}{1000} \times \langle T_m \rangle = 0.192$ ms. Then, the average time that the stator is actually detached from the rotor between consecutive strokes at the load considered in our simulations is 0.008 ms. During this time, the tether connection unwinds to $69 \exp(-150/0.02 \times 8 \times 10^{-6}) \approx 65°$, or by 4°. This is less than our assumed elementary step length, $2\pi/26 \approx 14°$.

However, we note here once again that there is not yet concrete evidence that a single-stator motor at very high load does not, in fact, "lose" several steps to the unwinding of the tether connection. This uncertainty will likely be resolved only by experiments which can quantify how the ion flux varies between single- and multi-stator motors (i.e., motors with different duty ratios) at high loads.

4.3   In conclusion

The dynamics of the BFM across applied loads have been of great interest since a two-regime torque-speed curve was proposed several decades ago. Recent experiments reporting that the number of stators in a motor varies across loads have opened some interesting questions, and reopened several more.

For instance, the zero-torque speed has been assumed to be independent of the number of docked stators based on the results of early "resurrection" experiments [18, 103, 128]. Theoretical models after these results were reported have all been constructed to reproduce this behavior at low loads. However, recent experiments strongly suggest that these experiments were never performed on motors with more than a single stator [68], making revisiting this long-held assumption timely.

We note that $\sim 25\%$ of the zero-load motors measured in [68] were interpreted to have two, instead of one, stators. However, it was noted by the authors that motors that were interpreted to have two stators likely had flagella which were incompletely sheared, which may have resulted in an increased load for these motors. Furthermore, this result was reached using a relatively small number of data points, making a statistically significant conclusion difficult to reach. The idea that the stator number varies with load is quite new, and further experiments on the low-load behavior of this motor performed with this knowledge are needed for conclusive evidence in any direction.

In opposition to current assumptions, our simulations predict that the zero-torque speed of the BFM increases with stator number. We note that there was an earlier model that predicted that the motor's speed at low load was not universal [123]. However, the mechanism suggested in [123] was a tightly-coupled one which predicted that this speed would *decrease* with an increasing number of stators. Experiments by Lo et al. [72] (shown in Figure 4.3c)

seem to support the opposite trend, as predicted by our model; however, further experiments at low load are required to make any definitive conclusions. As we mentioned previously, tightly-coupled mechanisms can be differentiated from ours by an experiment testing the intercept of the relationship between the number of ions per revolution and motor speed [13].

Our prediction arises from our assumption that stators detach from the motor when they pause between steps. This assumption is common to most models in which a conformational change in the stator drives motor rotation. This results in a low duty ratio for motors at low load, where the waiting time between steps is at least on the order of the time spent in a power stroke. Because the power stroke duration is much longer at high loads, the duty ratio in this regime is not affected by this unbound state. In this way, our mechanism is consistent with evidence that processive motors at high load must have a high duty ratio.

It is important to note that we do not propose that there is *no* top speed to the motor at low loads: the moving time T_m at zero-torque still takes some, albeit not much, time. The limiting speed of the motor at low loads will occur when the duty ratio of the motor approaches 1 (i.e., when the waiting time between subsequent power strokes T_w no longer significantly decreases with the recruitment of additional stators). Our simulations suggest, however, that this top speed might not be reached by motors with close to the maximum number of observed stators (Figure 4.3c), let alone by single-stator motors.

Recently, Lo et al. presented evidence of increasing zero-torque-speed with stator number in chimeric, sodium-driven motors [72]. However, this result was not fully explored as the authors focused on understanding single-stator motor dynamics. Further such experiments, especially on wild-type motors, would directly test the hypothesis presented here. While previous experiments have clarified other aspects of low-load motor behavior [130, 129, 120], the explicit characterization of the dependence of the limiting speed on the number of stator units deserves a more focused study.

The discovery that stator recruitment in the flagellar motor is dynamic and load-dependent forces us to go back and reconsider many things that were considered common knowledge in the field. We certainly do not claim that the current published data on the wild-type H^+ motor support or validate our model (though there is support in the sodium-driven motor). However, because the prior experiments must be reevaluated in light of new evidence, we do claim that further experiments are required to reach any definitive conclusions.

We hope that this chapter, and really this thesis in general, has emphasized that even those questions long-believed to be closed must be periodically critically examined when new information arises. We strongly hope that our proposal of this model will reinvigorate the question of how the flagellar motor's low-load speed depends on stator number, and, in particular, will provide the momentum for experiments conducted with all the current knowledge taken into account.

Chapter 5

The year(s) of magical thinking: validation experiments

> "We imagined we knew everything....but in fact, I have come to see, we knew not the smallest fraction of what there was to know."
>
> — Joan Didion, *The Year of Magical Thinking*

We hope that, by now, it has been made clear — either by example or, at least, by our constantly saying so — that a (if not the) major theme in this dissertation is how fundamentally and intricately theory and experiment weave together, and how much they both benefit from this interaction. In the past few chapters, we have presented our theoretical work and emphasized its grounding in experimental reality. In this chapter, we do the opposite: Inspired by our theoretical predictions, we propose and design experiments to test and validate our models. In particular, we aim to directly test, for the first time, a prediction made by the models presented in earlier chapters of this thesis.

A unique feature of our model (relative to other recently proposed ones) is that motor rotation is **loosely coupled** to ion flux — that is, not every ion passage results in an equally productive power stroke. This can be understood intuitively if one considers the (unlikely, but this is hypothetical!) event in which protons arrive at two independent stators at exactly the same time. In this case, both stators will execute their power strokes simultaneously, but the motor will move the same angular distance as if only one stator had been pushing. Therefore, the distance traveled by one *perfect* power stroke could also be due to two "imperfect" strokes, and thus use twice the number of expected ion passages.

The content of this chapter, and so its exposition and structure, differ from previous chapters in two important ways: (1) it concerns practical/experimental, rather than theoretical, work; and (2) it deals primarily with methodology — that is, it focuses on optimizing setups for answering a biological question, rather than with the answer of that question. To this end, we chronicle our troubleshooting, and detail out *both* our successful and failed protocols chronologically, focusing on which features changed as our experimental setup was logically built up and improved. We choose to present this chapter in this format (as opposed to simply showing the "final state" of the setup at the time of submission) in the hope that such exposition will prove instructional to others attempting similar or related experiments.
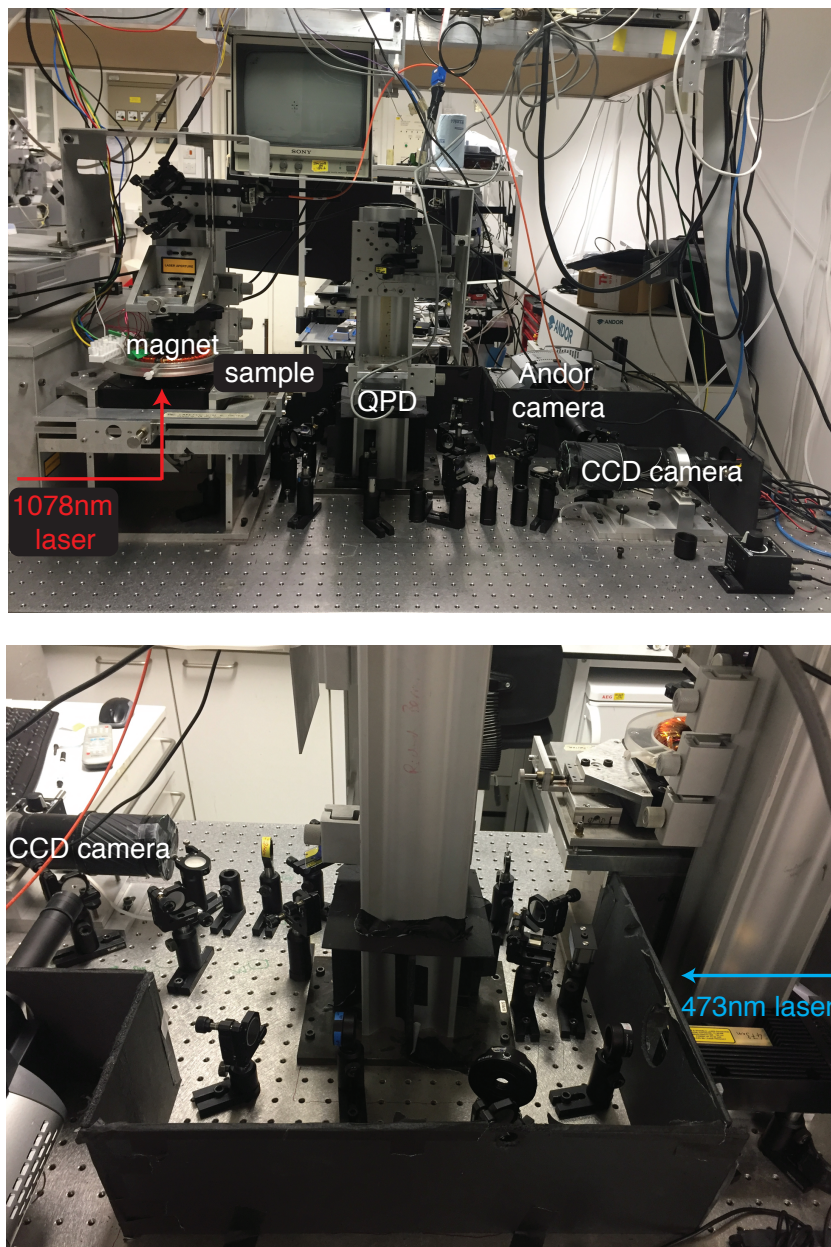
Figure 5.1: Two photographs (front and back view) giving an overview of the entire setup. Sources and light paths for the two lasers are noted in red (infrared light) and blue (blue light). Details and descriptions of subsets of this setup are provided in later portions of this chapter and in the relevant references as cited.

A note we would like to emphasize is related to our second point. The setups presented in this chapter (and in Appendix B, where full protocols for every experiment mentioned are provided) will be used towards answering the questions outlined above after this thesis is submitted. For this reason, they will almost certainly evolve (well) past the states they are presented in here; they are not — as of course nothing is in science, and especially not in practical experiments — final.

5.1 Components of our experimental setup

In this section, before we outline the details of our experiment, we first take the time to describe our experimental setup, component by component. An overview of the entire setup is provided in Figure 5.1. This setup is constructed on a laminar flow, actively damped, optical air table (Newport S2000). The microscope is designed to incorporate three illumination sources in an illumination pathway for condenser bright-field. The three illumination sources are a 1064 nm (Elforlight, Northants, UK) diode-pumped solid-state laser, a 473 nm (Oxxius, France) electrically-pumped semiconductor laser (high-power laser diode), and a high-power LED (Thorlabs, NJ, USA).

The setup is enclosed either by a metal (constructed from our drawings by the University of Oxford Physics machine shop) or black foam board (hand-made) cage system, in order to minimize the effects of dust and ambient light. Several portions of this cage system have been removed for the photograph shown in Figure 5.1; some obscuring pieces remain because they are too unwieldy to remove without misaligning the setup.

Portions of this setup have been inherited from previous members of the Berry Lab at the University of Oxford; the contributors are noted throughout and readers will be accordingly directed to the relevant sources for further, more detailed, information.

Microscopy

The flagellar motor is too small to be seen with visible light, but luckily many ways have been developed to gather information about its behavior. The two most common of these have been the **tethered cell** and **bead assays**. In the former, a cell is attached to a surface (microscope slide) by its flagellar filament or hook and the spinning cell body is used to infer the dynamics of the motor. In the latter, a bead is attached to the flagellar filament or stub, and *its* rotation is used to infer the dynamics of the motor. Here, we will end up using a combination of the two — but more on that later (in Section 5.2).

In bright-field microscopy, illumination light diffracted by the sample is collected by the objective, producing a diffraction pattern in the back focal plane and a focused image in the image plane. The incident light that does not interact with the sample is transmitted, creating (in conjunction with higher order diffracted rays) a contrast image, which shows as a dark image against a bright background. This form of imaging is ideal for transparent specimens with medium optical density (like, for instance, $\sim 1\mu m$ sized polystyrene beads).
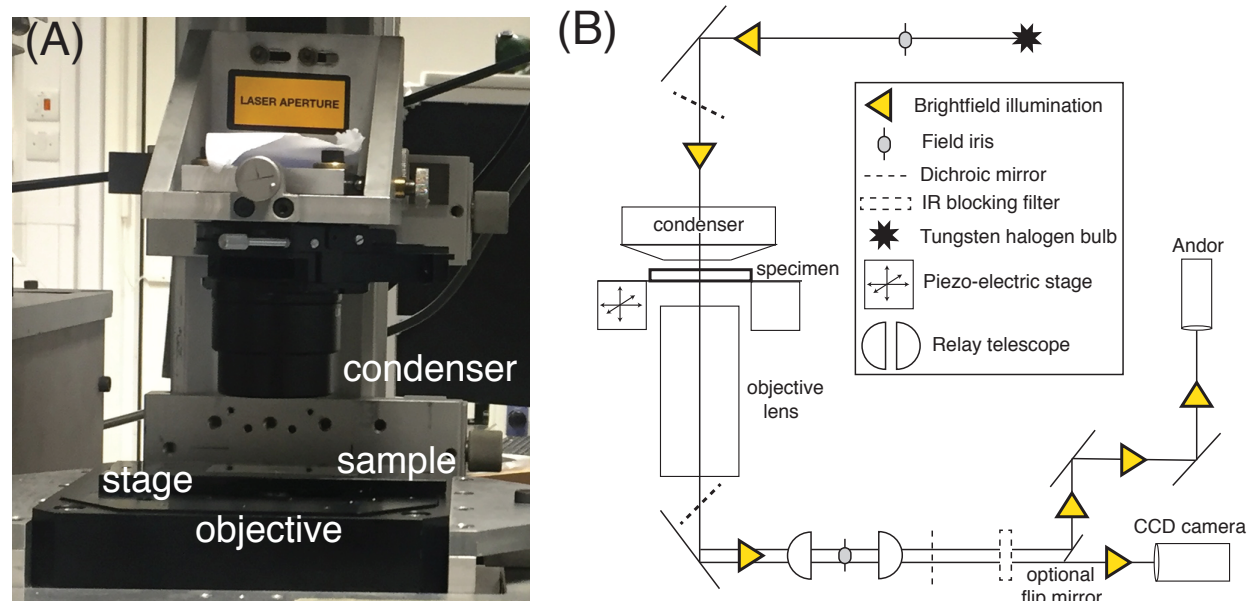
Figure 5.2: A photograph zooming in on the objective, stage, and condenser used (left) and a schematic of the optical setup for bright-field microscopy (right) showing two alternate illumination paths that conclude either at a CCD camera or an Andor Ixon camera depending on the positioning of an optional flip mirror. An overview of the entire setup is provided in Figure 5.1.

Our setup makes use of an inverted bright-field microscope (seen as part of Figure 5.1 and on its own in Figure 5.2). The bright-field image is projected onto either a CCD video camera by a zoom lens (for initial positioning) or a high quantum efficiency 128×128 pixel Andor Ixon high-speed video camera. The path for the outgoing light was chosen using a flip mirror. The CCD records onto a DVD (LiteOn, Taiwan), while the Andor records directly onto a controlling computer.

Optical trapping

For our purposes, it is important that we establish a method to reliably track the speed of the motor in time. Optical tweezers apply or measure pN-level forces on an object (here, a polystyrene bead) using laser light. Usually (and this work is no exception), infrared wavelengths are chosen, because they impart a low level of photodamage to biological specimens. The beam is brought to a diffraction-limited focus by a high numerical aperture microscope objective lens. Particles with a higher refractive index (as compared to the solution they are in) are drawn into a potential well at the focal point as they come close to the focus. This can be best understood either in terms of minimizing the energy in the laser radiation field or by considering the exchange of momentum between the trapped particle and the photons

it deflects (whichever seems more intuitive).

Displacement of the bead can be measured either from the image of the trapped particle, or by measuring the deflection of the trapping beam. We choose the latter, determining the (x, y) position of the magnetic bead by collimating the transmitted laser beam (via a condenser). In this method, called **back focal plane (BFP) interferometry**, the associated intensity shift in the back focal plane of the condenser is imaged onto a quadrant photo-diode (QPD) [51]. This method is well-suited for experiments that require a high-time resolution (like this one!), because the high intensity of the focused laser beam avoids the problem of shot noise.

The laser trap used in this work was implemented on the same inverted bright-field microscope described in the previous section (and as shown in Figure 5.1). The major components of this setup were initially built and aligned by Dr. Alex Rowe (see [104]); for the work in this chapter, we have added some components necessary for our experiments (e.g., fluorescence for sodium imaging, magnetic tweezers), and rearranged and realigned the full setup to this end. The components and general structure of the laser trap remain largely unchanged as inherited from Dr. Rowe, and accordingly, detailed information regarding the construction and calibration of this trap can be found in [104].

The trap consists of a home-made (a "how-to" is provided in [104]) single beam, single focus 1064 nm laser. This beam was attenuated by a $\lambda/2$ waveplate and polarizer, and then passed through two beam-expanding telescopes to slightly overfill the back aperture of an oil-immersion objective of N.A. 1.4 (CFI plan-fluor 100x, Nikon, Japan). A condenser lens re-collimates this beam to fill the surface of a quadrant photo-diode (Pin-SPOT 9DMI, UDT Sensors, CA, USA). The signals from each quadrant are amplified using a home-made [104] current-to-voltage amplifier and is sampled at up to 5 kHz (controlled by LabVIEW software, National Instruments UK, Newbury, UK). A long-pass filter (1000 nm cutoff) is placed in front of the diode to block ambient light.

The four photocurrents to each quadrant of the photodiode are manipulated in order to obtain (x, y) signals for the bead's position as follows [69, 104]:

$$x = \frac{(Q_3 + Q_4) - (Q_1 + Q_2)}{(Q_1 + Q_2 + Q_3 + Q_4)}, \qquad y = \frac{(Q_1 + Q_4) - (Q_2 + Q_3)}{(Q_1 + Q_2 + Q_3 + Q_4)}, \qquad (5.1)$$

where Q_i denotes the voltage signal from quadrant i of the QPD; quadrants are numbered starting at the upper left and moving clockwise. The denominator of these expressions denotes the relative magnitude of the signal $(Q_1 + Q_2 + Q_3 + Q_4)$. This positional data was then interpreted into rotational speed-time traces, as is outlined in Section 5.3.

Fluorescence

Fluorescence microscopy grants us the ability to specifically target and image molecular components in live cells, making it an incredibly useful tool in modern biology (and in the experiment we lay out in this chapter!). A **fluorophore** (fluorescent chemical compound) re-emits light upon excitation by light. At room temperature, most molecules exist at the
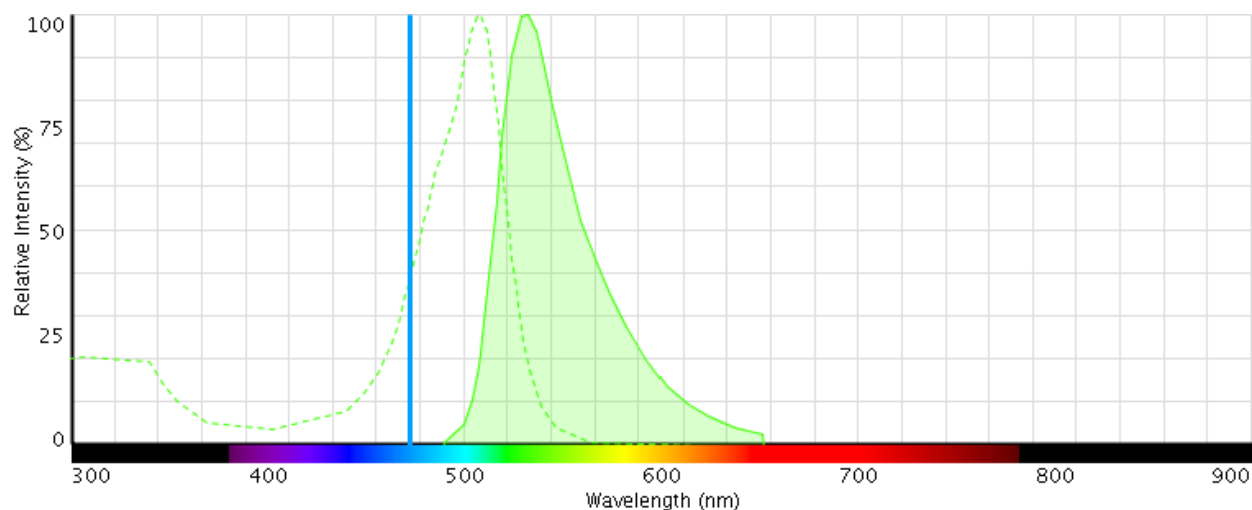
Figure 5.3: Excitation (white, dotted outline) and emission (green, solid outline) spectra for CoroNa Green, the sodium indicator fluorescent dye used. A blue vertical line denotes the wavelength of the laser used for excitation (473nm). Image from ThermoFisher.

ground electronic state. When a fluorophore absorbs a photon of a specific wavelength, one of its electrons jumps to an excited state and re-emits light at a (longer) wavelength during its decay back to the ground state. This work makes use of CoroNa Green, a fluorescent sodium indicator; the excitation and emission spectra for this molecule are given in Figure 5.3.

Fluorophores can go through many cycles of excitation and emission, after which the molecule is permanently rendered incapable of further fluorescence due to light-induced chemical damage (**photobleaching**). In our setup, we attempt to delay photobleaching by using short time exposures (via shuttering the laser in between measurements) and using minimal excitation light (via installed polarizers to lower laser intensity).

Dr. Sam Tusk's help was crucial in putting together the following fluorescence setup. We used a 473 nm laser diode to excite the CoroNa Green dye. Laser intensity was modulated using a continuously-variable neutral-density filter wheel (Thorlabs) and a polarizing beamsplitter cube. The laser illumination path was passed through two telescopes, dichroic mirror, and emission band-pass filter set XF100-2 (Omega Optical, Brattleboro, VT). The dichroic is an edge filter used at an oblique angle of incidence (typically 45°) to efficiently reflect light in the excitation band and to transmit light in the emission band. The purpose of the emission filter is to pass only the wavelengths emitted by the fluorophore and block all undesired light outside this band (especially the excitation light).

The laser then enters the shared pathway, illuminating the sample through the oil-immersion objective described previously. Images are obtained using the Andor high-speed camera, and are saved directly onto the controlling computer.
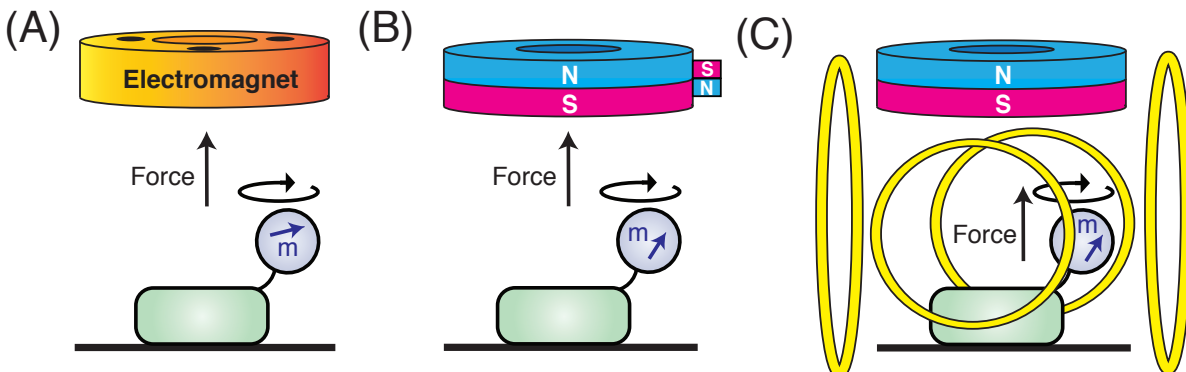
Figure 5.4: Examples of magnetic tweezer configurations for single-molecule measurements on the flagellar motor. **(A)** Magnetic tweezers using a three-pole electromagnet to create a rapidly rotating horizontal magnetic field (this work; see also, [88]). **(B)** Magnetic tweezers incorporating a small side magnet to create a horizontal perturbation to the cylindrical magnet's vertical field [70]. **(C)** Electromagnet torque tweezers using two pairs of Helmholtz coils for dynamic control of the horizontal magnetic field [56]. For more details on the use of magnetic tweezer apparatuses for single-molecule experiments, we refer the reader to [46].

Magnetic tweezers

In addition to optical methods (discussed earlier), magnets are another widely-used class of methods for applying torque to single molecules. In addition to optical methods (discussed earlier), we also use electromagnets in our tweezer setup. In past studies, tweezers have also been constructed using permanent magnets or pairs of Helmholtz coils (Figure 5.4). All of these methods follow the same basic principle: Torque is generated as a result of the interaction between the magnetic dipole moment $\vec{\mu}$ and the magnetic field $\vec{B}$:

$$\vec{\tau} = \vec{\mu} \times \vec{B}. \tag{5.2}$$

Therefore for particles with a permanent dipole, the maximum torque is attained when the angle between the dipole moment and the magnetic field is 90°. We use **superparamagnetic** beads (i.e., like paramagnets, they become magnetized in the presence of an external magnetic field but have a far larger magnetic susceptibility). Superparamagnetic beads consist of aggregates of randomly oriented iron oxide crystals (of ~5-10 nm), and there is a small inhomogeneity in the beads' magnetic susceptibility [94, 59]. If they were perfectly symmetric, their magnetization would tightly follow the field, and no torque would be exerted on the bead. The magnitude of torque delivered to superparamagnetic beads is then given by (for a full deriviation, see [88]):

$$\tau = \frac{\alpha M_{\text{sat}} B}{2} \sin(2\theta), \tag{5.3}$$

where B is the strength of the magnetic field, α is the anisotropy of the beads, M_{sat} is the saturating magnetization of the bead, and θ is the angle between the bead easy axis and the
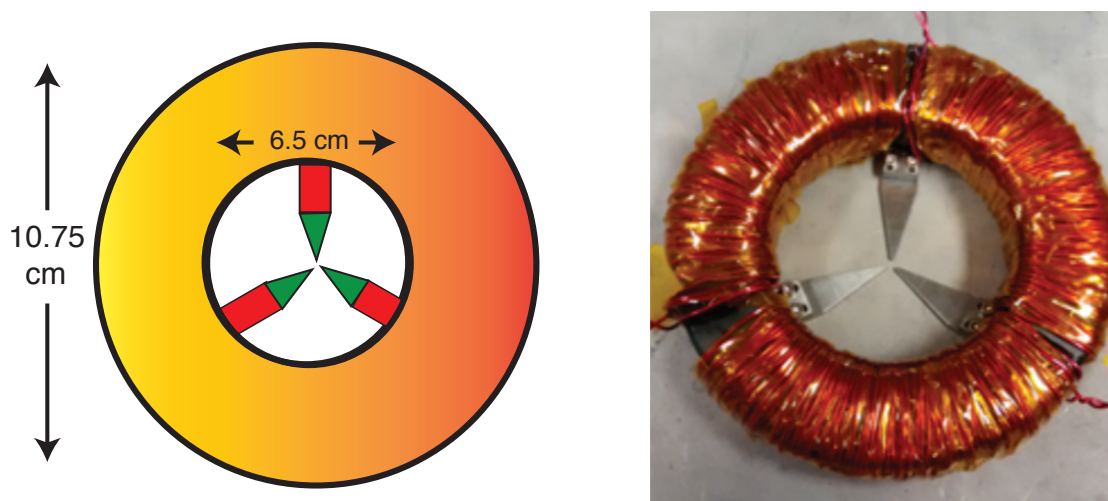
Figure 5.5: Top-down schematic (left) and photograph (right) of the electromagnet used for our magnetic torque tweezers. The orange region is composed of a highly magnetic-permeable ferrite core (0W-49718-TC, Magnetics). The red block of soft iron is epoxy-glued and fixed to the ferrite core while the triangular green pole pieces are bolted to the soft iron block. These pole pieces are removable and the slots present in the soft iron block allow the gap-spacing between the pole pieces to be varied. Figure adapted from [69].

magnetic field. The maximum torque on the bead is then attained when $\theta = 45°$ (this will come into play again later!).

The main component of our magnetic tweezers consists of a three-pole electromagnet (Figure 5.5), chosen primarily to minimize material in the optical path. The electromagnet was constructed with a highly magnetic permeable ferrite core (permeability $\sim$10,000; W material, Magnetics) and soft iron. An enameled 20 SWG 1 mm diameter magnetic wire was wound three times around the electromagnet. A polyimide film (Kapton) was used for electrical and thermal insulation between wire layers and at the ends of each coil. The electromagnet used in our setup was built by Dr. Ren Lim during his time at the University of Oxford; further details on its initial construction and calibration can be found in [69].

Currents were driven through each of the three coils by a car audio amplifier (EAPA450, Nikkai) and dictated through the circuit by a load resistor with resistance 2.3 Ω with a power rating of 150 W (HS150 2R2 J, ARCOL). This electromagnet was installed using a perspex holder (custom-made from our drawing by the University of Oxford Physics machine shop) within the aforementioned inverted bright-field microscope such that its position is centered relative to the objective and the condenser.

The stage holding the sample is set to move freely relative to the magnet; in our setup, the stage is fixed to the optical bench and moves independently of the magnet, objective, and condenser. During experiments, the magnet is brought to be almost in contact with the sample. Given the thickness of the coverslips used, the magnet is approximately 0.015

mm away from the beads it is meant to manipulate. Figure 5.1 shows an image of the electromagnet installed as a part of the microscope setup.

5.2 Coupling between ion flow and motor rotation

One of the most fundamental physiological properties of the flagellar motor is the mechanism by which it couples ion flow to rotation. The difficulty of quantifying this property lies in the number of simultaneous measurements required to do so: both the ion flux and the motor speed/torque need to be tracked. Another particular difficulty arises in making the first of these measurements: quantifying the flow of ions through a single channel is challenging, and high-resolution direct measurements of the flux through the flagellar motor have not been made. We begin this section by addressing this challenge.

Ion flux through single motors

The only previous study to attempt to measure flux through the flagellar motor was made by Meister et al. [84]. The authors reported measurements of the proton flux deduced from the rise in pH in the external medium of cells swimming in suspension. Simultaneous measurement of the motor speed was inferred from the vibrational motion of the swimming cell body. These calculations led to an estimate of a rotation-dependent flux to the motor speed of 1240 ± 240 protons per revolution, and the lack of resolution in the measurement prevented the authors from making a concrete conclusion as to whether the motor operated by a tight- or loose-coupled mechanism.

We have set up an experiment for this purpose as follows: using a fluorescent indicator, we will directly measure ion flux in single cells. By attaching beads to flagellar stubs, we will simultaneously track the speed of these cells in order to track how flux changes with speed. We propose that an estimate of a (constant or non-constant) number of ions per revolution can be inferred from such measurements. To minimize variance between cells, we will also attempt to vary the speed within a single cell using magnetic torque tweezers: In this way, we can estimate the number of ions per revolution at various speeds in the same motor.

Bacterial strains, growth and preparation protocols. For the work presented here, we shift our attention to sodium-driven motors, using an *E. coli* strain (MTB24) with plasmid pYS13 (*pomApotB*), which expresses chimeric stator proteins induced by isopropyl-β-D-thiogalactopyranosid (IPTG). The parent for this strain was YS34, prepared at Nagoya University by Dr. Yoshi Sowa and brought to the Berry Lab in 2003.

This strain has the following genotype: $\Delta cheY$, $\Delta pilA$, $\Delta motAB$, *fliC*::TN10 [114]. These denote the following deletions: $\Delta cheY$ means CheY has been deleted, and so the motor does not switch (the bacteria is a "straight swimmer" and does not tumble) [108]. $\Delta pilA$ means that bacterial pili — the short, hair-like structures on the surface of the cell (see Figure 1.3) — are not expressed in order to prevent rotational markers adhering to them. $\Delta motAB$
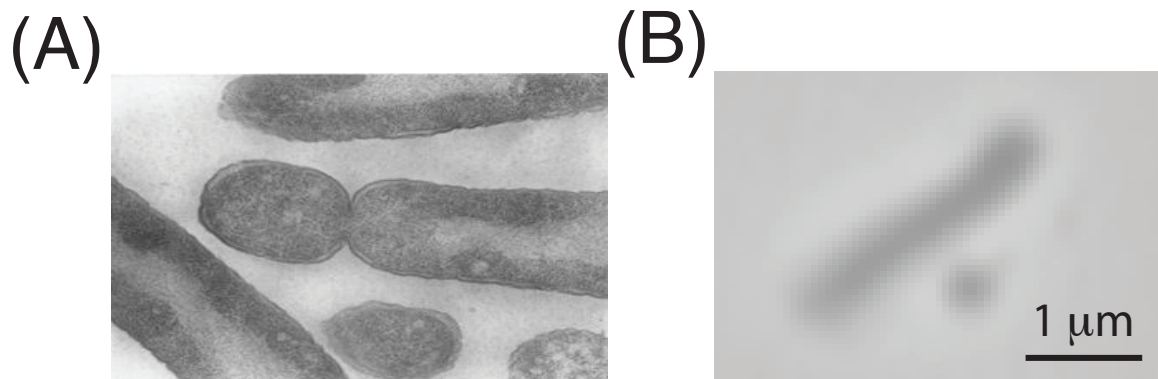
Figure 5.6: Mutations in the cell-division machinery of *E. coli* result in unequal division and the generation of small, anucleate "minicells". **(A)** Thin-section electron micrograph showing a cell producing a minicell. Figure from [2]. **(B)** Brightfield image comparing the size of a normal-sized bacterium from our MTB24 strain [111] with a minicell.

means that the (non-chimeric, proton-driven) stators have been deleted [33]. $fliC$::TN10 indicates that transposon TN10 has been inserted into the $fliC$ gene, meaning the bacteria do not have a flagellar filament [63, 105]. Cells of this strain also had an Avi-tag $flgE$, which indicates that FlgE protein in the hook has been replaced with an Avidity-tagged peptide-fused FlgE for conjugation of biotin [25].

Finally, the strain we use has an additional mutation in minB, which results in an unequal cell division and the formation of anucleate, spherical "minicells" (Figure 5.6) [48]. All data reported was taken from these minicells; this strain was developed from the MTB24 strain and gifted to us by the Lo group in Taiwan. This was done because in their original development of the method we use, Lo and colleagues reported that while the majority of the signal from internal sodium concentration $[Na^+]_{in}$ comes from chimeric motors, there is still a large intercellular variance observed. The authors postulate that this may arise in large part from the variance in flagellar number [71]. While normal *E. coli* cells can have between four to six flagellar filaments distributed over the cell body [67], minicells are estimated to have at most one filament (and thus, at most one motor contributing to the internal sodium concentration). Details of the preparation of MTB24 culture are given in Figure 5.7; full protocol for growing and preparing this strain is provided in Appendix B.

Loading cells for dynamic measurements of sodium flux. For fast dynamic measurements of ion-flux in single bacterial cells, we use the method described in [71]. As mentioned previously, we use CoroNa Green Sodium indicator dye (spectra shown in Figure 5.3). In order to "load" bacteria with this fluorescence indicator, cells were suspended in **high EDTA motility buffer** (10mM potassium phosphate, 85 mM NaCl, 10mM EDTA, pH 7.0) to increase the permeability of the outer lipopolysaccharide (LPS) membrane. CoroNa Green
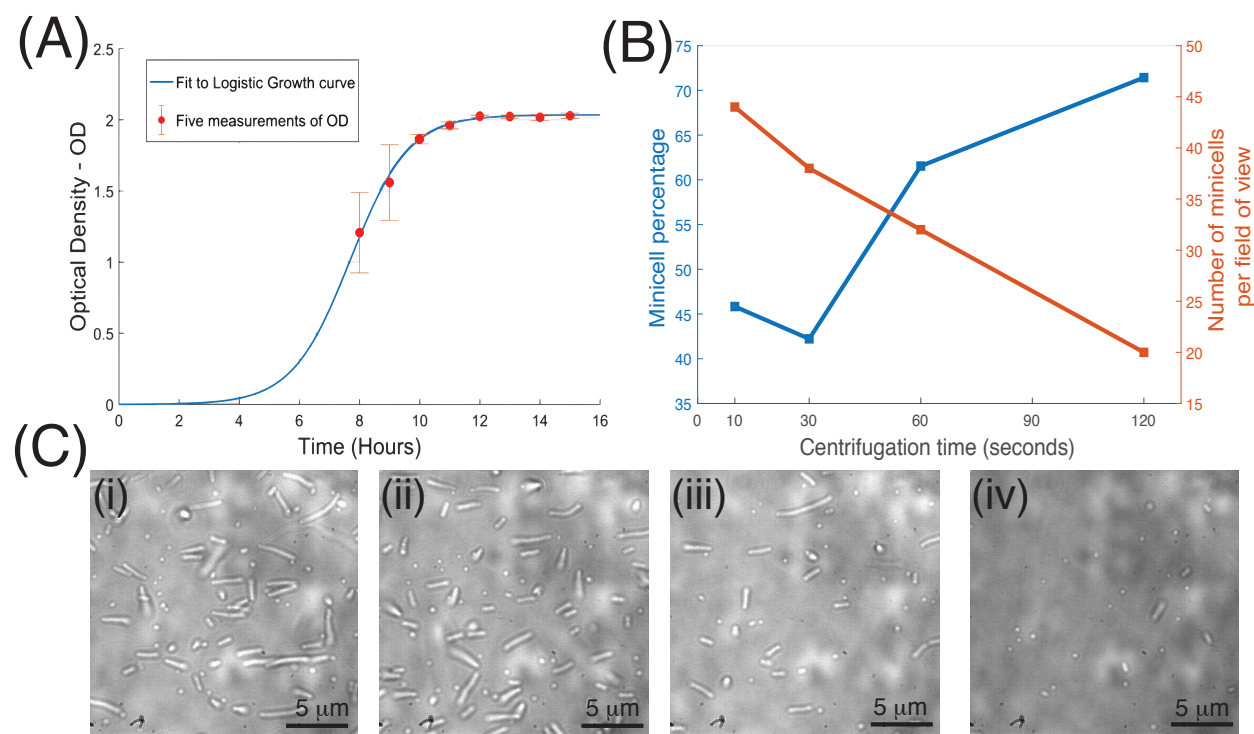
Figure 5.7: Growth and preparation of a MTB24 strain culture. **(A)** Growth curve for the MTB24 minicell strain, set to shake at 150rpm at 30°C (5mL TB, 50μM IPTG, 25μM chloramphenicol); optical density provides a metric for cell number. The strain shows the standard logistic growth, reaching stationary phase after approximately 12 hours. Cells were collected after 16 hours to allow for further minicell formation. **(B)** and **(C)** Differential centrifugation allows separation of normal-sized cells from minicells. Representative bright-field images for samples with initial spin times of 10s, 30s, 1 min, and 2 min (respectively) are shown in **(C)**. Initial spin time of 2 minutes removes most large cells from the solution, leaving mostly minicells behind (**(C.iv)**, rightmost panel). Absolute number of minicells (**(B)**, red line) is of less importance to us as the initial volume of culture can be made arbitrarily large; we are mostly concerned with the proportion with respect to normal-sized cells (**(B)**, blue line).

was added at a 40 μM concentration and cells were incubated for 30 min in the dark at 37°C. Cells were washed three times in **high-sodium motility buffer** (10mM potassium phosphate, 85 mM NaCl, 0.1mM EDTA, pH 7.0) to remove excess dye.

The loading protocol was optimized to maximize the fluorescent signal from loaded cells while assuring that the motor and sodium-motive force (SMF) are unaffected by the dye. Only a small increase in fluorescence was seen for higher loading times and higher concentrations of dye, with the price of a higher number of observed broken cells post-loading. The measured speeds of a 1μm bead attached to a tethered minicell (total load of this "mini-

cell+bead" arrangement is estimated to be equivalent to the load of a 1.5μm bead attached to a motor) were not significantly different between measured populations of loaded and unloaded cells (data not shown). Shorter loading times and/or lower loading concentrations of dye gave reduced fluorescence intensity.

An updated, inverted bead assay. Because of the required sensitivity of the measurements we wish to make, we further aim to reduce the effects of cell-to-cell variance by taking measurements at different speeds in a single cell by varying motor speed using the magnetic tweezer setup described in Section 5.1. So, now that we have a magnet set up, we just need something to which we can apply torque!

The **bead assay** has been used extensively in past studies on the flagellar motor [105, 114, 103]; the version of this assay described here has several inherent improvements: (1) we use a bacterial strain which does not express the flagellar filament, which allows for significantly reduced drag due to direct attachment of the bead to the hook; (2) this strain also endogenously expresses biotinylated hooks [25], which allows us to use streptavidin-coated beads and take advantage of the strong avidin-biotin binding (at least, in theory; the final protocol does not end up using this interaction for this purpose!); (3) we use spherical superparamagnetic beads (instead of simple polystyrene ones) in order to be able to separately track *and* manipulate motor speed.

For all results shown here, we use Dynabeads MyOne Streptavidin C1 beads (ThermoFisher), which are 1μm microbeads with a (carboxylic acid) hydrophobic coating and a monolayer of recombinant streptavidin covalently adhered to the surface. For these beads, $M_{\text{sat}} = 2.27 \times 10^{-23}$ Am^2 [69]. We estimate that $\sim$60 mT should allow us to spin the beads at speeds high enough to differentiate ion flux using our fluorescence setup (as discussed previously) [69]. Positional data from beads was acquired using LabVIEW as described in Section 5.1, and analyzed using MATLAB (Mathworks Inc., MA, USA); more information to this end is provided in Section 5.3.

Cells were stored, grown, and prepared as indicated in Section 5.1 and in the full protocol in Appendix B. **Tunnel slides** were made by sandwiching two glass coverslips (of dimensions 22$\times$40$\times$0.15 mm and 22$\times$22$\times$0.15 mm) together, separated by double-sided tape about 0.1 mm thick, resulting in a "tunnel" about 5 mm wide (Figure 5.8). In our first iteration of this assay, we flushed 50 μL of poly-L-lysine (PLL; 0.1% in H$_2$O, Sigma Aldrich) into the tunnel slide for 1-2 minutes, before rinsing it out with motility buffer. Cells diluted in high-sodium motility buffer were then flushed into the slide (50 μL) and allowed to sediment for 10-15 minutes; unstuck cells were then flushed out with more motility buffer, and beads were added to sediment (and hopefully attach to the hooks!) for another 5 minutes. Finally, unstuck beads were rinsed out using the motility buffer. This assay reproducibly provided high yields (Figure 5.8(A), rightmost panel).

While the PLL slide bead assay (applied to normal-sized cells) is a tried-and-true protocol, we originally felt that it may not be quite right for our purposes. Recall that the torque applied to a superparamagnetic bead by our tweezers obeys a sin(2θ) rule, where θ is the
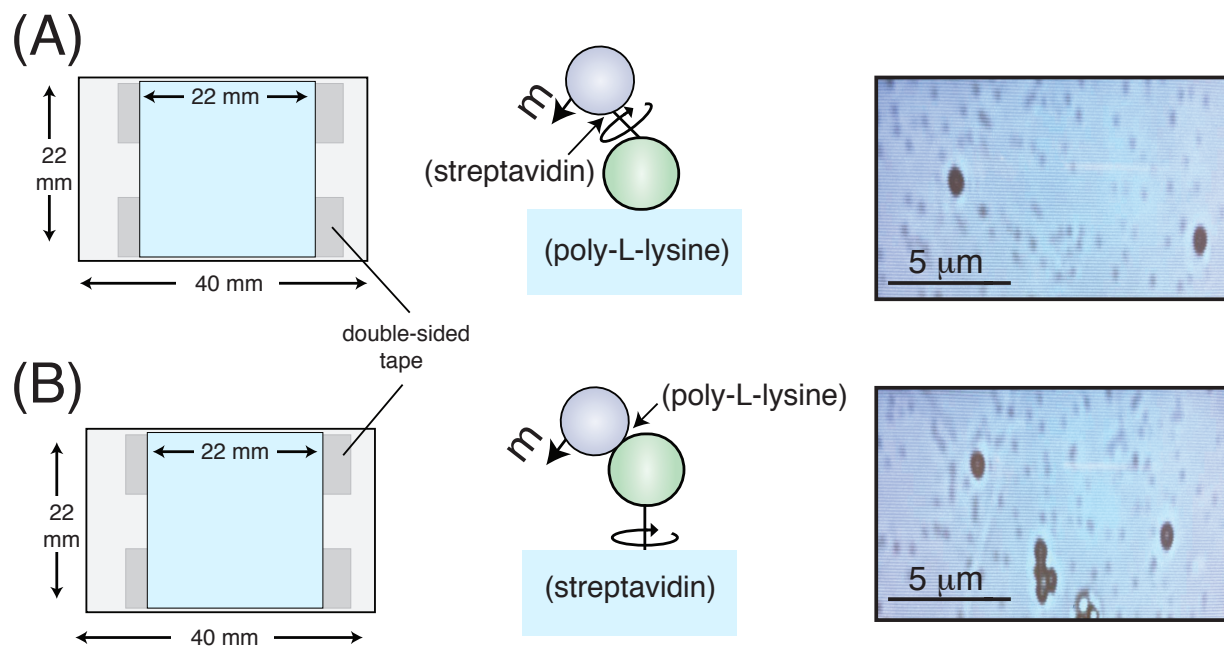
Figure 5.8: The setup of the bead assay using **(A)** poly-L-lysine- (PLL-) and **(B)** streptavidin-coated surfaces. *Left panel:* Tunnel slides are made by sticking together two coverslips using double-sided tape. *Middle panel:* Schematic of how minicells attach to the coverslip and how superparamagnetic beads are then subsequently attached to the cell in each version of the bead assay. Right panel: Brightfield images showing our (comparable) yields of attached minicells for both versions of the bead assay. Note, however, that the inverted cell assay **(B)** leads to more frequent aggregation of beads because coating them with PLL makes them non-specifically sticky, including to each other.

angle between the magnetic field and the bead's easy axis. Now, in the PLL assay, a minicell lands onto the slide randomly, such that its flagellar stub (and thus, axis of rotation) may be oriented in anyway; this is particularly salient when we are using spherical minicells vs. elongated normal *E. coli*, which have far lower curvature and thus far less variance in the orientation of their hooks (Figure 5.8(A), middle panel).

If the hook is oriented at a small angle α from the vertical, the angle between the cell's easy axis and the magnetic field θ will vary by $\pm\alpha$ over the course of a single period of rotation. Then from Equation (5.3), the torque applied to the bead over a period will vary between $\tau(\theta + \alpha)$ and $\tau(\theta - \alpha)$. Recall that in the low Reynolds number environment in which the BFM resides, there is no "coasting" (that is, without any inertia, the bead will only move according to the torque being applied to it *at that instant*), and so the bead may not be able to be driven at a constant speed if the range of applied torque is too wide.

Additionally, the bead then lands with its axis oriented randomly, further lowering the chances that we will be able to manipulate the motor effectively using our tweezers. This
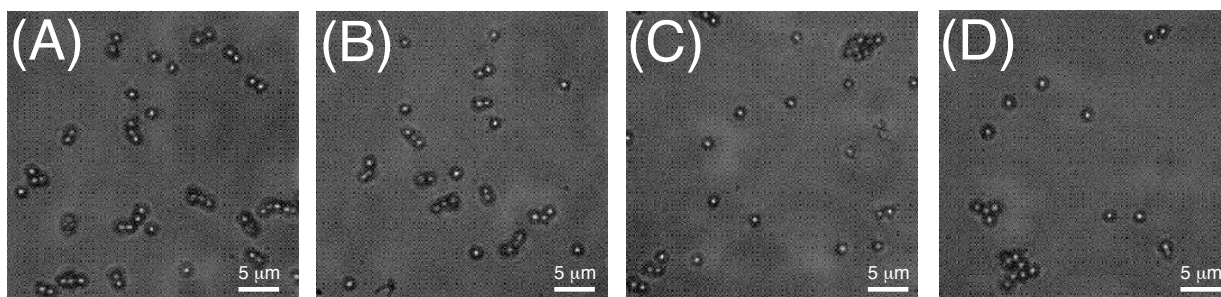
Figure 5.9: Increasing dilution of poly-L-lysine coated beads (up to a certain point) reduces clumping. Brightfield images are shown for 4 µL of beads dissolved in **(A)** 50 µL, **(B)** 100 µL, **(C)** 300 µL, and **(D)** 400 µL of solution. No significant improvement is seen after ∼100x dilution.

latter issue can (and will) be alleviated by allowing the beads to settle within a Helmholtz coil; however, the randomness in the orientation of the cells' hooks remains problematic.

One way to circumvent the issue of randomly oriented hooks is to attach the cells to the coverslip not by their cell bodies, but by the (biotinylated) hooks themselves, thus fixing the axis of rotation. From now on, we refer to this assay as the **inverted cell assay**. We do this by functionalizing the coverslips with streptavidin as follows (detailed protocol is provided in Appendix B): 50µL of biotin-BSA mixture is flowed through the tunnel slide and then washed out with motility buffer after 20 minutes. This is followed by flowing streptavidin into the space. After washing out the streptavidin 20 minutes later, a dense cell solution is flowed into the tunnel slide.

Note our use of the word "dense": PLL creates a non-specifically sticky surface so that a cell needs only hit the surface once to attach. In contrast, the streptavidin slide will capture a cell only if it hits with its biotinylated hook, which may require several interactions with the surfaces before a cell successfully attaches. We first attempted the streptavidin tethering with the non-minicell strain of MTB24 for proof of principle, and were ecstatic to get reproducibly high yields (not shown).

However, for a long time, we were unable to get comparable (or even reasonable) yields with the minicells. We finally realized this is likely due to the fact that the **scale height** ($h = \frac{kT}{mg}$, which for small particles represents roughly their mean distance above a surface) of the minicells was far higher than that of the normal-sized cells due to their reduced size. This discrepancy is not as noticeable in the PLL assay (since only one "trip" to the slide surface is needed) but becomes prohibitive for streptavidin slides. We overcome this hurdle by placing the slide with cell solution in a swinging bucket centrifuge to raise the "gravitational force" that the minicells experience (to ∼10g), thus lowering their scale height. This, at last, allows us to obtain yields comparable to that of the PLL slide assay (Figure 5.8(B), right panel).

Finally, once the minicells are tethered to the surface by their hooks, we must figure out a way to attach our superparamagnetic beads to their cell bodies. As the biotin on their hooks
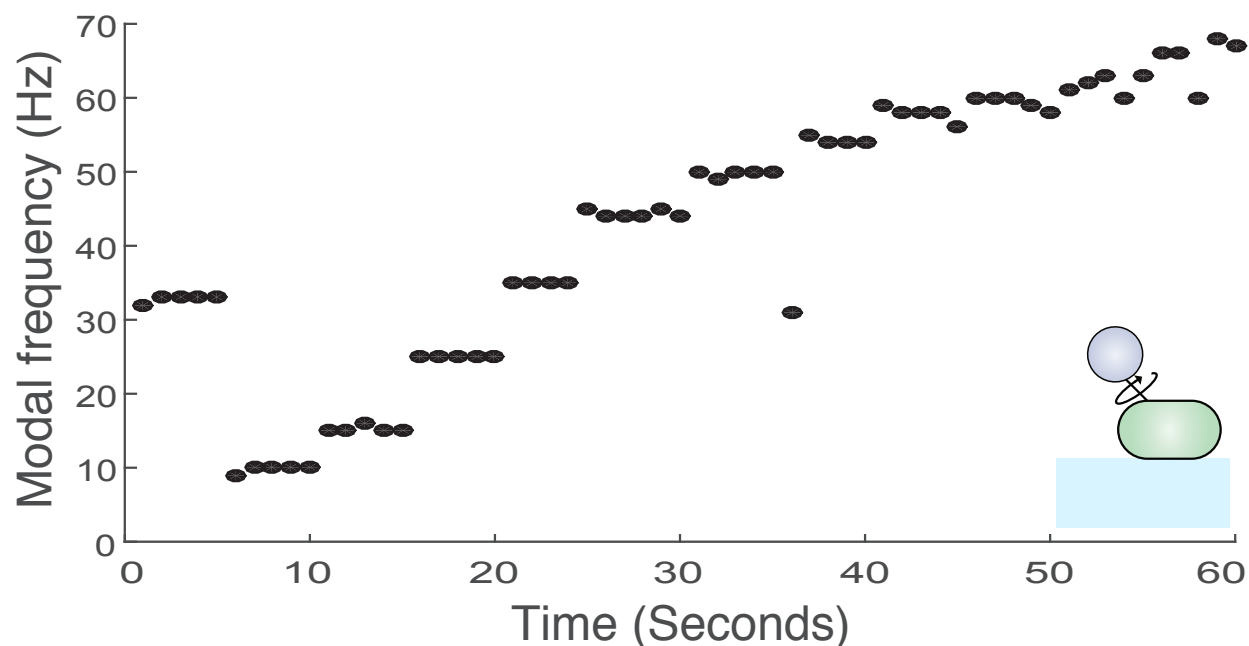
Figure 5.10: Example speed-time trace showing a PLL-tethered cell with hook-attached bead following an external magnetic field at successive speeds increasing by 10 Hz every 5 seconds up to ∼60 Hz. The natural speed of the cell (shown in the first 5 seconds of the trace) was ∼30 Hz. The bead begins slipping and failing to follow the external field at speeds larger than 60 Hz.

is no longer accessible to us, we are not able to take advantage of the beads' streptavidin coating. We choose instead to essentially reverse the previous assay and coat the beads with PLL in order to nonspecifically attach them to the cell bodies.

We do so as follows (detailed protocol, as always, is provided in Appendix B): first, we mix 90μL of PLL with 5μL of bead solution. We allow the solution to sit for 1 minute. We then pellet the beads out by centrifiguation and suspend them in (non-sodium) motility buffer at a concentration of 100x to flow into the tunnel slide. Such a high dilution is chosen to prevent clumping of the beads due to their high nonspecifically reactive coating (see Figure 5.9). Despite this, beads are far more likely to aggregate in this protocol than in the standard bead assay (Figure 5.8(B), right panel); aggregation is further aggravated when beads are allowed to sediment within the Helmholtz coils (not shown). Regardless, this protocol provides us with 10-15 single (i.e., non-clumped) beads attached to tethered minicells per slide, which is sufficient for our measurements.

In a test of over 25 cells in the inverted cell assay thus far, we were able to rotate only 1 at a speed over 50 Hz and none over 100 Hz. While this maximum is similar to that for the PLL assay (Figure 5.10), we had attempted to measure over 100 cells with the PLL assay before obtaining this one successful trace. Further comparative measurements are required to
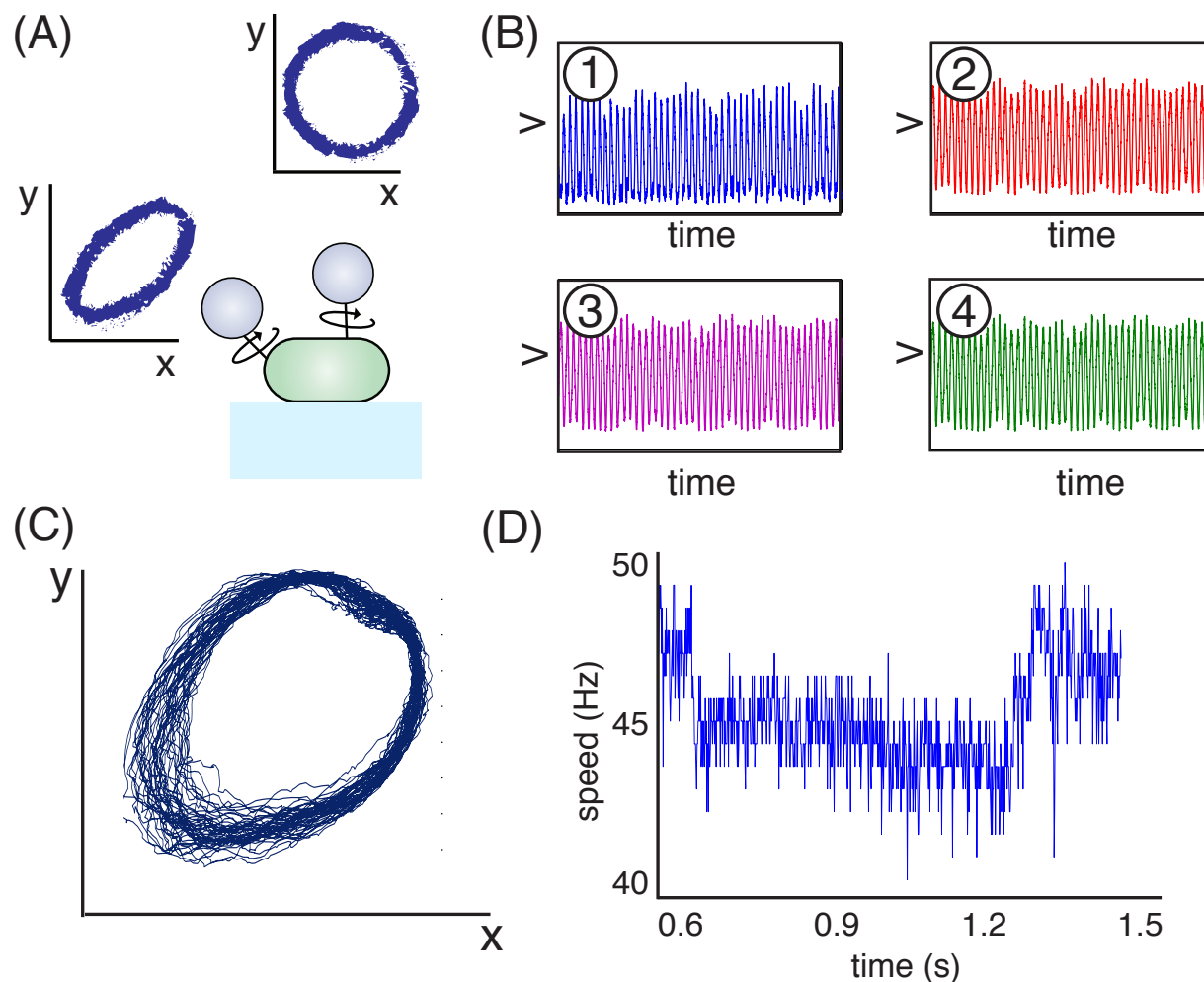
Figure 5.11: Conversion of photodiode signal into speed-time traces. **(A)** Schematic showing that the (x, y) projection of a bead's projection can be either circular or elliptical depending on the position of the hook on the cell body. **(B)** Voltage signal through each of the four quadrants of the QPD for a cell in 85 mM sodium solution. **(C)** Position of the bead attached to the cell in (x, y) space for 1 second, determined as in Equation (5.1). **(D)** A fast Fourier transform gives a speed-time trace.

definitively determine whether the various difficulties associated with the inverted cell assay (e.g., bead aggregation, lower yields of tethered cells) will be worthwhile for our purposes.

5.3 Analysis tools

In this section, we outline the tools developed in order to process and analyze the data collected as described above. We focus on two features in particular: (1) processing and

quantifying the fluorescence intensity from images taken using our setup; and (2) converting the (x, y) position data from the photodiode into high-resolution speed-time traces. As our focus has been primarily on experimental design and setup, we emphasize that the data presented in this chapter is preliminary. To this end, we note (as before) that while the general analysis pipeline is finalized, the details of the tools presented in this section are very likely to evolve as more data is collected and experimental protocols are further optimized.

Fluorescence image analysis

Under our previously described loading protocol, the fluorescence signal is 5 times the background. For analysis, each area around a fluorescent cell will be divided into three regions: background, marginal area, and cell area (see [71] for further details).

These regions are designated by their pixel intensities: the background pixel intensity is obtained using a threshold, T_{bg}, from the Gaussian function $g(I) = A_0 \exp\left[-(I - I_{bg})^2/2A_1^2\right]$. The values of the constants will be determined from fits to our final data. The background threshold is determined by choosing I_0, the smallest I for which $I > I_{peak}$ and $g(I) < 1$; $T_{bg} = I_0$. Likewise, the threshold for the cell $T_{cell} = (I_{max} + I_0)/2$. The marginal area is then the region for which $T_{bg} < I < T_{cell}$. By considering only the pixel intensity of the center of each cell, we ameliorate the effects of cell size: Smaller cells will have a relatively larger marginal area and a lower average intensity if the whole cell is considered. The average fluorescent intensity of a cell is then determined as:

$$F = \langle I - I_{bg} \rangle_{I > T_{cell}}, \tag{5.4}$$

where I_{bg} is the average intensity of the background.

Of course, several processes other than sodium flux can cause changes in average fluorescence. After entry into the cell, the dye is converted into its acidic fluorescent form, where an intracellular esterase then cleaves off the acetate domain. The negatively-charged acidic form has a low rate of passive leakage from the cell, and so continuing activation of dye during observation leads to increasing fluorescence. Decreasing fluorescence could be caused by leakage of dye out of cells, metabolic or other chemical degradation, or photobleaching.

In particular, photobleaching sets a limit to the number of successive measurements we can make on a single cell. With a typical illumination intensity of 7.35 W/cm^2, the bleaching time constant of Sodium Green, a similar fluorescent sodium indicator, was measured to be $\sim$50 seconds. As the newly-developed CoroNa Green is touted to be a improvement on this dye, we expect similar or better results at the same illumination [81]. Images with 1 second exposure at this intensity gave us fluorescence intensities 5 times greater than noise; therefore, we estimate $\sim$50 successive measurements can be made before photobleaching causes significant deterioration of the fluorescence signal. Values for internal sodium concentrations can then be calculated from these measurements (after calibration) as described in [71].
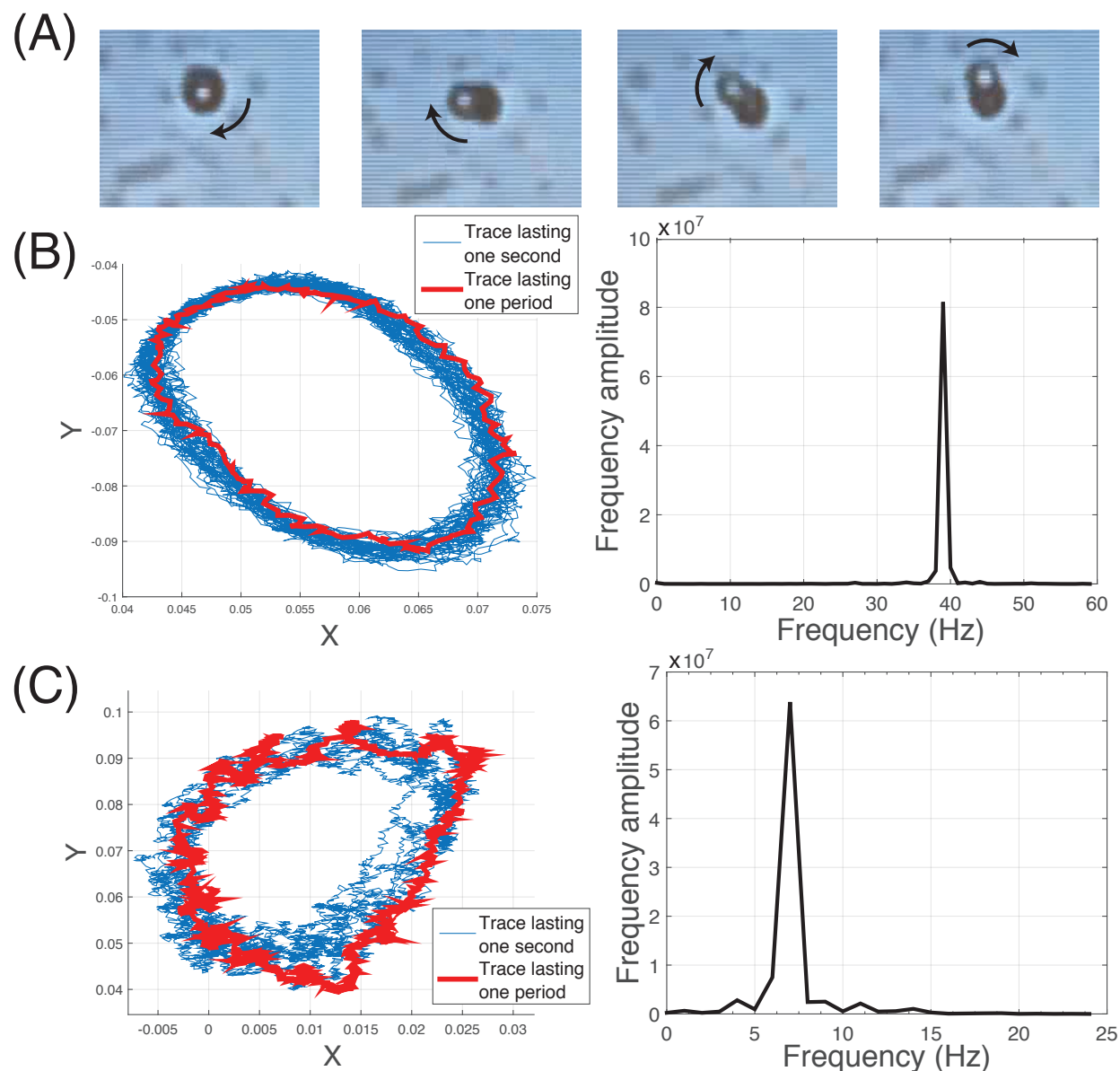
Figure 5.12: Analyzing example traces for PLL and inverted cell assays. **(A)** Frame grabs showing a PLL-coated bead spinning attached to a tethered cell (inverted cell assay). **(B)** and **(C)** Representative traces (left; an exemplary single revolution for each is highlighted in red) and peak extracted frequency (right) for the PLL and inverted cell assays, respectively. The inverted cell trace seems to convolute the motion of the bead and the tethered cell, resulting in a messier ellipse and broader peak in Fourier space.

Speed-time traces

The output current from each photodiode (as described in Section 5.1) is converted to a voltage, which are then read out by a LabVIEW program (Figure 5.11(B)). All subsequent analysis was performed in MATLAB. First, these signals are then converted to bead (x, y) position as described in Equation (5.1). Depending on the location of the motor on the cell body, the paths traced out by the beads are either circular or elliptical (usually at least somewhat elliptical; Figure 5.11(C)).

Ellipses were fit to the coordinates of the bead using a least-squares algorithm, from which the angular position of the bead was derived [45] (Figure 5.12(B) and (C)). This positional trace was considered in 1-second overlapping windows, spaced 0.05 seconds apart. The speed of the motor in each of these windows was determined by finding the maximum of the unfiltered power spectrum, which is given by the square of its time-Fourier transform (Figure 5.11(D)).

We note that traces for the inverted cell assay tend to be far messier and more difficult to resolve than for the PLL assay. This is likely because the connection between the bead and the cell body is not immune to "wobble", and the resulting ellipse is a convolution of the bead and cell motion (Figure 5.12(C)). As expected, traces worsen considerably when magnetic torque is applied, as the bead motion is exacerbated, sometimes becoming completely unresolvable (data not shown). This is another checkmark against the inverted cell assay, and will be taken into consideration in our final assay choice.

5.4 In conclusion

One of the purposes of any model is, or at least should be, to generate experimentally-testable predictions. The theoretical mechanism for torque-generation in the flagellar motor proposed in previous chapters makes several such predictions; in this chapter, we design and set up an experiment to directly test one of them.

For over 40 years, it has been believed that the flagellar motor operates by a **tightly-coupled** mechanism — that is, that each revolution of the motor is driven by a fixed number of ions across the membrane. Our model goes against this status quo, suggesting instead that each motor step may *not* be of equal size. However basic to the BFM's mechanism, this physiological property has yet to be directly measured or tested, likely due to the difficulty of measuring local proton flux / pH changes (as would be necessary in the wild-type *E. coli* motor). We circumvent this issue by proposing an experiment using a chimeric, sodium-driven motor which can be monitored using a sodium fluorescent indicator.

Even though the purpose of the experiment proposed here is simple — measure the relationship between ion flow across the membrane and motor rotation —, the setup has several components: This is because our goal requires the simultaneous measurement and control of several motor properties. Specifically, our setup includes components for fluorescence microscopy (to visualize changes in intracellular sodium concentration via a fluorescent indicator), magnetic tweezers (to vary torque and make measurements at various speeds in a

single cell), and an optical feedback trap (to monitor the speed of the motor we are manipulating and observing). While we have outlined here the construction of this setup and the generalized protocol for the experimental measurements, several improvements and details remain.

First, our method for coating beads with PLL and sticking them to cell bodies results in unusable large aggregates of beads, which is further aggravated by using Helmholtz coils to align the axis of the beads during settling. This might be improved in several ways, for example by further diluting the bead solution and flowing it through the tunnel slide more slowly, or by functionalizing the beads with a coating which will minimize non-specific binding (e.g., antibodies to the *E. coli* cell surface). Second, our protocol for applying magnetic torque to the motor can be systematically optimized; for instance, by varying the distance between the arms of the electromagnet or by testing beads from different manufacturers which may have stronger dipoles. Another improvement would involve upgrading our amplifier so that we would be able to pass more current through the coil. We leave these (and the ultimate answer to the question of loose vs. tight coupling in the flagellar motor) to future work.

Chapter 6

This is just to say: conclusions and future work

"I have done
the experiments
that were in
your lab book

and which
you were probably
saving
for your postdoc.

Forgive me
they were exciting
so sweet
and so cool."

— (Parody) William Carlos Williams, *This Is Just To Say*

The scientific aims of this thesis have been to (1) present an experimentally testable model for torque generation in the bacterial flagellar motor and (2) propose (and set up) the experiments to test various predictions made by our model. We hope that in focusing on and closely examining the fundamental mechanochemical cycle of this nanomachine, we have answered some questions and opened up many more about its structure, dynamic behavior, and interaction with its environment.

In particular, we put forward a mechanically-specific model to explain how the rotary motor of bacterial flagella generates torque in order to propel the swimming of these microorganisms. The localization of the motor to the bacterial inner cell membrane, combined with its large size, has made obtaining detailed information about motor structure very difficult. This dearth of experimental information has, in turn, made it difficult to generate models that pinpoint any specific physical mechanism as the driving force behind motor rotation.

We, with the work in this thesis, attempted to address this by carefully collating all the available experimental data and using this to put together as specific and detailed a model

as possible. We hope that this work emphasizes that one need not wait for full protein structures before proposing mechanistic models and using them to make specific predictions. Not knowing what something looks like (exactly, at least) does not make understanding how it works impossible — just a bit harder (and, accordingly, more fun to figure out!).

Importantly, each assumption and piece in the model proposed here is rooted in experiment. Our model implicates both electrostatic and steric forces as part of the flagellar motor's mechanochemical cycle (Chapter 3 and [76]). We propose that electrostatic forces play a non-vital role, positioning the torque-generating stator units in place to exert steric force on the rotor. This assertion arises from decades-old experimental results that found that mutations of charged residues on the stator and rotor reduces, but does not eliminate, motor function [133]. Furthermore, counter-mutations (e.g., a positive-to-negative mutation on the rotor to counteract a negative-to-positive mutation on the stator) often restored motor function fully, and sometimes even improved it.

The specificity of this model allowed us to make several experimentally-testable predictions. We followed up on two of these in this dissertation. One prediction of our fundamental model is explored in Chapter 4, and concerns the behavior of the motor in the low-load, high-speed regime. The prevailing opinion in the literature has been that there is a universal "limiting speed" for the flagellar motor. This was spurred on by experimental results reporting that low load motors showed only one speed jump when "resurrected" at low loads [112].

To explore the kinetically limited region, we extended our model to motors with multiple stators in Chapter 4 (and in [90]). Under the (natural) assumption that individual torque-generating units act independently, our model predicts the opposite of these results: Additional stator units, at both high and low loads, increase motor speed. While this contention with the status quo may seem concerning, another aim of this thesis is to emphasize the importance of never being married to one's theories, but rather being willing to constantly integrate new information and revise them as needed.

The resurrection result at low loads (among many others) has come under question with the recent discovery that the flagellar motor's structure adapts to its external environment — specifically, motors operating at high loads/low speeds contain a higher number of stator units than those at lower loads/higher speeds [68]. Given this, these results could be interpreted not as evidence of a limiting motor speed, but rather as support of the idea that motors at low load can only maintain one (or at most two) torque-generating units. We further support the predictions of our model through experimental results showing multiple speeds at low loads in chimeric, sodium-driven motors [90].

Another surprising prediction our model makes is that motor rotation is loosely coupled to ion flux — that is, each ion passage does not necessarily result in steps of equal sizes. This, like the lack of a universal, stator number-independent motor speed, goes against the majority of the current literature. Again, we make use of our access to sodium-driven motors to design an experiment to directly test this assertion. In Chapter 5, we described our setup using a sodium fluorescent dye to directly measure sodium flux in motors whose speeds we are able to control using magnetic tweezers. As noted in the previous chapter, many aspects

of this setup and protocol can still be improved: For instance, magnetic control may be made stronger by using beads with higher magnetization or by passing a higher current through the electromagnet tweezers.

Of course, in addition to these two predictions, many more remain to be pursued (we hope our belief that good models not only answer questions, but generate new ones as well has shone through in this dissertation). For one such example, recall that one of the reasons our modeling efforts are particularly timely is the result regarding the motor's adaptation in response to external conditions. Beyond this observation, however, it remains unknown how motors experiencing high external forces recruit and maintain more stators than those at lower loads. Even the basic question of whether the motor is a direct mechanosensor (i.e., stator recruitment is load-dependent) or if stator recruitment is indirectly managed via motor speed remains to be tested directly. The primary difficulty in this measurement lies in uncoupling the effects of load and speed. However, similar to our experimental setup for measuring ion flux, we once again can make use of our access to sodium-driven chimeric motors to test how stator recruitment rate changes as the external sodium concentration (and thus speed) is varied at constant load (bead size).

Other predictions include: each motor step is composed of two half-steps; the two pairs of MotA loops in the stator work to generate torque in the CCW and CW directions; and motor switching operates via flipping of FliG proteins acting via nearest-neighbor interactions (i.e., according to an Ising model), among others. We hope that these will be addressed further eventually (preferably soon), but are out of the scope of the work contained in this thesis.

Beyond the (many, exciting) questions that remain regarding the dynamics of the motor itself, the BFM also sits at an interesting crossroads: There are also several (quite different!) research directions that arise naturally from its study. In addition to its obvious and fundamental role in the motility of flagellated bacteria, questions stemming from the behavior of the flagellar motor have important implications for several other fundamental biological processes, including other bacterial machinery such as that for gliding motility in *Myxococcus* [122], biofilm formation and the liquid-to-surface living transition [118], information processing in chemotaxis [85], and the dynamics of other molecular motors, including the closely-related F_O motor of ATP synthase [57, 28]. And this is to name only a few! So, with this, our final hope (of the many we have already, ambitiously, stated) is that the work in this dissertation will both lay down some groundwork and inspire passion for further study of exciting scientific questions in many diverse areas of research.

Appendix A

An overview of steric forces

In this section, we describe our modeling of the steric forces between the stator and the rotor, as well as a general discussion on the nature of contact/steric forces in a low Reynolds number environment. The behavior of objects moving at low Reynolds number is counterintuitive. When the Reynolds number is small, viscous forces dominate over inertial forces and inertia can be ignored [101]. In the following, we illustrate some of these properties using a simple linear momentum balance. We can then extend this analysis to angular momentum balances, which are directly relevant to the BFM.

Consider a force F pushing an object A which is in contact with a larger object, B. We denote the drag coefficients on objects A and B as ζ_A and ζ_B, respectively. Let us consider the following two situations.

Case 1: if F is applied to A, how much force is transferred to B when they are in contact? In the steady state, the force balances can be written as:

$$F - F_c - \zeta_A v_A = 0$$
$$F_c - \zeta_B v_B = 0 \ . \tag{A.1}$$

In Equation (A.1), v_A and v_B are the velocities of objects A and B, respectively, and F_c is the contact force between objects A and B. When the two objects are in contact and are moving together, the following "contact condition" ensures that the velocity of the objects are equal:

$$v_A = v_B. \tag{A.2}$$

In this case, the force transferred by A to B (the contact force, F_c), is obtained by solving (A.1):

$$F_c := \frac{F}{1 + \zeta_A/\zeta_B}. \tag{A.3}$$

When the drag on B is large, *i.e.*, $\zeta_A/\zeta_B \ll 1$, almost all of the force F is transferred to the object B. Conversely, when $\zeta_A/\zeta_B \gg 1$, then most of the force is consumed to drag object A with little force transferred to object B.

Case 2: when there are N objects of type A in contact with B, each with a force F applied to them. As in the first case, we are concerned with how much of F is transferred to B. Again, using free-body diagrams, we can write the equations of motion for the objects as

$$F - F_c^i - \zeta_A v_A^i = 0, \quad i \in \{1, \dots, N\},$$

$$\sum_{i=1}^{N} F_c^i - \zeta_B v_B = 0, \tag{A.4}$$

where F_c^i is the contact force between the ith object of type A and object B. As before, when the objects are in contact, the contact condition ensures that $v_A^i = v_B$ for all i. Therefore, the force transferred to B by N objects of type A can be derived from (A.4) as

$$F_c = \sum_{i=1}^{N} F_c^i = \frac{NF}{1 + N\zeta_A/\zeta_B}. \tag{A.5}$$

When $\zeta_A/\zeta_B \ll 1/N$, then $F_c \approx NF$. Therefore, the force transferred to B is multiplied by the number of objects pushing B. However, when $\zeta_A/\zeta_B \gg 1/N$, then the force transferred is $F_c \approx F/(\zeta_A/\zeta_B) \approx 0$. Finally, when $\zeta_A/\zeta_B \approx 1$ (and N is sufficiently large), then the force transferred is $F_c \approx F$ (i.e., the force transferred in this system is approximately the same as a single object A pushing B).

The above properties of contact forces can be applied to the BFM by identifying object A as the stator and B as the rotor-load system (i.e., the rotor and the bead), and F as the internal force generated by the proline hinge pushing the stator from its straight to bent state.

For large loads (e.g., large beads), almost all of the force generated by the stator is transferred to the rotor; i.e., the torque is close to stall. Moreover, as more stators are recruited, the transferred force increases linearly with the number of active stators, in accordance with the observed linear speed dependence on the number of stators near stall torque. By contrast, at zero load, if there exists a situation where the stator and rotor drags are comparable, then the above analysis suggests that the transferred force during a single step is equivalent to a single stator pushing the rotor. This suggests that, if the assumption that stators step in synchrony holds, torque and speed at low loads may be independent of the number of active stators.

In addition to the above, contact forces also have the following important implications for the BFM:

1. Because it operates at low Reynolds number, the rotor moves only as long as it is pushed by the stator. This assures that the rotor never moves faster than the stator.

2. Experiments based on torque-speed curves alone may never be able to detect the number of operating stators at different loads (e.g., if both torque and speed are independent of the number of stators at low load). Rather, one likely needs chemical markers, such

as the GFP tags as used in [117], to identify the number of docked and engaged stators for a given load.

3. The torque generated by the BFM depends on the bead size and is not constant across applied loads, as it was considered to be by previous models [123, 80, 79].

Interestingly, the speed of the BFM has been shown to be slightly nonlinearly dependent on the number of stators at high loads. A linear relationship between speed and stator number would imply (1) that the applied force of the stator is independent of the load and (2) that all stators act independently. Our results suggest that this nonlinearity may arise as a natural consequence of the steric force in (at least partially) coupled stators. Further experiments will be needed to further explore this hypothesis.

Appendix B

Full experimental protocols

Cell growth

We specifically refer to the protocol for the MTB24 minicell strain used in this thesis; however, this can be generalized to many bacterial strains (just substitute in the appropriate inducers and antibiotics, if necessary!).

1. Make a solution of 25μM chloramphenicol (to preserve plasmids) and 50μM IPTG (to induce plasmids) in tryptone broth (TB, 1% BD bacto tryptone, 85mM sodium chloride) in an Erlenmeyer flask.

2. Add 20-100μL of cells to the solution.

3. Place flask in incubator at 30°C for 16-17 hours, shaking at 150rpm; make sure lid is only partially screwed on to prevent anaerobic conditions. [**Note:** For non-minicell strains, growth time will likely be lower.]

4. Upon removal, check OD_{600}; ideally, it should be between 1.5-1.8. [**Note:** For non-minicell strains, ideal OD_{600} will likely be lower.]

5. Use immediately!

Cell preparation

This preparation corresponds to the sodium-driven chimeric strain; for *E. coli* strains with wild-type motors, a similar protocol will hold if a non-sodium motility buffer is used.

1. Spin cells in a centrifuge for 2 minutes at 3000g. There should be a visible pellet (how large this pellet is will depend on the OD of the solution). [**Note:** If you are working with the non-minicell MTB24 strain, skip ahead and go to the penultimate step!]

2. Dispose pellet and spin supernatant for 25 minutes at 3000g. The initial pellet contains the large cells of MTB24, whereas the second, longer spin will separate out the smaller, lighter minicells. [**Note:** The minicell pellet will be far smaller than the original pellet; for smaller initial volumes, it may even be undetectable – don't worry!]

3. Carefully remove the supernatant and resuspend the pellet in sodium motility buffer (MB, 10mM potassium phosphate, 0.1mM EDTA, 85mM NaCL, pH 7.0).

4. Repeat this washing 1-2x, as desired. [**Note:** You may want to avoid multiple washings if your pellet is very small, as more cells are inevitably lost in each wash.] The final suspension should be 5-20x concentrated depending on pellet size (e.g., if 1mL of cell solution is used initially, resuspend final pellet in 50-200μL of MB).

Bead preparation

This bead preparation focuses on functionalizing beads with a poly-L-lysine coating for non-specific binding, but removing a few steps leaves behind a protocol for use of these beads in the standard bead assay.

1. Mix 5μL of beads in solution (we use Dynabeads MyOne Streptavidin C1) with 90μL of poly-L-lysine (0.01% solution) in an Eppendorf tube. [**Note:** If doing the standard bead assay, skip this step.]

2. Spin bead solution in a centrifuge for 30 seconds at 3000g. Carefully remove all the supernatant and resuspend in deionized water or in MB.

3. Repeat this washing 1-2x, as desired. The final suspension should be a 50-100x dilution (e.g., if you had 5μL of beads to start with, the final suspension should be 250-500μL). [**Note:** If doing the standard bead assay, the final suspension should be a 20-50x dilution.]

Tunnel slide preparation

Standard tunnel slide preparation; this should be generalizable to many assays, including all those discussed in this thesis.

1. Take one small and one large coverslip (we use 22x22mm and 22x40mm, respectively).

2. Put two strips of double-tape along the length of the larger coverslip and place the smaller coverslip on top (see Figure 5.8).

3. Use a razor to cut off the excess tape.

4. Use an Eppendorf tube (or similar) to press down the top coverslip and remove any bubbles.

Poly-L-lysine slide bead assay

This is one of two bead assays we outline in this thesis. This protocol is for minicells, but can be generalized with some slight changes (we note these throughout).

1. Prepare tunnel slide (see previous protocol).

2. Flow through MB to wet (always tissue through all fluid for speed; if more patient, gravity is fine).

3. Flow through 50μL of 0.01% poly-L-lysine and incubate for 5 minutes.

4. Rinse the tunnel slide with 50μL sodium MB (twice if desired).

5. Add 30-50μL of cell suspension and incubate for 15-20 minutes in a humidity chamber (we use a small box with a wet tissue in it). Make sure to incubate with the same surface down as in the PLL step. [**Note:** If working with normal-sized cells, incubate for 5 minutes.]

6. Rinse the tunnel slide with 50μL sodium MB (twice if desired) to remove unstuck cells.

7. Flow through 30-50μL of streptavidin-coated bead solution and incubate in the humidity chamber for 10 minutes. Once again, remember to incubate with the same side down. [**Note:** This type of bead is specific to the strain we are using, which has a biotinylated hook to bind nicely to streptavidin-coated beads. But the procedure is general.]

Avidin slide bead assay

This is the other of two bead assays we outline in this thesis. This protocol, like the previous one, is for minicells, but can be generalized with some slight changes (we note these throughout).

1. Prepare tunnel slide (see previous protocol), but do not trim the excess double sided tape.

2. Flow through MB to wet (always tissue through all fluid for speed; if more patient, gravity is fine).

3. Flow through 50μL biotin-BSA mixture and incubate for 20 minutes in a humidity chamber.

4. Rinse the tunnel slide with 50μL sodium MB (twice if desired).

5. Flow through 50μL streptavidin or neutravidin (1mg/mL in MB) and incubate for 20 minutes in a humidity chamber. Make sure to incubate with the same surface down as in the biotin-BSA step (we recommend with the coverslip down for the sake of step 7).

6. Rinse the tunnel slide with 50μL sodium MB (twice if desired).

7. Add 30-50μL of cell suspension. Place slide in a centrifuge and spin (with same side down as in the biotin and avidin steps) for 5-10 minutes at 5-10g. The excess double sided tape will serve to hold the slide in place within the centrifuge bucket. [**Note:** If working with normal-sized cells, simply incubate as in the PLL protocol for 15-20 minutes.]

8. Remove slide from centrifuge and wash through with MB (twice if desired).

9. Flow through 20μL of dilute PLL-coated beads (see bead preparation preparation protocol) and incubate for 10-15 minutes in the humidity chamber. Repeat as needed, until desired yield of spinners is obtained. Remember to wash out with MB in between each repetition to prevent bead clumping!

Loading with fluorescent dye

This protocol outlines the procedure on loading *E. coli* minicells with the fluorescent sodium indicator CoroNa. Similar protocols likely will work for other bacterial strains and dyes.

1. After cell preparation, mix the final pellet in 200μL of loading buffer (10mM EDTA, 10mM sodium phosphate) and 4μL prepared CoroNa stock solution (2mM CoroNa in DMSO). [**Note**: Depending on pellet size, you may want to add more or less loading buffer; this is fine, but just make sure the CoroNa is at 40μM in the final solution.]

2. Incubate the Eppendorf tube at 37°C for 30 minutes.

3. Spin cells in a centrifuge for 25 minutes at 3000g. [**Note**: The pellet may be smaller than you remember! This is likely due to the damage caused to some cells by the harsh loading buffer. Do not spin further to increase pellet size — this will just lead to cell fragments being included in your final solution.]

4. Resuspend the pellet in sodium motility buffer. Repeat this washing 1-2x, as desired. As before, the final concentration should be 50-200x dilution.

Bibliography

[1] Dinah Abram, Henry Koffler, and A. E. Vatter. "Basal structure and attachment of flagella in cells of Proteus vulgaris." In: *Journal of Bacteriology* 90.5 (1965), pp. 1337–1354.

[2] HI Adler et al. "Miniature Escherichia coli cells deficient in DNA". In: *Proceedings of the National Academy of Sciences* 57.2 (1967), pp. 321–326.

[3] David E Alexander and Steven Vogel. *Nature's flyers: birds, insects, and the biomechanics of flight*. JHU Press, 2004.

[4] R McNeill Alexander. *Principles of animal locomotion*. Princeton University Press, 2003.

[5] U Alexiev et al. "Rapid long-range proton diffusion along the surface of the purple membrane and delayed proton transfer into the bulk." In: *Proceedings of the National Academy of Sciences* 92.2 (1995), pp. 372–376.

[6] Yukako Asai et al. "Ion-coupling Determinants of Na+-driven and H+-driven Flagellar Motors". In: *Journal of Molecular Biology* 327.2 (2003), pp. 453–463.

[7] Fan Bai et al. "Coupling between switching regulation and torque generation in bacterial flagellar motor". In: *Physical Review Letters* 108.17 (2012), p. 178105.

[8] Fan Bai et al. "Model studies of the dynamics of bacterial flagellar motors". In: *Biophysical Journal* 96.8 (2009), pp. 3154–3167.

[9] Victor Barcilon. "Ion flow through narrow membrane channels: Part I". In: *SIAM Journal on Applied Mathematics* 52.5 (1992), pp. 1391–1404.

[10] H. C. Berg. "The rotary motor of bacterial flagella". In: *Annual Review of Biochemistry* 72 (2003), pp. 19–54.

[11] Howard C. Berg and Robert A. Anderson. "Bacteria swim by rotating their flagellar filaments". In: *Nature* 245.5425 (1973), pp. 380–382.

[12] Howard C. Berg and Linda Turner. "Torque Generated by the Flagellar Motor of Escherichia coil". In: *Biophysical Journal* 65.5 (1993), pp. 2201–2216.

[13] Richard M Berry. "Torque and switching in the bacterial flagellar motor. An electrostatic model." In: *Biophysical Journal* 64.4 (1993), p. 961.

[14]   Richard M Berry and Howard C Berg. "Absence of a barrier to backwards rotation of the bacterial flagellar motor demonstrated with optical tweezers". In: *Proceedings of the National Academy of Sciences* 94.26 (1997), pp. 14433–14437.

[15]   Richard M. Berry, Linda Turner, and Howard C. Berg. "Mechanical limits of bacterial flagellar motors probed by electrorotation." In: *Biophysical Journal* 69.1 (1995), p. 280.

[16]   David F. Blair and Howard C. Berg. "Restoration of torque in defective flagellar motors". In: *Science* 242.4886 (1988), pp. 1678–1681.

[17]   Richard W Blob and Timothy E Higham. "Terrestrial locomotion: where do we stand, where are we going? An introduction to the symposium". In: *Integrative and Comparative Biology* (2014), pp. 1051–1057.

[18]   Steven M. Block and Howard C. Berg. "Successive incorporation of force-generating units in the bacterial rotary motor". In: *Nature* 309 (1984), pp. 470–472.

[19]   Steven M Block, David F Blair, and Howard C Berg. "Compliance of bacterial flagella measured with optical tweezers". In: *Nature* 338 (1989), pp. 514–518.

[20]   Steven M Block, David F Blair, and Howard C Berg. "Compliance of bacterial polyhooks measured with optical tweezers". In: *Cytometry* 12.6 (1991), pp. 492–496.

[21]   Ryan Boschert, Frederick R Adler, and David F Blair. "Loose coupling in the bacterial flagellar motor". In: *Proceedings of the National Academy of Sciences* (2015), pp. 4755–4760.

[22]   Richard W. Branch et al. "Adaptive Remodelling by FliN in the Bacterial Rotary Motor". In: *Journal of Molecular Biology* 426.19 (2014), pp. 3314–3324.

[23]   Timothy F Braun et al. "Arrangement of core membrane segments in the MotA/MotB proton-channel complex of Escherichia coli". In: *Biochemistry* 43.1 (2004), pp. 35–45.

[24]   Timothy F. Braun et al. "Function of proline residues of MotA in torque generation by the flagellar motor of Escherichia coli". In: *Journal of Bacteriology* 181.11 (1999), pp. 3542–3551.

[25]   Mostyn T Brown et al. "Flagellar hook flexibility is essential for bundle formation in swimming Escherichia coli cells". In: *Journal of Bacteriology* 194.13 (2012), pp. 3495–3501.

[26]   Perry N Brown, Christopher P Hill, and David F Blair. "Crystal structure of the middle and C-terminal domains of the flagellar rotor protein FliG". In: *The EMBO Journal* 21.13 (2002), pp. 3225–3234.

[27]   Wesley R Browne, Andrew Woolley, and Dahui Hu. "Molecular Machines". In: *Chemical Physical Chemistry* 17.12 (2016), pp. 1713–1714.

[28]   Carlos Bustamante, David Keller, and George Oster. "The physics of molecular motors". In: *Accounts of Chemical Research* 34.6 (2001), pp. 412–420.

[29] Xiaobing Chen and Howard C Berg. "Torque-speed relationship of the flagellar rotary motor of Escherichia coli". In: *Biophysical Journal* 78.2 (2000), pp. 1036–1041.

[30] Germaine Cohen-Bazire and Jack London. "Basal Organelles of Bacterial Flagella". In: *Journal of Bacteriology* 94.2 (1967), pp. 458–465.

[31] F. S. Cordes, J. N. Bright, and M. S. P. Sansom. "Proline-induced Distortions of Transmembrane Helices". In: *Journal of Molecular Biology* 323 (2002), pp. 951–960.

[32] T Daniel, C Jordan, and D Grunbaum. "Hydromechanics of swimming". In: *Advances in Comparative and Environmental Physiology* 11 (1992), pp. 17–49.

[33] Kirill A Datsenko and Barry L Wanner. "One-step inactivation of chromosomal genes in Escherichia coli K-12 using PCR products". In: *Proceedings of the National Academy of Sciences* 97.12 (2000), pp. 6640–6645.

[34] Nicolas J. Delalez, Richard M. Berry, and Judith P. Armitage. "Stoichiometry and Turnover of the Bacterial Flagellar Switch Protein FliN". In: *mBio* 5.4 (2014), e01216–14.

[35] Nicolas J. Delalez et al. "Signal-dependent turnover of the bacterial flagellar switch protein FliM". In: *Proceedings of the National Academy of Sciences USA USA* 107.25 (2010), pp. 11347–11351.

[36] M. L. DePamphilis and Julius Adler. "Attachment of Flagellar Basal Bodies to the Cell Envelope: Specific Attachment to the Outer, Lipopolysaccharide Membrane and the Cytoplasmic Membrane". In: *Journal of Bacteriology* 105.1 (1971), pp. 396–407.

[37] M. L. DePamphilis and Julius Adler. "Fine structure and isolation of the hook-basal body complex of flagella from Escherichia coli and Bacillus subtilis". In: *Journal of Bacteriology* 105.1 (1971), pp. 384–395.

[38] M. L. DePamphilis and Julius Adler. "Purification of Intact Flagella from Escherichia coli and Bacillus subtilis". In: *Journal of Bacteriology* 105.1 (1971), pp. 376–383.

[39] K. Dimmitt and M. Simon. "Purification and Thermal Stability of Intact Bacillus subtilis Flagella". In: *Journal of Bacteriology* 105.1 (1971), pp. 369–375.

[40] T. A. J. Duke, N. Le Novére, and D. Bray. "Conformational Spread in a Ring of Proteins: A Stochastic Approach to Allostery". In: *Journal of Molecular Biology* 308.3 (2001), pp. 541–553.

[41] R Edgeworth, BJ Dalton, and T Parnell. "The pitch drop experiment". In: *European Journal of Physics* 5.4 (1984), p. 198.

[42] Timothy C. Elston and George Oster. "Protein turbines. I: The bacterial flagellar motor." In: *Biophysical Journal* 73.2 (1997), pp. 703–721.

[43] Gregory Falkovich. *Fluid mechanics: A short course for physicists*. Cambridge University Press, 2011.

[44] Edward H Feng and Gavin E Crooks. "Length of time's arrow". In: *Physical Review Letters* 101.9 (2008), p. 090602.

[45] Andrew Fitzgibbon, Maurizio Pilu, and Robert B Fisher. "Direct least square fitting of ellipses". In: *IEEE Transactions on Pattern Analysis and Machine Intelligence* 21.5 (1999), pp. 476–480.

[46] Scott Forth et al. "Torque measurement at the single-molecule level". In: *Annual Review of Biophysics* 42 (2013), pp. 583–604.

[47] Noreen R. Francis et al. "Isolation, characterization and structure of bacterial flagellar motors containing the switch complex". In: *Journal of Molecular Biology* 235.4 (1994), pp. 1261–1270.

[48] Anne Cornish Frazer and Roy Curtiss. "Production, properties and utility of bacterial minicells." In: *Current Topics in Microbiology and Immunology* 69 (1975), pp. 1–84.

[49] David C Fung and Howard C Berg. "Powering the flagellar motor of Escherichia coli with an external voltage source". In: *Nature* 375.6534 (1995), pp. 809–812.

[50] L Gardini, FS Pavone, and M Capitanio. "Single molecule study of processive myosin motors". In: *Photonic Technologies (Fotonica 2016), 18th Italian National Conference on*. IET. 2016, pp. 1–4.

[51] Frederick Gittes and Christoph F Schmidt. "Interference model for back-focal-plane displacement detection in optical tweezers". In: *Optics Letters* 23.1 (1998), pp. 7–9.

[52] A.N. Glagolev and V.P. Skulachev. "The proton pump is a molecular engine of motile bacteria". In: *Nature* 272 (1978), pp. 280–282.

[53] James Gray. *Animal locomotion*. Norton New York, 1968.

[54] Peter M Hoffmann. "How molecular motors extract order from chaos (a key issues review)". In: *Reports on Progress in Physics* 79.3 (2016), p. 032601.

[55] Yuichi Inoue et al. "Torque–speed relationships of Na+-driven chimeric flagellar motors in Escherichia coli". In: *Journal of Molecular Biology* 376.5 (2008), pp. 1251–1259.

[56] Xander JA Janssen et al. "Electromagnetic torque tweezers: a versatile approach for measurement of single-molecule twist and torque". In: *Nanoletters* 12.7 (2012), pp. 3634–3639.

[57] Wolfgang Junge. "ATP synthase and other motor proteins". In: *Proceedings of the National Academy of Sciences* 96.9 (1999), pp. 4735–4737.

[58] E. A. Kim et al. "Membrane Segment Organization in the Stator Complex of the Flagellar Motor: Implications for Proton Flow and Proton-Induced Conformational Change". In: *Biochemistry* 47 (2008), pp. 11332–11339.

[59] Daniel Klaue and Ralf Seidel. "Torsional stiffness of single superparamagnetic microspheres in an external magnetic field". In: *Physical Review Letters* 102.2 (2009), p. 028302.

[60] Seiji Kojima and David F Blair. "Conformational change in the stator of the bacterial flagellar motor". In: *Biochemistry* 40.43 (2001), pp. 13041–13050.

[61] Anatoly B Kolomeisky and Michael E Fisher. "Molecular motors: a theorist's perspective". In: *Annual Review of Physical Chemistry* 58 (2007), pp. 675–695.

[62] Goro Kuwajima. "Construction of a Minimum-size Functional Flagellin of Escherichia coli". In: *Journal of Bacteriology* 170 (1988), pp. 3305–3309.

[63] Goro Kuwajima. "Flagellin domain that affects H antigenicity of Escherichia coli K-12." In: *Journal of Bacteriology* 170.1 (1988), pp. 485–488.

[64] P Läuger. "Torque and rotation rate of the bacterial flagellar motor." In: *Biophysical Journal* 53.1 (1988), pp. 53–65.

[65] Mark C Leake et al. "Stoichiometry and turnover in single, functioning membrane protein complexes". In: *Nature* 443.7109 (2006), pp. 355–358.

[66] L. K. Lee et al. "Structure of the torque ring of the flagellar motor and the molecular basis for rotational switching". In: *Nature* 466.7309 (2010), pp. 996–1000.

[67] Einar Leifson et al. *Atlas of bacterial flagellation.* New York & London, Academic Press., 1960.

[68] Pushkar P Lele, Basarab G Hosu, and Howard C Berg. "Dynamics of mechanosensing in the bacterial flagellar motor". In: *Proceedings of the National Academy of Sciences USA* 110.29 (2013), pp. 11839–11844.

[69] Ren Chong Lim. "Application of External Torque on the Bacterial Flagellar Motor". PhD thesis. University of Oxford, 2015.

[70] Jan Lipfert et al. "Magnetic torque tweezers: measuring torsional stiffness in DNA and RecA-DNA filaments". In: *Nature Methods* 7.12 (2010), pp. 977–980.

[71] Chien-Jung Lo, Mark C. Leake, and Richard M. Berry. "Fluorescence measurement of intracellular sodium concentration in single Escherichia coli cells". In: *Biophysical Journal* 90.1 (2006), pp. 357–365.

[72] Chien-Jung Lo et al. "Mechanism and kinetics of a sodium-driven bacterial flagellar motor". In: *Proceedings of the National Academy of Sciences USA* 110.28 (2013), E2544–E2551.

[73] Chien-Jung Lo et al. "Nonequivalence of Membrane Voltage and Ion-Gradient as Driving Forces for the Bacterial Flagellar Motor at Low Load". In: *Biophysical Journal* 93.1 (2007), pp. 294–302.

[74] Graeme Lowe, Markus Meister, and Howard C. Berg. "Rapid rotation of flagellar bundles in swimming bacteria". In: *Nature* 325.12 (1987), pp. 637–640.

[75] DG Luchinsky et al. "Ion channels as electrostatic amplifiers of charge fluctuations". In: *Journal of Physics: Conference Series.* Vol. 142. 1. IOP Publishing. 2008, p. 012049.

[76] Kranthi K Mandadapu et al. "Mechanics of torque generation in the bacterial flagellar motor". In: *Proceedings of the National Academy of Sciences* 112.32 (2015), E4381–E4389.

[77] Michael D. Manson et al. "A protonmotive force drives bacterial flagella". In: *Proceedings of the National Academy of Sciences USA* 74.7 (1977), pp. 3060–3064.

[78] Shusuke Matsuura, Jun-ichi Shioi, and Yasuo Imae. "Motility in Bacillus subtilis driven by an artificial protonmotive force." In: *FEBS Letters* 82.2 (1977), pp. 187–190.

[79] Giovanni Meacci, Ganhui Lan, and Yuhai Tu. "Dynamics of the bacterial flagellar motor: The effects of stator compliance, back steps, temperature, and rotational asymmetry". In: *Biophysical Journal* 100.8 (2011), pp. 1986–1995.

[80] Giovanni Meacci and Yuhai Tu. "Dynamics of the bacterial flagellar motor with multiple stators". In: *Proceedings of the National Academy of Sciences USA* 106.10 (2009), pp. 3746–3751.

[81] Silke D Meier, Yury Kovalchuk, and Christine R Rose. "Properties of the new fluorescent Na+ indicator CoroNa Green: comparison with SBFI and confocal Na+ imaging". In: *Journal of Neuroscience Methods* 155.2 (2006), pp. 251–259.

[82] M. Meister and H. C. Berg. "The stall torque of the bacterial flagellar motor." In: *Biophysical Journal* 52.3 (1987), pp. 413–419.

[83] Markus Meister, S Roy Caplan, and H.C. Berg. "Dynamics of a tightly coupled mechanism for flagellar rotation. Bacterial motility, chemiosmotic coupling, protonmotive force." In: *Biophysical Journal* 55.5 (1989), p. 905.

[84] Markus Meister, Graeme Lowe, and Howard C. Berg. "The proton flux through the bacterial flagellar motor". In: *Cell* 49.5 (1987), pp. 643–650.

[85] Gabriele Micali and Robert G Endres. "Bacterial chemotaxis: information processing, thermodynamics, and behavior". In: *Current Opinion in Microbiology* 30 (2016), pp. 8–15.

[86] Thierry Mora, Howard Yu, and Ned S Wingreen. "Modeling torque versus speed, shot noise, and rotational diffusion of the bacterial flagellar motor". In: *Physical Review Letters* 103.24 (2009), p. 248102.

[87] Thierry Mora et al. "Steps in the bacterial flagellar motor". In: *PLoS Computational Biology* 5.10 (2009), E1000540.

[88] Francesco Mosconi, Jean François Allemand, and Vincent Croquette. "Soft magnetic tweezers: A proof of principle". In: *Review of Scientific Instruments* 82.3 (2011), p. 034302.

[89] Shuichi Nakamura et al. "Evidence for symmetry in the elementary process of bidirectional torque generation by the bacterial flagellar motor". In: *Proceedings of the National Academy of Sciences* 107.41 (2010), pp. 17616–17620.

[90] Jasmine A Nirody, Richard M Berry, and George Oster. "The limiting speed of the bacterial flagellar motor". In: *Biophysical Journal* 111.3 (2016), pp. 557–564.

[91] Jasmine A Nirody, Yi-Ren Sun, and Chien-Jung Lo. "The biophysicist's guide to the bacterial flagellar motor". In: *Advances in Physics: X* 2.2 (2017), pp. 324–343.

[92] Yasutaka Nishihara and Akio Kitao. "Gate-controlled proton diffusion and protonation-induced ratchet motion in the stator of the bacterial flagellar motor". In: *Proceedings of the National Academy of Sciences* 112.25 (2015), pp. 7737–7742.

[93] Masayoshi Nishiyama, Hideo Higuchi, and Toshio Yanagida. "Chemomechanical coupling of the forward and backward steps of single kinesin molecules". In: *Nature Cell Biology* 4.10 (2002), pp. 790–797.

[94] Davide Normanno, Marco Capitanio, and Francesco Saverio Pavone. "Spin absorption, windmill, and magneto-optic effects in optical angular momentum transfer". In: *Physical Review A* 70.5 (2004), p. 053829.

[95] Fumio Oosawa and Shigeru Hayashi. "Coupling between flagellar motor rotation and proton flux in bacteria". In: *Journal of the Physical Society of Japan* 52.11 (1983), pp. 4019–4028.

[96] Fumio Oosawa and Shigeru Hayashi. "The loose coupling mechanism in molecular machines of living cells". In: *Advances in Biophysics* 22 (1986), pp. 151–183.

[97] Fumio Oosawa and Junji Masai. "Mechanism of flagellar motor rotation in bacteria". In: *Journal of the Physical Society of Japan* 51.2 (1982), pp. 631–641.

[98] K. Paul et al. "A molecular mechanism of direction switching in the flagellar motor of Escherichia coli". In: *Proceedings of the National Academy of Sciences* 108.41 (2011), pp. 17171–17176.

[99] Koushik Paul et al. "Architecture of the flagellar rotor". In: *The EMBO Journal* 30.14 (2011), pp. 2962–2971.

[100] Steven L Porter, George H Wadhams, and Judith P Armitage. "Signal processing in complex chemotaxis pathways". In: *Nature Reviews Microbiology* 9.3 (2011), pp. 153–165.

[101] Edward M Purcell. "Life at low Reynolds number". In: *American Journal of Physics* 45.1 (1977), pp. 3–11.

[102] B Selva Rani and Ch Aswani Kumar. "A Comprehensive Review on Bacteria Foraging Optimization Technique". In: *Multi-objective Swarm Intelligence*. Springer, 2015, pp. 1–25.

[103] Stuart W. Reid et al. "The maximum number of torque-generating units in the flagellar motor of Escherichia coli is at least 11". In: *Proceedings of the National Academy of Sciences USA* 103.21 (2006), pp. 8066–8071.

[104] Alex D Rowe. "Rotation of the sodium driven bacterial flagellar motor." PhD thesis. University of Oxford, 2005.

[105] William S Ryu, Richard M Berry, and Howard C Berg. "Torque-generating units of the flagellar motor of Escherichia coli have a high duty ratio". In: *Nature* 403.6768 (2000), pp. 444–447.

[106] AD Samuel and Howard C Berg. "Fluctuation analysis of rotational speeds of the bacterial flagellar motor." In: *Proceedings of the National Academy of Sciences* 92.8 (1995), pp. 3502–3506.

[107] AD Samuel and Howard C Berg. "Torque-generating units of the bacterial flagellar motor step independently." In: *Biophysical Journal* 71.2 (1996), p. 918.

[108] Birgit E Scharf et al. "Control of direction of flagellar rotation in bacterial chemotaxis". In: *Proceedings of the National Academy of Sciences* 95.1 (1998), pp. 201–206.

[109] Michael Silverman, Philip Matsumura, and Melvin Simon. "The identification of the mot gene product with Escherichia coli-lambda hybrids". In: *Proceedings of the National Academy of Sciences USA* 73.9 (1976), pp. 3126–3130.

[110] Michael Silverman and Melvin Simon. "Flagellar rotation and the mechanism of bacterial motility". In: *Nature* 249.452 (1974), pp. 73–74.

[111] Claudio Silvestrin. "Biotinylation of the flagellar hook in E. coli". PhD thesis. Ludwig-Maximilians-Universität München, 2010.

[112] Yoshiyuki Sowa and Richard M Berry. "Bacterial flagellar motor". In: *Quarterly Reviews of Biophysics* 41.02 (2008), pp. 103–132.

[113] Yoshiyuki Sowa, Bradley C. Stell, and Richard M. Berry. "A simple backscattering microscope for fast tracking of biological molecules". In: *Review Scientific Instruments* 81 (2010), p. 113704.

[114] Yoshiyuki Sowa et al. "Direct observation of steps in rotation of the bacterial flagellar motor". In: *Nature* 437.7060 (2005), pp. 916–919.

[115] Hirofumi Suzuki, Koji Yonekura, and Keiichi Namba. "Structure of the rotor of the bacterial flagellar motor revealed by electron cryomicroscopy and single-particle image analysis". In: *Journal of Molecular Biology* 337.1 (2004), pp. 105–113.

[116] Dennis R. Thomas et al. "The three-dimensional structure of the flagellar rotor from a clockwise-locked mutant of Salmonella enterica Serovar Typhimurium". In: *Journal of Bacteriology* 188.20 (2006), pp. 7039–7048.

[117] Murray J Tipping et al. "Load-dependent assembly of the bacterial flagellar motor". In: *mBio* 4.4 (2013), e00551–13.

[118] Natalie Verstraeten et al. "Living on a surface: swarming and biofilm formation". In: *Trends in Microbiology* 16.10 (2008), p. 496.

[119] George H Wadhams and Judith P Armitage. "Making sense of it all: bacterial chemotaxis". In: *Nature Reviews Molecular Cell Biology* 5.12 (2004), pp. 1024–1037.

[120] Fangbin Wang, Junhua Yuan, and Howard C Berg. "Switching dynamics of the bacterial flagellar motor near zero load". In: *Proceedings of the National Academy of Sciences* 111.44 (2014), pp. 15752–15755.

[121] Hongyun Wang and G Oster. "The Stokes efficiency for molecular motors and its applications". In: *Europhysics Letters* 57.1 (2002), p. 134.

[122] Charles Wolgemuth et al. "How myxobacteria glide". In: *Current Biology* 12.5 (2002), pp. 369–377.

[123] Jianhua Xing et al. "Torque-speed relationship of the bacterial flagellar motor". In: *Proceedings of the National Academy of Sciences* 103.5 (2006), pp. 1260–1265.

[124] Ruidong Xue et al. "A delicate nanoscale motor made by nature? The bacterial flagellar motor". In: *Advanced Science* 2.9 (2015), p. 1500129.

[125] Toshiharu Yakushi et al. "Roles of charged residues of rotor and stator in flagellar rotation: comparative study using H+-driven and Na+-driven motors in Escherichia coli". In: *Journal of Bacteriology* 188.4 (2006), pp. 1466–1472.

[126] Koji Yonekura, Saori Maki-Yonekura, and Michio Homma. "Structure of the Flagellar Motor Protein Complex PomAB: Implications for the Torque-Generating Conformation". In: *Journal of Bacteriology* 193.15 (2011), pp. 3863–3870.

[127] Tomohiro Yorimitsu et al. "The systematic substitutions around the conserved charged residues of the cytoplasmic loop of Na+-driven flagellar motor component PomA". In: *Journal of Molecular Biology* 320.2 (2002), pp. 403–413.

[128] J. Yuan and H. C. Berg. "Resurrection of the flagellar rotary motor near zero load". In: *Proceedings of the National Academy of Sciences* 105.4 (2008), pp. 1182–1185.

[129] Junhua Yuan and Howard C Berg. "Thermal and solvent-isotope effects on the flagellar rotary motor near zero load". In: *Biophysical Journal* 98.10 (2010), pp. 2121–2126.

[130] Junhua Yuan, Karen A Fahrner, and Howard C Berg. "Switching of the bacterial flagellar motor near zero load". In: *Journal of Molecular Biology* 390.3 (2009), pp. 394–400.

[131] Junhua Yuan et al. "Adaptation at the output of the chemotaxis signalling pathway". In: *Nature* 484 (2012), pp. 233–237.

[132] Junhua Yuan et al. "Asymmetry in the clockwise and counterclockwise rotation of the bacterial flagellar motor". In: *Proceedings of the National Academy of Sciences* 107.29 (2010), pp. 12846–12849.

[133] J. Zhou, R. T. Fazzio, and D. F. Blair. "Membrane Topology of the MotA Protein of Escherichia coli". In: *Journal of Molecular Biology* 251 (1995), pp. 237–242.

[134] Jiadong Zhou, Scott A Lloyd, and David F Blair. "Electrostatic interactions between rotor and stator in the bacterial flagellar motor". In: *Proceedings of the National Academy of Sciences* 95.11 (1998), pp. 6436–6441.